

UNIVERSITY OF CALIFORNIA, SAN DIEGO

Towards Realistic Image Synthesis of Scattering Materials

A dissertation submitted in partial satisfaction of the
requirements for the degree
Doctor of Philosophy

in

Computer Science

by

Craig Steven Donner

Committee in charge:

Professor Henrik Wann Jensen, Chair
Professor James Arvo
Professor Serge Belongie
Professor Samuel Buss
Professor David Kriegman

2006

Copyright
Craig Steven Donner, 2006
All rights reserved.

The dissertation of Craig Steven Donner is approved,
and it is acceptable in quality and form for publication
on microfilm:

Chair

University of California, San Diego

2006

いつもそばに居て
支えてくれた
愛子へ

pix·el, n. *A mischievous, magical spirit associated with screen displays. The computer industry has frequently borrowed from mythology: witness the sprites in computer graphics, the demons in artificial intelligence, and the trolls in the marketing department.*

— Jeff Meyer

TABLE OF CONTENTS

Signature Page	iii
Dedication	iv
Table of Contents	v
List of Figures	viii
List of Tables	xi
Acknowledgements	xii
Vita and Publications	xiv
Abstract of the Dissertation	xvi
Chapter 1 Introduction	1
Chapter 2 Radiative Transport	8
2.1 The Radiative Transport Equation	8
2.2 Phase Functions	11
2.3 Fresnel Reflectance	13
Chapter 3 1D light transport	14
3.1 The BRDF	14
3.2 Diffuse/Specular BRDFs	15
3.3 The Blinn BRDF	16
3.4 The Hanrahan-Krueger BRDF	18
3.5 The Stam BRDF	20
3.6 Kubelka-Munk Theory	23
Chapter 4 Monte Carlo methods	30
4.1 Path tracing	30
4.2 Bidirectional path tracing	31
4.3 Photon mapping	31
Chapter 5 Subsurface scattering of light using diffusion	33
5.1 Introduction	34
5.2 The delta-Eddington approximation	35
5.3 Deriving the diffusion equation	37
5.3.1 The diffusion equation	39

5.3.2	Solution for a point source in an infinite medium	39
5.3.3	Semi-infinite material	40
5.3.4	Diffuse internal reflectance	41
5.4	Approximate boundary condition	41
5.5	The diffusion dipole approximation	42
5.6	Discussion	45
Chapter 6	Hybrid methods	49
6.1	Diffusion and packet tracing	49
6.2	Diffusion and photon mapping	50
6.3	Diffusion and texture functions	51
Chapter 7	A new model for thin and layered materials	52
7.1	Background	53
7.2	Light scattering in thin slabs	54
7.3	Multiple layers	57
7.4	Inter-layer scattering	63
7.4.1	Accuracy of the multipole and convolution method	66
7.5	Rough surfaces	75
7.6	Rendering with the Multi-Layer Model	76
7.6.1	Texturing	78
7.7	Visual results	78
7.8	Summary and discussion	81
7.9	Acknowledgments	82
Chapter 8	A spectral shading model for human skin	89
8.1	Background	90
8.2	The structure of skin and its interaction with light	91
8.2.1	Absorption of light	92
8.2.2	Scattering of light	93
8.2.3	Skin layers	93
8.3	A two-layer model for human skin	94
8.3.1	Surface reflection	94
8.3.2	Subsurface scattering	95
8.3.3	Absorption by the epidermis	96
8.3.4	Absorption in the dermis	97
8.3.5	Scattering and thickness	98
8.3.6	Texturing	98
8.4	Implementation	99
8.5	Results	100
8.5.1	Spectral vs RGB diffusion profiles	104
8.6	Summary	105

8.7 Acknowledgments	106
Chapter 9 Conclusions	113
9.1 Future work	114
Bibliography	116

LIST OF FIGURES

Figure 1.1	(a) Lambert's model of diffuse reflection redrawn from [78]. (b) Surface penetration and scattering of light in a translucent material.	3
Figure 1.2	Scattering, or translucent, materials have striking characteristics. Images in (a) and the leaves image are used with permission.	7
Figure 2.1	Notations used in this dissertation	9
Figure 2.2	The reflection and refraction of light.	13
Figure 3.1	Geometry of the Blinn model.	17
Figure 3.2	Geometry of the Kubelka-Munk model.	24
Figure 3.3	Kubelka-Munk reflectance and transmittance for multiple layers. Redrawn from [74].	28
Figure 5.1	Extrapolated fluence.	42
Figure 5.2	An incident ray of light is converted into a real source embedded in the material, and a virtual source mirrored about the extrapolated boundary at $2AD$ above the surface. The total fluence is the sum of the fluences of the two sources.	44
Figure 5.3	The diffusion dipole can simulate the complex appearance of translucent materials. Images used with permission.	45
Figure 5.4	An example plot of a diffusion profile of a highly scattering material. The plot shows reflected radiant emittance vs. radial distance, comparing the dipole reflectance to a Monte Carlo simulation.	46
Figure 5.5	Dipole diffusion profiles compared to Monte Carlo photon packet tracing for various albedos. Note that the dipole becomes increasingly more inaccurate as the albedo decreases.	47
Figure 7.1	Dipole configuration for semi-infinite geometry (left), and the multipole configuration for thin slabs (right).	56
Figure 7.2	Comparison of the reflectance and transmission profiles of slabs of varying thickness predicted by the dipole and the multipole to Monte Carlo simulations. The slab thickness is 2 mean free paths, and the mean free path length is 1mm.	58
Figure 7.3	Comparison of the reflectance and transmission profiles of slabs of varying thickness predicted by the dipole and the multipole to Monte Carlo simulations. The slab thickness is 5 mean free paths, and the mean free path length is 1mm.	59

Figure 7.4	Comparison of the reflectance and transmission profiles of slabs of varying thickness predicted by the dipole and the multipole to Monte Carlo simulations. The slab thickness is 10 mean free paths, and the mean free path length is 1mm.	60
Figure 7.5	Comparison of the reflectance and transmission profiles of slabs of varying thickness predicted by the dipole and the multipole to Monte Carlo simulations. The slab thickness is 20 mean free paths, and the mean free path length is 1mm.	61
Figure 7.6	The mirroring distance of the multipole is changed in the case of mismatched indices. donnerF2.pdf.	63
Figure 7.7	The first two modes of the inter-scattering of light between two turbid layers.	65
Figure 7.8	Comparison of the convolved multipole with Monte Carlo simulation using parameters from Kienle [69], Figure 3.	68
Figure 7.9	Relative error of Figures 7.8 (top) and 7.8 (bottom).	69
Figure 7.10	Comparison of the convolved multipole with Monte Carlo simulation using parameters from Kienle [69], Figure 4.	70
Figure 7.11	Relative error of Figures 7.10 (top) and 7.10 (bottom).	71
Figure 7.12 (top)	Comparison of the convolved multipole with Monte Carlo simulation using parameters from Eda and Okada [27]. (bottom) Relative error with and without Kubelka-Munk correction to the convolution.	72
Figure 7.13	Reflectance of a two-layered material with (top), and without (bottom) Kubelka-Munk correction.	73
Figure 7.14	Transmittance of a two-layered material with (top), and without (bottom) Kubelka-Munk correction.	74
Figure 7.15	A piece of parchment illuminated from behind. Note, how the dipole model (left) underestimates the amount of transmitted light, while the multipole model (middle) matches the reference image computed using Monte Carlo photon tracing (right). . .	79
Figure 7.16	A buddha statuette sprayed with a thin layer of white paint. The first and third images are front-lit, the second and fourth back-lit.	84
Figure 7.17	A layered leaf lit from front and behind. The reflectances of the front and back sides of the leaf differ significantly, while the transmittance is nearly identical. Note that the color is due to multiple scattering; no textures are applied.	84
Figure 7.18	A translucent marble statue with surface roughness 0.1 on the left, 0.5 in the middle, and 1.0 on the right.	85
Figure 7.19	A multi-layered model of human skin using measured parameters for the individual skin layers [114].	86
Figure 7.20	Closeups of the complete model in the case of rendering human skin.	87

Figure 7.21 A full-face image using the complete model.	88
Figure 8.1 Spectral absorption coefficients of hemoglobin, melanins, and baseline skin absorption.	92
Figure 8.2 Two layer model of skin.	96
Figure 8.3 Change in skin color of a skin patch as melanin volume fraction C_m is increased from 0.1% to 50%.	101
Figure 8.4 Change in skin color of a skin patch as the hemoglobin fraction C_h is increased from 0.1% to 20%.	102
Figure 8.5 Change in skin color of a skin patch as the melanin blend β_m increases from 0 to 1.	102
Figure 8.6 Effect of changing ρ_s	103
Figure 8.7 Images showing the change in skin subsurface reflectance and color bleeding over the range of appearance produced by melanin, melanin blend, and hemoglobin change.	107
Figure 8.8 Calculated total diffuse reflectance spectra compared to measured data from [120]	108
Figure 8.9 Different skin types simulated with our model (top) compared to actual photographs of real skin samples (bottom).	108
Figure 8.10 Applying skin parameters to an entire face with texturing. . . .	109
Figure 8.11 Applying skin parameters to an entire face with texturing. . . .	110
Figure 8.12 Closeup of the head model using a spectral diffusion profile (left) and a RGB diffusion profiles (right).	111
Figure 8.13 The full spectral profiles for the parameters given in Figure 8.12 (top), and a closeup of the RGB diffusion profiles (bottom). . .	112

LIST OF TABLES

Table 7.1	Comparison of the total reflectance and transmission predicted by the dipole and multipole models compared to Monte Carlo for the plots in Figures 7.2–7.5.	57
Table 7.2	Optical parameters used in generating the images in Figures 7.19–7.21. η is the index of refraction, and d is the thickness of the layer.	81
Table 8.1	Parameters to our model.	99

ACKNOWLEDGEMENTS

To my ever-caring and beautiful wife Aiko, who has supported (and prodded) me throughout this long process. Without her love, support, and yes, prodding, this dissertation might still be nothing but a table of contents.

Of course, none of this would ever have been possible without my parents Gary and Barbara, for they not only brought me into this world, but taught me to observe, and learn from it. I also thank my sister Tami for being right that yes, one day, I *would* graduate.

In particular I must thank my Ph.D. adviser Henrik Wann Jensen, for had he not joined the faculty at UCSD, and shown interest in me and what I might be capable of, I would never have come this far. Thanks are also due to the other members of my Ph.D. dissertation committee, David Kriegman, Serge Belongie, Samuel Buss, and James Arvo, for agreeing to take their valuable time to read this dissertation and judge its merit.

The other people in (or formerly of, or visitors to) the combined UCSD Graphics and Vision “Pixel Lab” deserve special recognition, in particular (in alphabetical order): Sameer Agarwal, Tomas Akenine-Möller, Kristen Branson, Will Chang, Cameron Christian, Anson Chu, Piotr Dollar, Theo Engell-Nielsen, Cyrus Jam, Wojciech Jarosz, Neel Joshi, Alex Kozlowski, Arash Keshmirian, Anders Wang Kristenson, Bent Dalgaard Larsen, Satya Mallick, Vincent Rabaud, John Rapp, Steve Rotenberg, and Josh Wills. Thanks also to Matthias Zwicker (*hop Schweiz!*), and *danke schön* to Tim Weyrich and Manfred Ernst.

I would like to thank the San Diego Supercomputer Center for providing me with opportunities so early in my academic career, in particular I thank John Moreland. Also, although he has now moved on to Oregon State University, thank you to Mike Bailey, who first piqued my interest in Computer Graphics, and more importantly, who first offered me an internship at SDSC, and then somehow managed to convince me to apply to graduate school.

Finally, for their monetary support made this work possible, I thank the National Science Foundation for their funding under grant #0305399, and the Sloan Foundation.

Chapter 7, in part, is a reproduction of the material published in C. Donner and H. W. Jensen. *Light diffusion in multi-layered translucent materials*. *ACM Trans. Graphic.*,

24(3):1032–1039, 2005; and C. Donner and H. W. Jensen. *Rapid simulation of steady-state spatially-resolved reflectance and transmittance profiles of multi-layered turbid materials*. *J. Opt. Soc. Am. A*, 23(6):1382–1390, 2006. The dissertation author was the primary investigator and author of both papers.

Chapter 8, in part, is a reproduction of the material published in C. Donner and H. W. Jensen. *A spectral BSSRDF for shading human skin*. In *Rendering Techniques*, pages 409–417, 2006; and C. Donner and H. W. Jensen. *A spectral shading model for human skin*. In *ACM SIGGRAPH Sketches and Applications*, 2006. The dissertation author was the primary investigator and author of both papers.

VITA

1999–2002	Assistant Researcher, San Diego Supercomputer Center
2000–2004	Teaching Assistant, Department of Computer Science and Engineering, University of California, San Diego
2001	Bachelor of Science, <i>magna cum laude</i> , University of California, San Diego
2004	Master of Science, University of California, San Diego
2006	Doctor of Philosophy, University of California, San Diego

PUBLICATIONS

- T. J. Purcell, C. Donner, M. Cammarano, H. W. Jensen, and P. Hanrahan. *Photon mapping on programmable graphics hardware*. In *Graphics Hardware*, pages 41–50, 2003
- C. Donner and H. W. Jensen. *Faster GPU computations using adaptive refinement*. In Proceedings of ACM SIGGRAPH, Sketches and Applications, 2004
- C. Donner. *Photon mapping methods on programmable graphics hardware*. Master’s thesis, University of California at San Diego, 2004
- C. Donner and H. W. Jensen. *Light diffusion in multi-layered translucent materials*. *ACM Trans. Graphic.*, 24(3):1032–1039, 2005
- N. Joshi, C. Donner, and H. W. Jensen. *Noninvasive measurement of scattering anisotropy in turbid materials by nonnormal incident illumination*. *Opt. Lett.*, 31:936–938, 2006
- C. Donner and H. W. Jensen. *Rapid simulation of steady-state spatially-resolved reflectance and transmittance profiles of multi-layered turbid materials*. *J. Opt. Soc. Am.*, 23(6):1382–1390, 2006
- T. Weyrich, W. Matusik, H. Pfister, B. Bickel, C. Donner, C. Tu, J. McAndless, J. Lee, A. Ngan, H. W. Jensen, and M. Gross. *Analysis of human faces using a measurement-based skin reflectance model*. *ACM Trans. Graphic.*, 25:1013–1024, 2006
- S. G. Narasimhan, M. Gupta, C. Donner, R. Ramamoorthi, S. Nayar, and H. W. Jensen. *Acquiring scattering properties of participating media by dilution*. *ACM Trans. Graphic.*, 25:1003–1012, 2006

C. Donner and H. W. Jensen. *A spectral BSSRDF for shading human skin*. In *Rendering Techniques*, pages 409–417, 2006

C. Donner and H. W. Jensen. *A spectral shading model for human skin*. In *ACM SIGGRAPH Sketches and Applications*, 2006

ABSTRACT OF THE DISSERTATION

Towards Realistic Image Synthesis of Scattering Materials

by

Craig Steven Donner

Doctor of Philosophy in Computer Science

University of California, San Diego, 2006

Professor Henrik Wann Jensen, Chair

This dissertation focuses on developing accurate yet efficient shading methods for realistic image synthesis of scattering, or translucent, materials. Translucent materials are characterized by a soft “glow” when backlit, and are often mistaken for purely diffuse materials when front-lit. This appearance is caused by the penetration and subsurface scattering of light. Accurately and efficiently simulating light transport in these materials is a challenging problem in computer graphics. In this dissertation, we derive the popular diffusion dipole method widely used to simulate light transport in highly scattering materials. We analyze its strengths and weaknesses, along with the specific approximations made along its derivation.

We then introduce the multipole method, an efficient and accurate technique that simulates the transport of light in thin translucent slabs. It uses multiple dipoles mirrored about the boundaries of the slab to approximate boundary conditions on the internal radiance. We extend the multipole to model the inter-scattering of light between diffusing layers using a novel frequency domain technique similar to Kubelka-Munk theory. The new model accurately predicts the reflectance and transmittance of arbitrary systems of diffusing layers. To show the accuracy and validity of the model, we compare results of the multipole with those of Monte Carlo simulation, as well as data taken from the optics literature, and provide various photorealistic rendered images of materials such as paint, paper, and human skin.

As an example of a complete shading model, we also develop a new practical spectral model for shading human skin. We model skin as a two-layer translucent material using the multipole method. The model is driven by only four physiological parameters. These parameters control the amount of oil, melanin, and hemoglobin in the skin, which make it possible to match specific skin types, and also give a more intuitive control to drive the multipole. As validation, we compare simulated reflectance spectra of skin to actual measured data, and provide several photorealistic renderings of skin under various lighting conditions.

Chapter 1

Introduction

The goal of computer graphics is to develop algorithms that allow a computer to present a visual depiction of an environment, or *scene*, to an observer. Typically, this involves displaying a computer generated image via either printed medium or a display device. These images can be combined together temporally to create films for various purposes. Indeed, computer generated imagery has become commonplace in our daily lives, in advertising, movies, television, journalism, games, and printed media, just to name a few examples. One particularly important branch of computer graphics involves generating photorealistic imagery that recreates the physical world as accurately as possible.

Accurately describing and understanding the interaction of light with the materials that make up our environment is key to understanding our world. In this dissertation, we are primarily concerned with rendering photorealistic images of materials. In particular, we focus on the challenging problem of rendering images of translucent, or scattering, materials. In this dissertation we will often interchange the terms scattering and translucent when describing materials.

Translucent materials are all around us. For example, milk, leaves, skin, paper, clouds, paint, coffee, and marble are all scattering materials. Scattering materials make up the foods and liquids we eat and drink, and the materials that compose everyday objects such as plastics and paper. These materials make up our environment, and even the various tissues of our own bodies. The appearance of translucent materials is characterized by a

“glow” when backlit (see Figure 1.2), and they often have a soft, diffuse appearance when viewed under direct lighting.

Light has a complex interaction with translucent materials; it enters the material and is *scattered* or *absorbed* as it propagates through. Scattering is due to light interacting with suspended particles, such as fat globules in milk, or by undergoing high frequency refraction, as in biological materials such as skin, or both. In some materials, such as leaves and skin, the material may be composed of multiple layers, each with its own optical properties. Because we are attuned to their real natural appearance, these biological materials are a particular challenge to render accurately.

Light transport in biological materials is also of great importance in medical biology and medical physics. Understanding how light interacts with tissue spurs the development of therapeutic techniques, such as laser surgery [56], photodynamic therapy [130], and direct treatment of skin disorders such as cancers and subsurface stains [115]. Models must accurately predict the penetration, scattering, and absorption of light so as not to damage healthy tissue. The optical properties of turbid tissue recovered from samples can also give its physiological state [69]. In addition, models of light interaction with tissue give insight on our bodies react to light, such as in the production of melanin in skin after sun exposure [133].

Understanding light scattering is also important to many environmental sciences, where models of leaf and fauna reflectance allow for remote sensing of the health and structure of rainforests, crops, and other vegetation [33]. Scattering models also help predict changes in temperature of the oceans and atmosphere as they scatter and absorb the sun’s energy.

The propagation of light is in many ways similar to the propagation of other forms of energy, such as heat. The diffusion approximation, originally developed to explain the flight of neutrons in a nuclear fission reaction [36], has direct applicability to light transport, and is discussed in detail in Chapter 5. Realistic, accurate models of the scattering of these particles are critical to producing energy efficiently and safely.

In computer graphics, our focus is to produce accurate, efficient shading models for translucent materials. Most of the previous work in rendering models has focused on developing analytical models, but many of these models assume that light reflects only

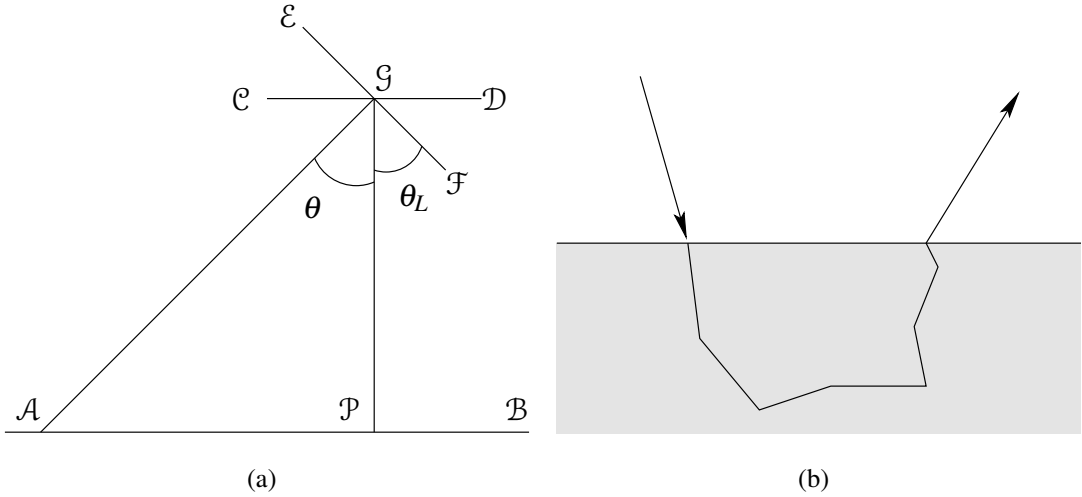


Figure 1.1: (a) Lambert's model of diffuse reflection redrawn from [78]. (b) Surface penetration and scattering of light in a translucent material.

at the surface of a material. This idea has its roots in the studies of Lambert [78], who determined that the illumination of a rough, unpolished surface decreases with the sine of the illumination angle. He illustrated his theory with the geometry in Figure 1.1(a), noting that if an illuminating surface \mathcal{CD} was rotated to the configuration \mathcal{EF} , the brightness at point \mathcal{P} would decrease with the sine of angle of emanation $\theta_L = \angle \mathcal{PGF}$. The angular dependence was later standardized by Beer [8] to be the cosine of the angle of incidence θ . Later experiments by many researchers worldwide both supported and discounted this simple theory of cosine dependence [128].

Zöllner [132], and later von Seeliger [119], theorized that a diffuse appearance could be caused by subsurface penetration, and then scattering, of light (Figure 1.1(b)). They were the first to consider the idea of subsurface scattering as the cause of a soft appearance. In his famous investigations into the natural world, Lord Rayleigh [93] discovered that small spherical particles, smaller than the wavelength of light, scatter light inversely proportional to the fourth power of the wavelength in question. This simple relation explains why the sky is blue. Lorenz, and later Mie [82], extended this to spheres of arbitrary size embedded in a homogeneous medium. Schuster also built on Rayleigh's ideas to explain the scattering of light in participating media like fog [101].

By the early 20th century, it had been shown that it was physically impossible for

Lambert and Bouguer’s models to predict the diffuse reflectance of materials [38]. Despite this, numerous light reflectance material models in computer graphics have incorporated the so-called “Lambert Cosine Law” [7, 11, 18, 45, 90, 109, 126, and others]. To be fair, these models focus on modeling the specular reflection of light from a surface, effectively ignoring the importance of translucency in the perception of materials. They were also developed with only limited computational resources, which was likely a major driving reason for simplicity. Still, they cannot simulate the translucent appearance of many materials.

The affordability of computers and their increase in computational power led to the development of Monte Carlo numerical techniques (discussed in Chapter 4), such as path tracing [66] and packet tracing [92]. While these methods can give great accuracy, their computational cost was, and remains, high.

Kubelka and Munk [75] introduced their theory for light transport in one dimension, where it quickly became popular for measuring optical properties and simulating the reflectance of pigmented materials, including leaves, skin, and paper [71]. This theory was later introduced to computer graphics by Haase and Meyer [41], and has been used to simulate the reflectance of various materials. Unfortunately, the one-dimensional assumption of Kubelka-Munk theory cannot predict the subsurface lateral scattering of light. This tends to give images rendered with this method a hard, dry look.

Blinn was the first to introduce the physics of light transport to the computer graphics community with his work on the rendering of the rings of Saturn [12]. Hanrahan and Krueger [42] later derived Blinn’s model directly from the one-dimensional radiative transport equation. These models assume that single scattering dominates subsurface scattered light. Stam [105] used a discrete matrix diagonalization approach to add the effects of multiple scattering, but still assumed one-dimensional transport. Similar to Kubekla-Munk theory, these models cannot simulate lateral scattering, and rendered images suffer from the same hard appearance. These models will be explored in Chapter 3.

Nuclear energy spawned the development of techniques capable of efficiently predicting the three-dimensional multiple scattering of particles, most notably the diffusion approximation [36]. Stam [104] introduced the diffusion approximation to computer graphics, but his multigrid approach was inefficient. Jensen et al. [62] later used the

dipole diffusion approximation to efficiently render realistic images of translucent materials, under the assumption that the material is homogeneous and semi-infinite in depth. We first derive, and then discuss, the diffusion approximation and the dipole model in Chapter 5.

The main limitations of the dipole model are its restriction to semi-infinite geometry and homogeneous materials. This precludes it from accurately rendering images of more complex materials, specifically thin and layered materials. Many common materials, such as skin, paint, leaves, and paper fit into this category. In this dissertation, we remove these restrictions and develop a new model that accurately reproduces the appearance of thin and layered translucent materials. We validate the model with both visual and numerical results.

One other limitation of previous techniques is the choice of optical properties for a particular model. Direct acquisition of these properties can be time-consuming and expensive, and even inaccurate. To mitigate this problem, this dissertation also introduces a new shading model for human skin that builds on the new model for multi-layered translucent materials. The skin model produces accurate renderings of human skin, and allows a user to predictably obtain a desired appearance with only four parameters to the model. These parameters are based on physical properties of the skin that directly describe its appearance.

The techniques presented in this dissertation generalize beyond graphics to medical physics, optics, and dermatological science. In computer graphics, they allow efficient rendering of a new class of materials, thin and multi-layered translucent materials, and specifically the generation of realistic images of human skin.

The remainder of the dissertation is organized as follows:

Chapter 2 introduces the theory of light transport in scattering materials, including the idea of radiative transport.

Chapter 3 explores one dimensional models for light transport in materials, while Chapter 4 looks at numerical solutions using Monte Carlo tracing.

Chapter 5 works through a detailed derivation of the diffusion dipole approximation for rendering translucent materials. It begins with radiative transport, derives the diffusion equation, and explains the motivation for the approximations made before using the

method of images to derive the diffusion dipole model. The exposition of this full derivation is a novel contribution that does not currently exist in the literature.

Chapter 6 looks at recent attempts to combine the efficiency of diffusion with the accuracy of other methods, in an attempt to either improve the quality of diffusion predictions, or extend diffusion to a larger class of materials.

Chapter 7 extends the work in Chapter 5 to support a new approximation for thin and layered translucent materials. This model avoids the difficulty of previous approaches through application of a novel frequency space technique, and is shown to be efficient, while still providing comparable accuracy to existing, more complicated, methods.

Chapter 8 uses the ideas proposed in Chapter 7 to construct a shading model for the specific purpose of rendering the appearance of human skin. The model is validated both qualitatively and quantitatively.

Finally, Chapter 9 summarizes the major contributions of the dissertation, and discusses avenues for future research.



Figure 1.2: Scattering, or translucent, materials have striking characteristics. Images in (a) and the leaves image are used with permission.

Chapter 2

Radiative Transport

In this section we explore some background and develop a common notation for the transport of light in translucent materials, which we will then use in later chapters. For a more thorough introduction to the theory of the propagation and scattering of light, Ishimaru [51] is an excellent reference.

2.1 The Radiative Transport Equation

Translucent materials are often made up of small “particles” of possibly varying size that both scatter and absorb light. These particles may be the organelles or small scale cellular structures in a plant leaf, or the molecular lattices in marble. High frequency changes in index of refraction can also cause scattering, such as light refracting through several cell membranes in succession. When a translucent material is struck by light, a portion of the light refracts into the medium and interacts with the material. This interaction is characterized by two possible events, scattering and absorption. Some light is reflected off of or transmitted through the material in some direction, while some light is absorbed by the material. σ_s and σ_a are defined as the *scattering* and *absorption coefficients* of the material, describing how much light is absorbed and scattered by the material per unit volume. In this dissertation, unless otherwise specified, we assume that the material is homogeneous; the absorption and scattering characteristics are constant throughout the material.

\vec{n}	Normal to a surface
\vec{x}	Position
r	Radial position
$\vec{\omega}$	Direction
$d\vec{\omega}$	Differential solid angle
L	Radiance
σ_a	Absorption coefficient
σ_s	Scattering coefficient
σ_t	Extinction coefficient
σ_{tr}	Effective transport coefficient
τ	Optical depth
α	Albedo
D	Diffusion constant
f	Average cosine of the scattering angle
g'	Degree of scattering anisotropy
p	Phase function
ϕ	Fluence (scalar/space irradiance)
\mathbf{E}	Vector (anisotropic) irradiance

Figure 2.1: Notations used in this dissertation

If a beam of light contributes radiance L into the material, then each unit volume will scatter $\sigma_s L$ radiance, and $\sigma_a L$ radiance will be absorbed. As the beam of light moves a small distance dz through the medium, then the *flux*, or change in intensity, due to scattering and absorption along that distance is

$$dL(\vec{x}, \vec{\omega}) = -dz(\sigma_s + \sigma_a)L = -dz \sigma_t L, \quad (2.1)$$

where $\vec{\omega}$ is the direction of the beam's propagation and $\sigma_t = \sigma_s + \sigma_a$ is the called the *extinction coefficient*. We define the z -axis as pointing into the material in the direction opposite its normal.

Without loss of generality, we can separate incident radiance into two components, the

reduced incident radiance L_{ri} , or reduced intensity –the collimated part of the radiance– and the diffuse radiance L_d , which is independent of direction

$$L(\vec{x}, \vec{\omega}) = L_{ri}(\vec{x}, \vec{\omega}) + L_d(\vec{x}, \vec{\omega}). \quad (2.2)$$

We express a beam of light with radiance Φ incident upon a material from above as

$$L(\vec{x}, \vec{\omega}) = \Phi \delta(\mu - \mu_0) \quad (2.3)$$

where $\mu = \vec{\omega} \cdot \hat{\mathbf{z}}$ is the cosine of the angle between $\vec{\omega}$ and the z -axis, μ_0 is the cosine of the angle between the direction of the beam and the z -axis, and δ is the Dirac delta function.

The *reduced intensity*, or the intensity of the unscattered light within the material, is light transmitted across the interface and attenuated exponentially with distance z from the surface. This attenuation is due to absorption and out-scattering, hence the extinction coefficient is used.

$$L_{ri}(\vec{x}, \vec{\omega}) = \Phi e^{-\sigma_t z / \mu_0} \delta(\mu - \mu_0). \quad (2.4)$$

Note that this light will travel a distance of z/μ_0 to reach depth z . This attenuation of light can also be defined in terms of the *optical depth* τ , where

$$\tau(z) = \int_0^z \sigma_t dz. \quad (2.5)$$

When σ_t is constant (as in the case of a homogeneous material), $\tau = \sigma_t z$, and (2.4) becomes

$$L_{ri}(\vec{x}, \vec{\omega}) = \Phi e^{-\tau / \mu_0} \delta(\mu - \mu_0). \quad (2.6)$$

We also define $\alpha = \frac{\sigma_s}{\sigma_t}$ as the *albedo* of the scatterers in the material. The more highly scattering the material, the closer the albedo is to unity. An albedo of zero corresponds to a purely absorbing material.

As the beam of light moves through the slab, its intensity will decrease by the above amount, but will be increased by light scattering *into* the beam's direction ($\vec{\omega}$) from other directions ($\vec{\omega}'$). We can represent this in-scattered light by integrating the contributions over the sphere of incident directions and scaling by the *phase function* p

$$L_{in}(\vec{x}, \vec{\omega}) = \int_{4\pi} p(\vec{\omega}, \vec{\omega}') L(\vec{x}, \vec{\omega}') d\vec{\omega}'. \quad (2.7)$$

The phase function describes the amount of light scattered from $\vec{\omega}'$ to $\vec{\omega}$. We generally assume the phase function depends only on the cosine of the scattering angle, $p(\vec{\omega}, \vec{\omega}') \Rightarrow p(\vec{\omega} \cdot \vec{\omega}')$. The next section will discuss different phase functions in more detail. The mean cosine of the scattering angle, g , is defined as [51]

$$g = \int_{4\pi} p(\vec{\omega}, \vec{\omega}') (\vec{\omega} \cdot \vec{\omega}') d\vec{\omega}'. \quad (2.8)$$

Given the above equations, the total amount of light in-scattered to our beam propagating in direction $\vec{\omega}$ along a distance dz is

$$\sigma_s dz \int_{4\pi} p(\vec{\omega}, \vec{\omega}') L(\vec{x}, \vec{\omega}') d\vec{\omega}'. \quad (2.9)$$

Summing (2.1) and (2.9), and dividing by dz gives the classic radiative transport equation (RTE)

$$\frac{dL(\vec{x}, \vec{\omega})}{dz} = -\sigma_t L(\vec{x}, \vec{\omega}) + \sigma_s \int_{4\pi} p(\vec{\omega}, \vec{\omega}') L(\vec{x}, \vec{\omega}') d\vec{\omega}', \quad (2.10)$$

which states that the change in radiance in a particular direction is due to loss from absorption and out-scattering, and gain from in-scattering.

2.2 Phase Functions

The phase function defines the fraction of incident light that is scattered in a particular direction. To conserve energy, a phase function must integrate to unity over the sphere of directions. The simplest phase function is the isotropic constant function

$$p(\vec{\omega}, \vec{\omega}') = \frac{1}{4\pi} \quad (2.11)$$

This function can be used with the particles are far smaller than the wavelength of the light.

All other phase functions are anisotropic. One phase function designed to be consistent with a Lambertian distribution has the form [29]

$$p_L(\vec{\omega}, \vec{\omega}') = \frac{8}{3}\pi (\sin(\vec{\omega} \cdot \vec{\omega}') + (\vec{\omega} \cdot \vec{\omega}') \cos(\vec{\omega} \cdot \vec{\omega}')). \quad (2.12)$$

A more common phase function was developed by Henyey and Greenstein [48] to model materials that contain random distributions of various sized particles, such as clouds of interstellar dust

$$p_{HG}(\vec{\omega}, \vec{\omega}') = \frac{1}{4\pi} \frac{1-g^2}{(1+g^2 - 2g\vec{\omega} \cdot \vec{\omega}')^{\frac{3}{2}}}. \quad (2.13)$$

Here $-1 \leq g \leq 1$ determines the level of anisotropy. Values of $g > 0$ indicate forward scattering, while $g < 0$ gives rise to backwards scattering. Because the function has only a cosine dependence on the incident and exitant, it assumes that the scattering is uniform in cones around the incident direction.

Another phase function useful for radiative transfer is the delta-Eddington phase function

$$p_{dE}(\vec{\omega}, \vec{\omega}') = \frac{1}{4\pi} [2f\delta(1 - \vec{\omega} \cdot \vec{\omega}') + (1-f)(1 + 3g'\vec{\omega} \cdot \vec{\omega}')], \quad (2.14)$$

where f determines the amount of light scattered into the forward peak (the first term), and the *asymmetry coefficient* g' denotes the strength of the anisotropy in the diffuse scattering. The delta-Eddington phase function follows the Henyey-Greenstein phase function very closely, but is mathematically simpler to evaluate without the division and costly square root [63]. The parameters f and g' are related to the mean scattering angle of the Henyey-Greenstein phase function by

$$f = g^2 \quad \text{and} \quad g' = \frac{g}{1+g}. \quad (2.15)$$

For materials that are mixtures of other materials, such as paints or mixed liquids, the scattering and absorption coefficients are the weighted sum based on volume fraction and the phase function.

$$\sigma_a = \sum_{i=0}^N w_i \sigma_{a,i}, \quad \sigma_s p(\theta, g) = \sum_{i=0}^N w_i \sigma_{s,i} p(\theta, g_i), \quad (2.16)$$

where w_i is the fraction of total volume occupied by each component [26]. Physically, this assumes that as the particles of two different materials mix together, the particles become randomized, and photons are likely to interact with particles from each individual component. To average the scattering of the mixture, the phase function is needed to properly weight the contribution of each scattering coefficient.

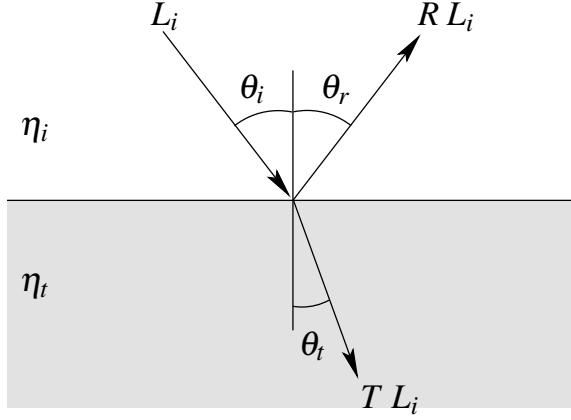


Figure 2.2: The reflection and refraction of light.

2.3 Fresnel Reflectance

The amount of light that refracts into the material and is then scattered is governed by the index of refraction of the incident and transmitted materials, and the incoming and transmitted angles (Figure 2.2). These quantities are related by Snell's Law

$$\eta_i \sin \theta_i = \eta_t \sin \theta_t, \quad (2.17)$$

where η_i and η_t are the indices of refraction of the incoming and transmissive materials, and θ_i and θ_t are the incident and transmitted angles.

The relative power of the light reflecting at the surface of the material is governed by Fresnel's equations

$$R_{\parallel} = \frac{\tan(\theta_i - \theta_t)}{\tan(\theta_i + \theta_t)} \quad R_{\perp} = \frac{\sin(\theta_i - \theta_t)}{\sin(\theta_i + \theta_t)}, \quad (2.18)$$

where R_{\parallel} indicates light parallel to the surface, and R_{\perp} light perpendicular to it. For unpolarized light, which we assume in this dissertation, the expression for Fresnel reflectance becomes

$$R(\theta) = \frac{1}{2} (R_{\parallel} + R_{\perp}). \quad (2.19)$$

At normal incidence ($\theta = 0$), the limit is taken to give

$$R_0(\theta = 0) = \left(\frac{\eta_i - \eta_t}{\eta_i + \eta_t} \right)^2. \quad (2.20)$$

Chapter 3

1D light transport

Because of the complex 3D nature of light scattering in translucent materials, light is often assumed to propagate only in 1D. This greatly simplifies the light transport problem, and leads to analytic models that are easy to use and understand. The main limitation of a 1D approximation, however, is that it forces light to scatter at a single point, the point of incidence. In this chapter we explore several different models that make 1D assumptions about light transport.

3.1 The BRDF

A *bidirectional reflectance distribution function* (BRDF) is the analogue of the phase function for surfaces. It defines the ratio of light incident to reflected light on a surface over the positive hemisphere [85]

$$f_r(\vec{\omega}_o, \vec{\omega}_i) = \frac{dL(\vec{x}, \vec{\omega}_o)}{L(\vec{x}, \vec{\omega}_i)(\vec{\omega}_i \cdot \vec{n}) d\vec{\omega}_i}. \quad (3.1)$$

Here $\vec{\omega}_i$ and $\vec{\omega}_o$ represent the incoming and outgoing directions, respectively, dL is the reflected differential radiance in direction $\vec{\omega}_o$, $L(\vec{x}, \vec{\omega}_i)$ is the incident radiance, and \vec{n} is the normal of the surface at \vec{x} . The dot product between the surface normal and the incident direction projects the area of the light onto the surface. Rearranging terms, we see that the contributed exitant radiance $L(\vec{x}, \vec{\omega}_o)$ from a single direction $\vec{\omega}_i$ is the product

of the projected incident radiance and the BRDF of the material

$$dL(\vec{x}, \vec{\omega}_o) = f_r(\vec{\omega}_o, \vec{\omega}_i)L(\vec{x}, \vec{\omega}_i)(\vec{\omega}_i \cdot \vec{n}) d\vec{\omega}_i. \quad (3.2)$$

The total exitant radiance the integral of contributions of incident radiance over the hemisphere of directions above \vec{x}

$$L(\vec{x}, \vec{\omega}_o) = \int_{2\pi} f_r(\vec{\omega}_o, \vec{\omega}_i)L(\vec{x}, \vec{\omega}_i)(\vec{\omega}_i \cdot \vec{n}) d\vec{\omega}_i. \quad (3.3)$$

Equation 3.3 is known as the *rendering equation* [66]. It is the surface analogue of the in-scattering term of the RTE. Note that the incident and exitant radiance are both evaluated at \vec{x} . This precludes the modeling any of the effects that occur from light propagating through the material. Despite this limitation, however, several BRDFs have previously been applied to model scattering materials.

In the case of transmitted radiance, the BRDF is replaced by a *bidirectional transmission distribution function* (BTDF) [85], though it has the same hemispherical form as the BRDF (3.1). The distinction is that the BTDF integral is over the negative hemisphere below the surface.

3.2 Diffuse/Specular BRDFs

Phong [90], and later Blinn [11], introduced simple BRDFs of the form

$$f_r(\vec{\omega}_o, \vec{\omega}_i) = (\kappa_d + \kappa_s S(\vec{\omega}_o, \vec{n}, \vec{\omega}_i))(\vec{\omega}_i \cdot \vec{n}). \quad (3.4)$$

where κ_d and κ_s are user-defined constants. The first term is Lambert's approximation for diffuse reflectance, modulated by a diffuse coefficient κ_d , while S defines a specular highlight modulated by a similar coefficient κ_s . Usually κ_d and κ_s are chosen such that $\kappa_d + \kappa_s \leq 1$, to conserve energy. Phong defined S in terms of the perfect specular reflection direction \mathbf{R} , while Blinn used the vector \mathbf{H} halfway between the outgoing ($\vec{\omega}_o$) and incoming ($\vec{\omega}_i$) directions, to avoid calculating \mathbf{R} .

Two other popular BRDF algorithms were developed by Torrance and Sparrow [109], and Ward [126]. The Torrance-Sparrow BRDF models the surface as a collection of

randomly distributed mirrors, or microfacets. Different distributions of these microfacets can model different kinds of specular reflection; a Beckmann or Gaussian distribution is commonly used. The Ward BRDF is designed to model anisotropic surface reflection by parameterizing the distribution of slopes over the surface. In both BRDFs, however, their diffuse component is essentially unchanged from Phong’s original model.

He *et al.* [44, 45] developed a comprehensive model for surface reflection based on Kirchoff transport theory, essentially adding complexity to the S term of the Phong model. Although their model goes into considerable detail regarding shadowing, masking, Fresnel effects, and roughness, it contains only a single constant Lambertian term to account for “diffuse reflectance.”

Both Schlick [99], and Shirley and Hu [102] noted that most BRDFs fail to capture the effects of subsurface scattering, but still assumed that diffuse reflectance would be mostly constant across a surface. Schlick’s algorithm accounted for Fresnel effects due to a transparent layer above a matte surface, but his model aimed more for computational efficiency than physical realism. Shirley and Hu’s algorithm attempted to couple glossy reflections from transparent layers (similar to Schlick) with a constant diffuse term at low angles of incidence. They still assumed, however, that calculating diffuse reflectance in a way more complicated than a Lambertian model would be too computationally expensive.

3.3 The Blinn BRDF

Blinn [12] was the first in computer graphics to introduce a scattering model based on the physics of light transport, in an attempt to reproduce the far-field reflectance of fuzzy or cloudy surfaces. He assumed that single scattering dominates the reflected radiance. To compute the reflectance from an infinitely wide slab of scattering particles using Blinn’s method, consider the “v”-shaped path of light that scatters at a single particle inside a layer of scatterers, shown in Figure 3.1. The incident radiance is attenuated along both paths to and from the particle due to extinction. If the incident light comes from direction $\vec{\omega}_i$, then the amount of light that reaches the particle at depth z is

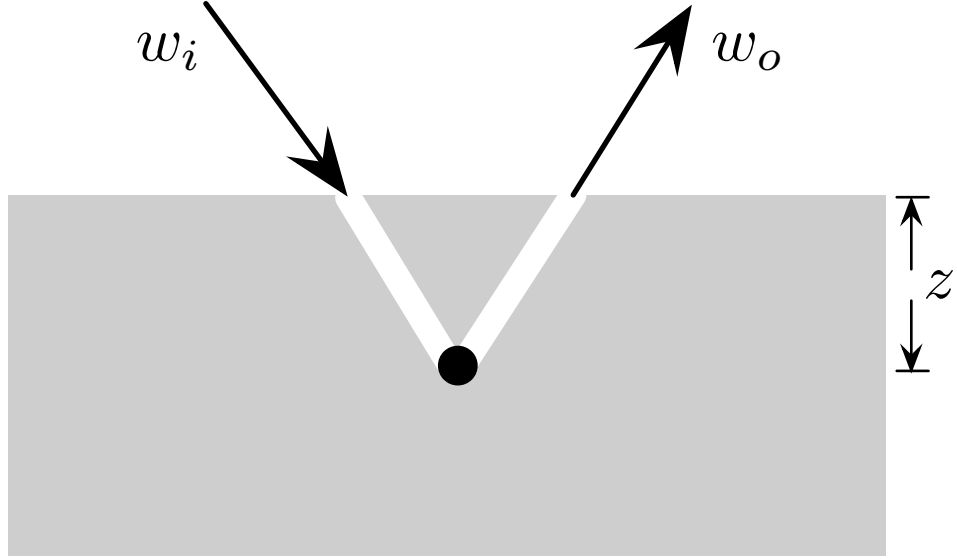


Figure 3.1: Geometry of the Blinn model.

$$\int_0^z L(\vec{x}, \vec{\omega}_i) e^{-\tau/\cos \theta_i} \quad (3.5)$$

where τ is the optical depth, $L(\vec{x}, \vec{\omega}_i)$ is the incident radiance on the cloud of particles at \vec{x} , $\theta_i = \vec{\omega}_i \cdot \vec{n}$, and \vec{n} is the normal at the surface. Of this light, some amount, governed by the phase function, will scatter in direction $\vec{\omega}_o$ towards the surface, and be attenuated along its exitant path.

$$\begin{aligned} L(\vec{x}, \vec{\omega}_o) &= \sigma_s \int_0^z p(\vec{\omega}_i, \vec{\omega}_o) L(\vec{x}, \vec{\omega}_i) e^{-\tau/\cos \theta_i} e^{-\tau/\cos \theta_o} \\ &= \alpha p(\vec{\omega}_i, \vec{\omega}_o) \frac{\cos \theta_i}{\cos \theta_i + \cos \theta_o} (1 - e^{-\tau(1/(\cos \theta_i + 1/\cos \theta_o))}) L(\vec{x}, \vec{\omega}_i), \end{aligned} \quad (3.6)$$

where $\theta_o = \vec{\omega}_o \cdot \vec{n}$. Similarly, if a slab of thickness d is lit from the bottom, the result becomes

$$L(\vec{x}, \vec{\omega}_o) = \alpha p(\vec{\omega}_i, \vec{\omega}_o) \frac{\cos \theta_i}{\cos \theta_i - \cos \theta_o} (e^{-\tau/\cos \theta_i} - e^{-\tau/\cos \theta_o}) L(\vec{x}, \vec{\omega}_i). \quad (3.7)$$

Thus the exitant radiance depends on the optical properties of the material, the scattering and absorption coefficients (contained in the albedo α), and the phase function. The choice of phase function depends on the type of material to be simulated; Blinn recommended an empirical phase function that was a linear combination of a Lambertian and Henyey-Greenstein phase functions for dusty clouds.

3.4 The Hanrahan-Krueger BRDF

Hanrahan and Krueger [42] noted that diffuse-plus-specular BRDFs could not realistically model light transport scattering materials. They based their opinion in part on Grabowski's [38] proof that it is impossible for any combination of surface roughness and reflectance to create a diffuse appearance. This led to them to develop a BRDF model identical to Blinn's [12], but derived directly from the 1D radiative transport equation.

Direct reflection of light in the Hanrahan-Krueger model is handled with a diffuse BRDF modulated by a Fresnel reflection term. The rest of the model is dedicated to determining the contribution of subsurface scattering. Similar to Blinn [12], we again formulate single scattering as an integral of the in-scattered radiance along the z -axis. The 1D form of the radiative transport equation is

$$\cos \theta_i \frac{dL(z, \vec{\omega}_o)}{dz} = -\sigma_t L(z, \vec{\omega}_o) + \sigma_s \int_{4\pi} p(\vec{\omega}_i, \vec{\omega}_o) L(z, \vec{\omega}_i) d\vec{\omega}_i, \quad (3.8)$$

where the cosine term accounts for change in path length of light entering the material at an angle θ_i to the normal, and $L(z, \vec{\omega}_i)$ is the incident radiance. Note that this 1D assumption essentially forces light to travel in only two directions, up ($+\hat{\mathbf{z}}$) and down ($-\hat{\mathbf{z}}$). That is, light must enter and exit the material at the same point, with a path length modulated by the cosine term, and the internal radiance of the slab is a function of depth z .

The amount of in-scattered light at a certain depth in the material from a single scattering event is the second term of Equation 3.8. Integrating this along the depth z to the surface of the material, accounting for attenuation on the incident and exitant paths (as in Equation 2.4) gives

$$L(\vec{x}, \vec{\omega}_o) = \int_0^z e^{-\tau/\cos \theta_i} e^{-\tau/\cos \theta_o} \sigma_s \int_{4\pi} p(\vec{\omega}_o, \vec{\omega}_i) L(z, \vec{\omega}_i) d\vec{\omega}_i \frac{dz}{\cos \theta_i}. \quad (3.9)$$

where again τ is the optical depth.

The boundary conditions for this equation are determined by separating the radiance into its downward and upward components

$$L(z, \vec{\omega}_o) = L_+(z, \vec{\omega}_o) + L_-(z, \vec{\omega}_o^*) \quad (3.10)$$

where L_+ is the radiance in the $\hat{\mathbf{z}}$ direction, and L_- is in the $-\hat{\mathbf{z}}$ direction, and $\vec{\omega}_o^*$ denotes the direction opposite $\vec{\omega}_o$ ($\vec{\omega}_o = \langle \theta_o, \phi_o \rangle$ while $\vec{\omega}_o^* = \langle \pi - \theta_o, \phi_o \rangle$).

If we assume no decrease in intensity from surface roughness, then the forward radiance at the top of the material is the incident radiance modulated by the Fresnel reflectance

$$L_+(\vec{x}, \vec{\omega}_o) = T^{\text{top}} L(z=0, \vec{\omega}_o), \quad (3.11)$$

where T^{top} is the Fresnel transmittance at the surface. L_+ is calculated directly. The remaining radiance L_s due to subsurface scattering is the total radiance passing upward through the surface at $z=0$

$$L_s(\vec{x}, \vec{\omega}_o) = T^{\text{top}}^{-1} L_-(z=0, \vec{\omega}_o^*), \quad (3.12)$$

which is modulated by a Fresnel term T^{top}^{-1} , while the light transmitted completely through the material is the radiance reaching the bottom, $L_{s,t}$, and is traveling in the $\hat{\mathbf{z}}$ direction

$$L_{s,t}(\vec{x}, \vec{\omega}_o) = T^{\text{bot}} L_+(z=d, \vec{\omega}_o), \quad (3.13)$$

where d is the thickness of the layer, and may be infinite. In the Hanrahan-Krueger model the reflected and transmitted radiance is completely determined by computing $L_+(z=d)$ and $L_-(z=0)$. Solving the above integral equation, however, particularly for an arbitrary number of scattering events, is non-trivial. To simplify the problem, Hanrahan and Krueger assume that the amount of subsurface scattered radiance is dominated by single-scattered radiance; light that scatters only once in the material before exiting. They approximate the multiply scattered light with a constant term, assuming that these higher orders would follow Lambert's Cosine Law due to randomized scattering

$$L_s(r, \vec{\omega}_o) = L^{(1)}(r, \vec{\omega}_o) + L^m \quad (3.14)$$

where L^m is the Lambertian approximation. If a true multiple scattering term is desired, Hanrahan and Krueger suggest precomputing the exitant radiance's angular distribution with a Monte Carlo simulation.

The single scattering term, $L^{(1)}$, is calculated directly from (3.9). Because we assume only a single scattering event, the light that is scattered must be directly from the reduced

intensity at that depth. Substituting the reduced intensity into (3.9) for $L(z, \vec{\omega}_i)$ and simplifying gives the same result as Blinn's derivation

$$L_s^{(1)}(z, \vec{\omega}_o) = \alpha T^{1 \rightarrow 2} T^{2 \rightarrow 1} p(\vec{\omega}_o^*, \vec{\omega}_i) \frac{\cos \theta_i}{\cos \theta_i + \cos \theta_o} (1 - e^{-\tau(1/(\cos \theta_i + 1/\cos \theta_o))}) L_i(z, \vec{\omega}_i),$$

where we have substituted α in for the albedo of the material. If the thickness of the layer increases ($\tau \rightarrow \infty$), and the material scatters isotropically, neglecting Fresnel effects, this simplifies to

$$L(\vec{x}, \vec{\omega}_o) = \frac{\cos \theta_i}{\cos \theta_i + \cos \theta_o} L_i(\vec{x}, w_i) \quad (3.15)$$

which is known to astrophysicists as the Lommel-Seeliger Law, a simple relation often used to model the reflectivity of the Moon [43]. Similarly to above, we can solve for the forward scattered light at $z = d$ and again obtain Blinn's result

$$L_{s,t}^{(1)}(z, \vec{\omega}_o) = \alpha \frac{\cos \theta_i}{\cos \theta_i - \cos \theta_o} T^{1 \rightarrow 2} T^{2 \rightarrow 3} p(\vec{\omega}_o, \vec{\omega}_i) (e^{-\tau(1/\cos \theta_i)} - e^{-\tau/\cos \theta_o}) L(z, \vec{\omega}_i).$$

When $\cos \theta_o = \cos \theta_i$, applying L'Hospital's rule avoids the division by zero

$$L_{s,t}^{(1)}(z, \vec{\omega}_o) = \alpha T^{1 \rightarrow 2} T^{2 \rightarrow 3} p(\vec{\omega}_o, \vec{\omega}_i) \frac{\tau}{\cos \theta_o} e^{-\tau/\cos \theta_o} L(z, \vec{\omega}_o). \quad (3.16)$$

Because of the assumption that light both enters and exits the material at the same location, the Hanrahan-Krueger model fails to capture the bleeding of light laterally across an object, characteristic of translucent materials. This is because, as later shown by Jensen and Buhler [59], for highly scattering translucent materials, multiple scattering dominates single scattering.

3.5 The Stam BRDF

Stam [105] was motivated by the problem of simulating light transport in human skin. He also derived his BRDF for a homogeneous slab from 1D radiative transport, but used a matrix operator approach and the discrete ordinate method, and also included the effects of isotropic surface roughness in his model. His model was the first non-Monte Carlo method in computer to incorporate the effects of multiple scattering

Stam computed the surface reflectance using a microfacet model similar to the Torrance-Sparrow [109] and van Ginneken [7] BRDFs. His subsurface scattering term

is, however, a discrete approximation, but begins similarly to the Hanrahan and Krueger model with the 1D radiative transport equation

$$\cos \theta_i \frac{dL(z, \vec{\omega}_o)}{dz} = -\sigma_t L(z, \vec{\omega}_o) + \sigma_s \int_{4\pi} p(\vec{\omega}_i, \vec{\omega}_o) L(z, \vec{\omega}_i) d\vec{\omega}_i$$

To simplify the equation, first discretize both the phase function and the incident radiance into cosine series

$$p(\vec{\omega}_i, \vec{\omega}_o) = \sum_{k=0}^{\infty} p_k(\theta_i, \theta_o) \cos k(\phi_o - \phi_i) \quad (3.17)$$

$$L(z, \vec{\omega}_i) = \sum_{k=0}^{\infty} L_k(z, \theta_i) \cos k(\phi_o - \phi_i) \quad (3.18)$$

Substituting these back into Equation 3.8 leads to a system of linear equations

$$\cos \theta_i \frac{dL_k(\tau, \theta_o)}{d\tau} = -L_k(\tau, \theta_o) + A_k \int_{-1}^1 p_k(\theta_i, \theta_o) L_k(\tau, \theta_i) d\theta_i \quad (3.19)$$

where $A_k = \alpha \frac{1+\delta_{0,k}}{4}$, $\delta_{0,k}$ is the discrete (Kronecker) delta function, and we have written the equation in terms of the optical depth τ . Discretizing the integral using

$$\int_{-1}^1 f(u) du \approx \sum_{m=1}^M w_m \{f(-u_m) + f(u_m)\} \quad (3.20)$$

where w_m are the weights and $u_m \geq 0$ are the discrete ordinates, gives a system of linear equations approximating the change in radiance

$$\cos \theta_n \frac{dL_k(\tau, \theta_n)}{d\tau} = -L_k(\tau, \theta_n) + A_k \sum_{m=1}^M w_m [p_k(-\theta_m, \theta_n) L_k(\tau, -\theta_m) + p_k(\theta_m, \theta_n) L_k(\tau, \theta_m)] \quad (3.21)$$

$$-\cos \theta_n \frac{dL_k(\tau, -\theta_n)}{d\tau} = -L_k(\tau, -\theta_n) + A_k \sum_{m=1}^M w_m [p_k(-\theta_m, -\theta_n) L_k(\tau, -\theta_m) + p_k(\theta_m, -\theta_n) L_k(\tau, \theta_m)] \quad (3.22)$$

As $p_k(-\theta_m, \theta_i) = p_k(\theta_m, -\theta_n)$ and $p_k(\theta_m, \theta_i) = p_k(-\theta_m, -\theta_n)$ we can rewrite the above in matrix notation, using the following helpful $M \times M$ matrices

$$(A_k)_{k,m} = (A_k w_m p_k(\theta_m, \theta_n) - \delta_{n,m}) / \cos \theta_n \quad (3.23)$$

$$(B_k)_{k,m} = A_k w_m p_k(\theta_m, -\theta_n) / \cos \theta_n. \quad (3.24)$$

Putting these together into a single $2M \times 2M$ scattering matrix

$$\mathbf{S}_k = \begin{pmatrix} -\mathbf{A}_k & -\mathbf{B}_k \\ \mathbf{B}_k & \mathbf{A}_k \end{pmatrix} \quad (3.25)$$

allows us to rewrite Equation 3.22 as

$$\mathbf{W} \frac{d\mathbf{L}_k(\tau)}{d\tau} = \mathbf{L}_k(\tau) - \mathbf{S}_k \mathbf{L}_k(\tau) \quad (3.26)$$

where \mathbf{W} is a vector containing the discrete cosine terms, \mathbf{L}_k is a vector of the discrete radiance terms, and we omit the dependence on angle for convenience. This expression is written more compactly as an ordinary homogeneous vector differential equation

$$\frac{d\mathbf{L}_k(\tau)}{d\tau} = \mathbf{M}_k \mathbf{L}_k(\tau) \quad (3.27)$$

where $\mathbf{M}_k = \mathbf{W}^{-1}(\mathbf{I} - \mathbf{S}_k)$, and \mathbf{I} is the identity matrix. To solve this differential equation, first diagonalize the matrix \mathbf{M} by computing its eigenvalues and eigenvectors such that $\mathbf{M} = \mathbf{V}\mathbf{D}\mathbf{V}^{-1}$, where \mathbf{D} is a diagonal matrix containing the eigenvalues of \mathbf{M} , and \mathbf{V} stores the eigenvectors columnwise. Rewriting the above expression and omitting the dependence on k gives

$$\frac{d\mathbf{w}(\tau)}{d\tau} = \mathbf{D} d\tau \mathbf{w}(\tau) \quad (3.28)$$

where $\mathbf{w} = \mathbf{V}^{-1}\mathbf{L}$. This expression has the exact solution

$$\mathbf{w}(\tau) = e^{\mathbf{D}\tau} \mathbf{u}, \quad (3.29)$$

where $e^{\mathbf{D}\tau}$ is a diagonal matrix whose entries are the exponentiated values of $\mathbf{D}\tau$, and \mathbf{u} is determined by the boundary conditions of the problem. Inverting the diagonalization gives the radiance in terms of \mathbf{u}

$$\mathbf{L}(\tau) = \mathbf{V}\mathbf{w}(\tau) = \mathbf{V}e^{\mathbf{D}\tau}\mathbf{u}, \quad (3.30)$$

The boundary conditions for this equation at the top and bottom of a slab of optical depth τ_d are

$$\mathbf{L}(0) = \mathbf{T}^{\text{top}} \mathbf{L}_i + \mathbf{L}_+(0) \quad (3.31)$$

$$\mathbf{L}_+(\tau_d) = \mathbf{R}_{\text{bot}} \mathbf{L}_-(\tau_d) \quad (3.32)$$

where \mathbf{T}^{top} is the discrete form of the transmittance at the top surface, \mathbf{L}_i is the discrete incident radiance, and \mathbf{R}_{bot} is the discrete reflectance at the bottom surface of the slab. These equations state that the radiance at the top of the slab is the sum of the transmitted

incident radiance, and the upwelling radiance at the surface; the radiance at the bottom of the slab is the reflected downwelling radiance. These expressions are similar to Hanrahan and Krueger's, though the z -axis is reversed, and in discrete form.

Rewriting Equation 3.30 terms of upward and downward directions

$$\begin{pmatrix} \mathbf{L}_+(\tau) \\ \mathbf{L}_-(\tau) \end{pmatrix} = \begin{pmatrix} \mathbf{V}_+ & \mathbf{V}_- \\ \mathbf{V}_- & \mathbf{V}_+ \end{pmatrix} \begin{pmatrix} e^{\mathbf{L}_+\tau} \mathbf{u}_+ \\ e^{-\mathbf{L}_-\tau} \mathbf{u}_- \end{pmatrix} \quad (3.33)$$

and substituting Equations 3.31 and 3.32 into it gives a solvable linear system that is used to find the radiance at the top and bottom of the slab. Modulating those with transmittance terms gives the final exitant radiance due to 1D subsurface scattering.

In the case of low albedo and a smooth surface, Stam's model simplifies to a discrete form of the Hanrahan-Krueger and Blinn models. In case of higher albedo, however, because Stam's model includes multiple scattering, it tends to predict a higher exitant radiance than single scattering models. It also incorporates limited anisotropic scattering depending on the phase function. Still, because the model is based on 1D light transport, it does not capture the soft or glowing appearance of translucent materials due to 3D subsurface transport of light.

3.6 Kubelka-Munk Theory

Although it was not originally defined as a BRDF model, Haase and Meyer also introduced a 1D light transport model for materials composed of scattering and absorbing pigments [41]. The model is based on Kubelka-Munk [75] theory, and was popular for some time to simulate light transport in materials such as paper, paint, skin, and plant leaves.

The Kubelka-Munk model makes a similar set of assumptions to the Hanrahan-Krueger and Blinn models, namely that the material is homogeneous with diffuse light incident, and that light scatters only in 1D. Consider the situation shown in Figure 3.2b, where we have a scattering and absorbing layer with thickness d covering a reflective background. Note that here we define the $\hat{\mathbf{z}}$ axis as pointing up, the opposite from before, to simplify our calculations later.

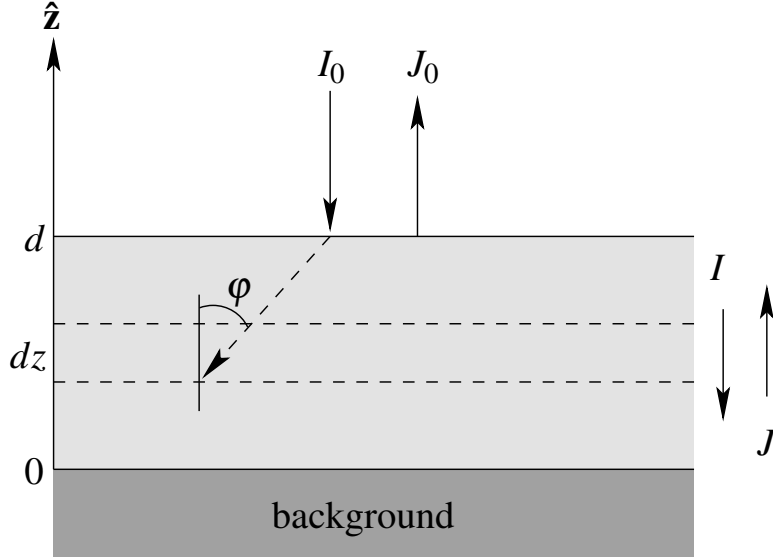


Figure 3.2: Geometry of the Kubelka-Munk model.

Similar to the Hanrahan-Krueger model, the Kubelka-Munk model is also based on examining the change in radiance over a small distance in the material. Assume the material is lit from above by I_0 diffuse light, and that the material scatters isotropically. The light falling on the thin cross section dz shown in Figure 3.2b is uniformly distributed in all directions. Consider a particular ray of light scattered at an angle φ with the surface normal, as shown by the dashed arrow in the figure. The path length of the ray through the cross section will be $\frac{dz}{\cos \varphi}$. If the angular distribution of the intensity falling on the cross section is $\partial I / \partial \varphi$, then the amount of light moving in direction φ is $\frac{1}{I_0} \frac{\partial I}{\partial \varphi}$. The average path length of the light passing through the cross section in the downward I direction is then [73]

$$d\xi_I = \int_0^{\frac{\pi}{2}} \frac{1}{I_0} \frac{\partial I}{\partial \varphi} \frac{dz}{\cos \varphi} d\varphi = dz \int_0^{\frac{\pi}{2}} \frac{1}{I_0} \frac{\partial I}{\partial \varphi} \frac{d\varphi}{\cos \varphi} \equiv u dz, \quad (3.34)$$

where we make the substitution of u for the integral. Similarly, the average path length of the light passing *upward* through the cross section toward the surface in the J direction is

$$d\xi_J = dz \int_0^{\frac{\pi}{2}} \frac{1}{J_0} \frac{\partial J}{\partial \varphi} \frac{d\varphi}{\cos \varphi} \equiv v dz. \quad (3.35)$$

Using the above equations for the path lengths through a small cross section, we

can determine the change in intensity. If we again consider the light passing downward through the cross section dz , the decrease in intensity over the path length $d\xi_I$ is

$$(\sigma_a + \sigma_s)Id\xi_I = (\sigma_a + \sigma_s)uIdz. \quad (3.36)$$

Similarly, for the light passing upward through dz

$$(\sigma_a + \sigma_s)Jd\xi_J = (\sigma_a + \sigma_s)vJdz. \quad (3.37)$$

With the above assumption that light travels only in one dimension, light scattered from the I direction will augment that traveling in the J direction, and vice versa. The resulting changes in intensities are

$$-dI = -(\sigma_a + \sigma_s)uIdz + \sigma_s v J dz \quad (3.38)$$

$$dJ = -(\sigma_a + \sigma_s)vJdz + \sigma_s u Idz, \quad (3.39)$$

where the signs have been chosen consistent with J increasing, and I decreasing, with z .

Since the material scatters isotropically, the light inside the material has the same intensity in all directions. If we consider the hemisphere of light falling downward on dz , the contribution from each direction φ is $\partial I = \cos \varphi d\vec{\omega}$. The angular distribution of light in the negative \hat{z} direction, relative to a plane perpendicular to the \hat{z} axis, can be found by expanding this to spherical coordinates

$$\frac{\partial I}{\partial \varphi} = 2I_0 \sin \varphi \cos \varphi \quad (3.40)$$

Similarly for upward passing light

$$\frac{\partial J}{\partial \varphi} = 2J_0 \sin \varphi \cos \varphi. \quad (3.41)$$

Substituting these into (3.34) and (3.35), we find that

$$u = \int_0^{\frac{\pi}{2}} 2 \sin \varphi d\varphi = 2 \quad \text{and} \quad v = \int_0^{\frac{\pi}{2}} 2 \sin \varphi d\varphi = 2. \quad (3.42)$$

If we define

$$K = 2\sigma_a \quad \text{and} \quad S = 2\sigma_s, \quad (3.43)$$

then substitution into (3.38) and (3.39) gives

$$-\frac{dI}{dz} = -(K+S)I + SJ, \quad (3.44)$$

$$\frac{dJ}{dz} = -(K+S)J + SI. \quad (3.45)$$

If we divide both equations by S and let

$$a = \frac{K+S}{S} = 1 + \frac{K}{S} \quad (3.46)$$

then we can rewrite these equations as

$$-\frac{dI}{Sdz} = -aI + J, \quad (3.47)$$

$$\frac{dJ}{Sdz} = -aJ + I. \quad (3.48)$$

Dividing the first equation by I , the second by J , and adding the two equations, we find

$$\frac{1}{Sdz} \left(\frac{dJ}{J} - \frac{dI}{I} \right) = -2a + \frac{J}{I} + \frac{I}{J}. \quad (3.49)$$

Making the substitution $r = J/I$, and noting that $I = -J$, this can be rewritten as

$$\frac{dr}{Sdz} = r^2 - 2ar + 1, \quad (3.50)$$

or more importantly

$$\int \frac{dr}{r^2 - 2ar + 1} = S \int dz, \quad (3.51)$$

where we are integrating over the thickness of the layer. Note that $r = J/I$ is the ratio of light leaving the material to that entering the material, which is precisely the reflectance.

Solving Equation (3.51) requires stating a boundary condition for the integration. There are two boundary conditions related to the reflectance at the top and the bottom of the layer

$$z=0 : \left[\frac{J}{I} \right]_{z=0} = R_b = \text{ Reflectance of the background,} \quad (3.52)$$

$$z=d : \left[\frac{J}{I} \right]_{z=d} = R = \text{ Reflectance at the surface.} \quad (3.53)$$

We can now integrate the left side of (3.51) by partial fractions to get

$$\frac{1}{2b} \ln \frac{(R-a-b)(R_b-a+b)}{(R_b-a-b)(R-a+b)} = Sd, \quad (3.54)$$

which can be written in simpler form using the hyperbolic cotangent [73]

$$\coth^{-1} \frac{b^2 - (a-R)(a-R_b)}{b(R-R_b)} = bSd \quad (3.55)$$

Solving (3.55) for the reflectance R gives

$$R = \frac{1 - R_b(a - b \coth bSd)}{a + b \coth bSd - R_b}. \quad (3.56)$$

This expression gives the reflectance of a scattering layer covering a background with reflectance R_b . If the layer is infinitely thick ($d = \infty$), completely obscuring the background ($R_b = 0, R = R_\infty$), (3.56) becomes

$$R_\infty = \frac{1}{a+b} = \frac{a - \sqrt{a^2 - 1}}{a^2 - a^2 + 1} = 1 + \frac{K}{S} + \sqrt{\left(\frac{K}{S}\right)^2 + 2\frac{K}{S}} \quad (3.57)$$

which is a rather simple expression for the subsurface scattering of light from thick materials. If instead the background is ideally black or the layer is suspended in space with no backing at all ($R_b = 0, R = R_0$),

$$R_0 = \frac{1}{a + b \coth bSd} = \frac{\sinh bSd}{a \sinh bSd + b \cosh bSd}. \quad (3.58)$$

The transmittance of the material has similar form. The transmittance is the amount of light I that reaches the background. Recalling that $r = J/I$, for a layer of thickness z

$$J = R_0 I = \frac{I}{a + b \coth bSz}, \quad (3.59)$$

which, when substituted into (3.47) yields

$$-\frac{dI}{Sdz} = -aI + \frac{I}{a + b \coth bSz}. \quad (3.60)$$

We can integrate this expression over the thickness of the layer by first dividing by I and making the substitution $u = bSz$

$$-\frac{1}{S} \int_0^d \frac{dI}{I} = -a \int_0^d dz + \frac{1}{bS} \int_0^d \frac{I}{a + b \coth u} du, \quad (3.61)$$

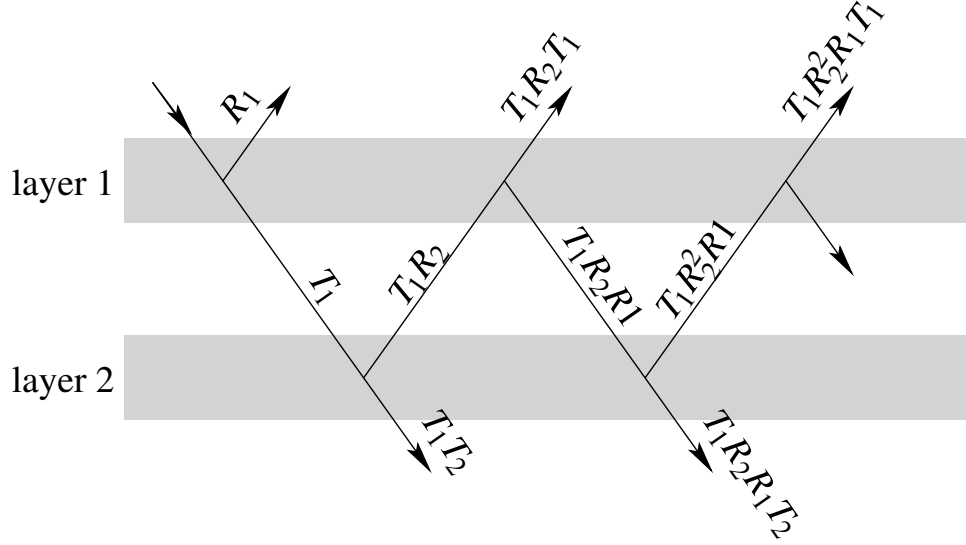


Figure 3.3: Kubelka-Munk reflectance and transmittance for multiple layers. Redrawn from [74].

which simplifies to

$$T = \frac{I_0}{I_d} = \frac{b}{a \sinh bSd + b \cosh bSd}, \quad (3.62)$$

where T , the transmittance, is the ratio of the intensity at d to the incident intensity.

Kubelka-Munk theory can also be applied to multiple layers. Consider the situation in Figure 3.3, where we have two scattering layers on top of each other (the space between them for illustration purposes only). According to Kubelka-Munk theory, if the incident radiance $I_0 = 1$, the amount of light reflected from the top layer will be R_1 , defined by (3.58), while the amount transmitted, T_1 , is from (3.62). The amount of light directly transmitted through both layers is T_1 modulated by the transmittance of layer 2 is T_1T_2 . Similarly, T_1R_2 light reflects up off of the bottom layer, and $T_1R_2T_1$ light will reach the top of layer 1.

Light can reflect between the two layers indefinitely. The total reflectance and transmittance is the sum of all possible inter-reflections [74]

$$R_{1,2} = R_1 + T_1^2 R_2 (1 + R_1 R_2 + R_1^2 R_2^2 + \dots) = R_1 + \frac{T_1^2 R_2}{1 - R_1 R_2} \quad (3.63)$$

$$T_{1,2} = T_1 T_2 (1 + R_1 R_2 + R_1^2 R_2^2 + \dots) = \frac{T_1 T_2}{1 - R_1 R_2} \quad (3.64)$$

The reflectance and transmittance of more than two layers is found by using these expressions as the reflectance and transmittance of a single layer, and substituting them

back in as R_1 and T_1 .

The Kubelka-Munk model has been used extensively in the paint and paper industries for predicting the reflectance of pigment mixtures [65], and was more recently used in the feature film *Shrek* to model the skin of humanoid characters [14]. It has also proved useful in the rendering of weathering phenomenon, such as metallic patinas [24], and in simulating transparent layers of watercolor [19]. The simplicity of the model is its main attraction, and it gives reasonable results for some types of materials [71]. In particular, Kubelka-Munk theory has been popular in the study of canopy and leaf optics.

The model, however, does have limitations. The simple expressions derived above assume that the layers are homogeneous, yet paint molecules, which the Kubelka-Munk model is widely used to simulate, are known to clump together, which affects the overall color [35]. Although not explicitly stated, we also assumed that the scattering layers and the medium above the layers had matched indices of refraction (note that no Fresnel terms appear in the Kubelka-Munk model), which is not always the case.

The assumption that the incident light is perfectly diffuse led in part to the 1D approximation of the transport equation, and the simple expressions for reflectance and transmittance. This assumption, however, makes it difficult to describe the response to a single beam of light. In particular, for computer graphics, where incident light is generally described as incident rays, this makes it difficult to use this technique for simulating materials.

Kubelka and Munk's model also suffers from the same drawback as the Hanrahan-Krueger model; light exits the material at the same point it enters. This implies that the Kubelka-Munk model cannot simulate lateral color bleeding, or light bleeding into shadows. Still, this limitation is what gives the solutions their elegant simplicity.

Chapter 4

Monte Carlo methods

As we have seen, BRDF models are not suited to simulating light transport in scattering materials. At the other end of the spectrum from them are Monte Carlo techniques. These rely on simulation of the paths light takes in a scattering material to obtain reflectance and transmittance. Though a complete introduction to Monte Carlo methods is beyond the scope of this dissertation, this Chapter briefly discusses some existing methods as they relate to translucent materials. These approaches are general and capable of simulating translucent materials, but they are computationally costly for highly scattering materials.

4.1 Path tracing

One of the most brute force methods for simulating light transport in scattering materials is path tracing. Originally introduced by Kajiya [66], path tracing traces rays from the camera into the scene, and randomly constructs a path that contributes to a pixel only if the ray encounters a light source. Path tracing is slow to converge in general, even when importance sampling is used to minimize the number of traced rays. Russian Roulette also reduces the number of paths to trace by probabilistically deciding whether to scatter or absorb the ray based on the albedo. For highly scattering materials, a ray may undergo many scattering events before exiting the material, and its exit direction will be randomized. It is therefore unlikely that a ray would hit a light source.

Reversing the direction of the rays gives packet tracing [92]. Photons are launched from light sources and scattered in the material until they are absorbed or reach a detector (or camera). Alternatively, photons are stored where they exit the material to give a distribution of radiant exitance at the surface.

Despite these drawbacks, path tracing has been used to develop light models for translucent materials. Jensen et al. [61] used path tracing to model the darkening of wet materials by tracing rays through a layer of water at the surface. More recently, Baranoski and Rokne [5] and Krishnaswamy and Baranoski [72] have modeled the small scale structures of plant leaves and skin, and generated images using path tracing. While these methods are robust and comprehensive, they are computationally extremely expensive.

4.2 Bidirectional path tracing

To improve the efficiency of path tracing, LaFortune [76] and Veach [117] in parallel developed *bidirectional* path tracing, which has also been extended to participating media [77]. To alleviate the problem of exitant rays from a scattering medium being unlikely to hit a light source, in bidirectional path tracing two paths are traced, one from the camera, and one from the light source. These path represents a family of possible paths from light to camera; each vertex from the light path is connected to each vertex of the camera path, and weighted appropriately to improve the convergence rate of the algorithm. Unfortunately, the weights of each path depend on the inverse distance between vertices. In highly scattering materials, this distance can be very small, which causes the solution to be singular. Overall, the high computational cost (though still better than pure path tracing) and possible singularities make bidirectional path tracing a poor candidate for rendering translucent materials.

4.3 Photon mapping

Somewhat related to bidirectional path tracing and packet tracing, *photon mapping* connects light paths to eye paths by depositing photons from light sources on surfaces,

and then adding the contributions of these photons when camera rays intersect visible surfaces [57, 58]. Photons are traced from light sources similar to the standard packet tracing algorithm [92]. They are stored in a *photon map*, usually a *kd-tree*, for efficient access. In the case of scattering materials, photons are stored in a volume photon map at every scattering event [60]. During rendering, camera rays are traced into the material, and the contribution of nearby scattered photons is summed.

Photon mapping has been used by Dorsey et al.. [23] to simulate the effects of weathering on stone, as well as the subsurface scattering of light in materials like marble. Unfortunately, however, for highly scattering materials, photon mapping requires a large number of photons to be stored, and can quickly consume large amounts of memory.

Chapter 5

Subsurface scattering of light using diffusion

Full 3D light transport is simulated accurately by standard Monte Carlo simulation, but there can be variance in the final solution if insufficient samples are used [23], and the high computational cost is generally undesirable. More sophisticated caching techniques such as photon mapping are also available, but can require large amounts of storage for highly scattering materials [60]. An analytical solution to the problem of 3D light transport that preserves accuracy while remaining efficient is what is missing in the models already discussed in this dissertation. Application of diffusion theory leads to such a solution.

As discussed earlier in this dissertation, BRDF models either assume that light does not penetrate into the material, or use simple 1D solutions to the radiative transfer equation, explicitly assuming that light enters and exits the material in the same location. While this makes the problem of light transport more tractable, these models neglect light that enters the material, scatters around, and exits in another location. It is this type subsurface scattering that causes the soft translucent appearance of many materials. Diffusion theory, which this chapter discusses, deals with a full 3D solution to radiative transfer, and accurately captures this scattering phenomenon [25]. Diffusion theory does have its limiting assumptions, however. Specifically, we must assume the material is optically thick, and that it is highly scattering ($\sigma_s \gg \sigma_a$).

5.1 Introduction

Diffusion theory leads to a well known result in physics, the diffusion approximation, but was only recently introduced fully to computer graphics. The complex mathematics involved make diffusion theory a particularly difficult concept to understand, which may explain the lack of enthusiasm early attempts to make the graphics community aware of it received [104].

Jensen et al. [62] re-introduced the diffusion approximation to the graphics community in the form of a *bidirectional scattering surface distribution function* (BSSRDF) [85]

$$S_d(\vec{x}_i, \vec{\omega}_i; \vec{x}_o, \vec{\omega}_o) = \frac{1}{\pi} F_t(\vec{x}_i, \vec{\omega}_i) R(r) F_t(\vec{x}_o, \vec{\omega}_o). \quad (5.1)$$

where F_t is the Fresnel transmittance at the entry and exit locations \vec{x}_i and \vec{x}_o , $r = ||\vec{x}_i - \vec{x}_o||_2$, $\vec{\omega}_i$ and $\vec{\omega}_o$ are the incident and exitant directions, and the diffuse reflectance, R , is approximated by a diffusion dipole, which we will describe later in this chapter. The material is characterized by its scattering and absorption coefficients, and its phase function. In the physical world, these parameters often vary spatially, though in practice they are often held constant throughout the material. In this chapter, we assume that the material is completely homogeneous to ease in deriving the basic formulas, though later we will soften this restriction slightly.

In this chapter we derive the diffusion dipole model starting from the basic physics of light transport, to give a good understanding of the inner workings of the model. We begin by deriving the diffusion equation similar to Ishimaru [51] and Prahl [91], but we explicitly show the steps involved and give motivations for the approximations made to give a more complete picture. We then explore the details that lead to the dipole approximation.

Although rigorous solutions to both the radiative transport equation and the diffusion equation do exist [15, 34, 51, 127], they are expensive to compute, often on the order of performing a full Monte Carlo particle simulation. As this section will show, some simple approximations can simplify the computation while still preserving accuracy and plausibility in most situations. The diffusion approximation has its roots in nuclear physics, where radiative transport describes the scattering of neutrons. Finding the full

story leading from radiative transport through the dipole approximation to the diffusion dipole in the literature, however, leads one through the dense realms of optical, medical, and nuclear physics.

5.2 The delta-Eddington approximation

We derive the diffusion approximation similar to Prahl [91] and Moulton [83], and use the delta-Eddington phase function for its simplicity. Although the popular Henyey-Greenstein phase function can also be used, the delta-Eddington phase function makes the derivation simpler. First, recall the full radiative transport equation (Equation 2.10) in the case of an infinite medium

$$\frac{dL(r, \vec{\omega})}{dz} = -\sigma_t L(r, \vec{\omega}) + \sigma_s \int_{4\pi} p(\vec{\omega}, \vec{\omega}') L(r, \vec{\omega}') d\vec{\omega}',$$

where the change in radiance is a combination of loss due to scattering and absorption, plus light scattered into the $\vec{\omega}$ direction, and r is the distance from a single source within the medium.

Substituting the delta-Eddington phase function into Equation 2.10 and expanding the extinction coefficient σ_t gives

$$\frac{dL(r, \vec{\omega})}{dz} = -\sigma_a L(r, \vec{\omega}) - \sigma_s(1-f)L(r, \vec{\omega}) + \frac{\sigma_s}{4\pi} \int_{4\pi} L(r, \vec{\omega}') (1-f)(1+3g'\vec{\omega} \cdot \vec{\omega}') d\vec{\omega}'. \quad (5.2)$$

If we define

$$\sigma'_s = \sigma_s(1-f) \quad \text{and} \quad \sigma'_t = \sigma_a + \sigma'_s \quad (5.3)$$

and combine like terms then

$$\frac{dL(r, \vec{\omega})}{dz} = -\sigma'_t L(r, \vec{\omega}) + \frac{\sigma'_s}{4\pi} \int_{4\pi} L(r, \vec{\omega}') (1+3g'\vec{\omega} \cdot \vec{\omega}') d\vec{\omega}'. \quad (5.4)$$

σ'_s is called the *reduced scattering coefficient*, while $\sigma'_t = \sigma'_s + \sigma_a$ is the *reduced extinction coefficient*. They indicate that the portion of light that is not scattered in the $\vec{\omega}$ direction is reduced by $1-f$; this light is scattered out of the collimated beam and into the diffuse portion of the radiance. Note that Equation 5.4 has nearly the same form as Equation 2.10, but with reduced coefficients. By the principle of *similarity*, we use these

reduced coefficients and assume isotropic scattering without significantly altering the solution [131]. Physically, we are lengthening or shortening the distance traveled by scattered light by $1 - f$, which after many scattering events is similar to the effect of an anisotropic phase function.

Recall from Equation 2.2 that the radiance can be separated into two components, the reduced incident radiance, and the diffuse radiance. The reduced intensity can be calculated directly from Equation 2.4, accounting for Fresnel transmission at the surface.

As discussed in Chapter 2, we separate incident radiance into the reduced intensity and the diffuse radiance

$$L(r, \vec{\omega}) = L_{ri}(r, \vec{\omega}) + L_d(r, \vec{\omega}).$$

In this Chapter, we focus our attention to the second term of Equation 2.2, or the *multiple scattered* light. To find the diffuse radiance, consider the change in diffuse radiance over a small distance dz . This includes loss due to absorption and scattering (a) and the addition of diffuse and in-scattered radiance (b). In addition, previously unscattered reduced incident light is scattered *into* the diffuse portion from all directions (c)

$$\begin{aligned} \frac{dL_d(r, \vec{\omega})}{dz} &= \underbrace{-\sigma'_t L_d(r, \vec{\omega})}_{(a)} + \underbrace{\frac{\sigma'_s}{4\pi} \int_{4\pi} L_d(r, \vec{\omega}') (1 + 3g' \vec{\omega} \cdot \vec{\omega}') d\vec{\omega}'}_{(b)} \\ &\quad + \underbrace{\frac{\sigma'_s}{4\pi} \int_{4\pi} p(\vec{\omega}, \vec{\omega}') T \Phi(r) e^{-\sigma'_t z/\mu_0} \delta(\mu - \mu_0) d\vec{\omega}'}_{(c)}, \end{aligned} \quad (5.5)$$

where T is the Fresnel transmittance at the surface. Since the delta function in the reduced intensity is only non-zero when $\mu = \mu_0$, the first term of the delta-Eddington phase function in Equation 5.5c goes to zero. If we also assume that the scattering is symmetric ($g' = 0$), then

$$\frac{dL_d(r, \vec{\omega})}{dz} = -\sigma'_t L_d(r, \vec{\omega}) + \frac{\sigma'_s}{4\pi} \int_{4\pi} L_d(r, \vec{\omega}') d\vec{\omega}' + \frac{\sigma'_s}{4\pi} T \Phi(r) e^{-\sigma'_t z/\mu_0}. \quad (5.6)$$

5.3 Deriving the diffusion equation

Our goal is to find a solution for the diffuse radiance given in Equation 5.6, since the reduced intensity is calculated directly. If we assume that the material has high albedo ($\sigma_s \gg \sigma_a$) that scatter the incident light rays many times, then after many interactions, the light distribution will become randomized, or diffuse [104]. We approximate the diffuse radiance in Equation 5.6 by a finite real spherical harmonic expansion

$$L_d(r, \vec{\omega}) \approx \sum_{n=0}^N \sum_{m=-n}^n \left(\frac{2n+1}{4\pi} \right)^{\frac{1}{2}} L_n^m(r) y_n^m(\vec{\omega}). \quad (5.7)$$

With $N = 1$ (often called the P_1 approximation), we get the following expansion

$$L_d(r, \vec{\omega}) \approx \frac{1}{\sqrt{4\pi}} L_0^0(r) y_0^0(\vec{\omega}) + \sqrt{\frac{3}{4\pi}} \sum_{m=-1}^1 L_1^m(r) y_1^m(\vec{\omega}). \quad (5.8)$$

The real spherical harmonic terms are

$$\begin{aligned} y_0^0 &= \frac{1}{\sqrt{4\pi}} \\ y_1^{-1} &= \sqrt{\frac{3}{4\pi}} \sin \theta \cos \phi \\ y_1^0 &= \sqrt{\frac{3}{4\pi}} \cos \theta \\ y_1^1 &= \sqrt{\frac{3}{4\pi}} \sin \theta \sin \phi. \end{aligned}$$

We can consider the y_1^m terms as describing a vector in space, and write the following expression, composed of a scalar term ϕ and a vector term \mathbf{E}

$$L_d(r, \vec{\omega}) \approx \frac{1}{4\pi} \phi(r) + \frac{3}{4\pi} \mathbf{E}(r) \cdot \vec{\omega}. \quad (5.9)$$

The scalar term is called the *fluence* and represents the isotropic flux, defined as

$$\phi(r) \equiv L_0^0(r) = \int_{4\pi} L_d(r, \vec{\omega}) d\vec{\omega}. \quad (5.10)$$

The fluence can be thought of as the average amount of light entering a small volume in the medium. The vector term, called *vector irradiance* or *vector flux*, represents the

anisotropic flux in a direction $\hat{\mathbf{s}}_f$, and can be thought of as the net photon current at a point in the material

$$\mathbf{E}(r) \equiv \begin{bmatrix} L_1^{-1}y_1^{-1}(r) \\ L_1^1y_1^1(r) \\ L_1^0y_1^0(r) \end{bmatrix} = \int_{4\pi} L_d(r, \vec{\omega}) \vec{\omega} d\vec{\omega}. \quad (5.11)$$

Each component of the vector is the value of one of the first order radiance expansion terms, and thus the dot product represents the sum of the three first order terms. Equation 5.9 can also be interpreted as the sum of the first two moments of the radiance.

Rewriting the left side of the diffuse radiance equation (Equation 5.6) as a gradient

$$(\vec{\omega} \cdot \nabla)L_d(r, \vec{\omega}) = -\sigma'_t L_d(r, \vec{\omega}) + \frac{\sigma'_s}{4\pi} \int_{4\pi} L_d(r, \vec{\omega}') d\vec{\omega}' + \frac{\sigma'_s}{4\pi} T\Phi(r)e^{-\sigma'_t z/\mu_o}, \quad (5.12)$$

and substituting the diffuse radiance approximation Equation 5.9 in for L_d on both sides of Equation 5.12 gives

$$(\vec{\omega} \cdot \nabla)\phi(r) + 3(\vec{\omega} \cdot \nabla)[\mathbf{E}(r) \cdot \vec{\omega}] = -\sigma_a\phi(r) - 3\sigma'_t[\mathbf{E}(r) \cdot \vec{\omega}] + \sigma'_s T\Phi(r)e^{-\sigma'_t z/\mu_o}. \quad (5.13)$$

We now have an expression that depends only on the fluence and vector flux. Integrating Equation 5.13 over all directions and simplifying gives

$$\nabla \cdot \mathbf{E}(r) = -\sigma_a\phi(r) + \sigma'_s T\Phi(r)e^{-\sigma'_t z/\mu_o} \quad (5.14)$$

This expression indicates that the change in diffuse flux is due to the absorption of scalar flux and in-scattered collimated light. Multiplying both sides of Equation 5.13 by $\vec{\omega}$ before integrating gives

$$\nabla\phi(r) = -3\sigma'_t\mathbf{E}(r). \quad (5.15)$$

Recall that our goal is to find the diffuse radiance at the surface of the material, and thus the reflectance. This is equivalent to finding the radiant exitance in the direction of the normal at the surface. This quantity can also be thought of as the photon current out of the material, which from our definition of flux density is precisely $E(r) = \mathbf{E}(r) \cdot \vec{n}$. Since the normal is pointing in the $-\hat{\mathbf{z}}$ direction we rewrite this as $E(r) = -\mathbf{E}(r) \cdot \hat{\mathbf{z}}$. If we assume we are far from the surface of the material where the light is incident

$$\mathbf{E}(r) = -\frac{1}{3\sigma'_t}\nabla\phi(r). \quad (5.16)$$

Dotting both sides with $-\hat{\mathbf{z}}$ gives

$$E(r) = \mathbf{E}(r) \cdot \vec{n} = -D(\nabla \cdot \hat{\mathbf{z}})\phi(r) = -D \frac{d\phi(r)}{dz} \quad (5.17)$$

where $D = \frac{1}{3\sigma'_t}$ is the *diffusion constant*. This states that the net flux, or current, is in the opposite direction of the net change in scalar flux. Effectively, it means that light travels away from areas of high concentration (*e.g.* sources). Thus, we approximate the radiant exitance, and thus the reflectance, by getting a closed form expression for the fluence and then just taking the derivative.

5.3.1 The diffusion equation

To get an expression only in terms of the fluence, take the divergence of Equation 5.15 to obtain

$$\nabla \cdot \mathbf{E}(r) = -\frac{1}{3\sigma'_t} \nabla^2 \phi(r). \quad (5.18)$$

Equating Equations 5.14 and 5.18 and simplifying gives the classic diffusion equation

$$\nabla^2 \phi(r) - \sigma_{tr}^2 \phi(r) = -3\sigma'_s \sigma'_t T \Phi(r) e^{-\sigma'_t z / \mu_o}, \quad (5.19)$$

where $\sigma_{tr}^2 = 3\sigma'_t \sigma_a$ is the *effective transport coefficient*. This expression is used to find the average diffuse flux, and thus the diffuse radiance. Note that the right hand side represents the collimated beam source. If we were to use a different source function, the right hand side would change.

5.3.2 Solution for a point source in an infinite medium

A simple solution exists to the diffusion equation in the case of a point source in an infinite medium, again assuming that the medium is highly scattering and scatters uniformly and isotropically. Since there is no collimated beam, the diffusion equation (Equation 5.19) becomes [36]

$$\nabla^2 \phi(r) - \sigma_{tr}^2 \phi(r) = 0 \quad (5.20)$$

The one boundary condition to this equation is that fluence decreases the further we move from the source

$$\lim_{r \rightarrow \infty} \phi(r) = 0 \quad (5.21)$$

Equation (5.20) is solved by expanding the Laplacian operator into spherical coordinates. Because we are assuming isotropy, however, there is spherical symmetry and the angle dependant terms go to zero, leaving

$$\frac{d^2\phi(r)}{dr^2} + \frac{2}{r} \frac{d\phi(r)}{dr} - \sigma_{tr}^2 \phi(r) = 0, \quad (5.22)$$

where r is the distance from the point source. This expression has a simple solution

$$\phi(r) = \frac{\Phi}{4\pi D} \frac{e^{-\sigma_{tr}r}}{r}. \quad (5.23)$$

where again $\sigma_{tr} = \sqrt{3\sigma_t'\sigma_a}$.

5.3.3 Semi-infinite material

If all we wanted to do was render infinitely extending volumes, we could use the point source fluence directly to find the diffuse radiance. For surfaces, however, we make the assumption that the material is semi-infinite below the surface. In this case, we assume that the diffuse radiance at the surface of the material is due only to scattered light leaving the material. That is, diffuse light that exits the material at the surface never comes back, so there is no diffuse radiance going in the $\hat{\mathbf{z}}$ direction at the surface. We state this mathematically as an integral over the positive hemisphere

$$\int_{\Omega^+} L_d(r, \vec{\omega})(\hat{\mathbf{z}} \cdot \vec{\omega}) d\vec{\omega} = 0 \quad \text{at } z = 0, \quad (5.24)$$

where again $\hat{\mathbf{z}}$ is directed into the slab in the direction opposite its normal. The $(\hat{\mathbf{z}} \cdot \vec{\omega})$ term projects the radiance into the slab. Substituting the approximation for the diffuse radiance (Equation 5.9) into Equation 5.24 gives

$$\phi(r) - 2D \frac{\partial \phi(r)}{\partial z} = 0 \quad (5.25)$$

where $D = \frac{1}{3\sigma_t'}$ as before.

5.3.4 Diffuse internal reflectance

Unfortunately, the above boundary condition does not take into account light internally reflected at the surface. This happens when the scattering material and the non-scattering material above it do not have the same index of refraction (a very common occurrence). A more realistic boundary condition notes that the diffuse radiance in the $-\hat{\mathbf{z}}$ direction is equal to the diffuse incident radiance reflected down at the surface in the $\hat{\mathbf{z}}$ direction [39]

$$\int_{\Omega^+} L_d(r, \vec{\omega}) (\hat{\mathbf{z}} \cdot \vec{\omega}) d\vec{\omega} = \int_{\Omega^-} F_{dr} L_d(r, \vec{\omega}) (-\hat{\mathbf{z}} \cdot \vec{\omega}) \quad \text{at } z=0, \quad (5.26)$$

where F_{dr} is the internal Fresnel reflectivity of the slab. Since the light distribution is assumed to be diffuse due to multiple scattering, however, we assume that there is no dependence on the angle of incidence. This diffuse reflectivity is often approximated with a simple polynomial expansion [28, 39]

$$F_{dr} \simeq \begin{cases} -0.4399 + \frac{0.7099}{\eta} - \frac{0.3319}{\eta^2} + \frac{0.0636}{\eta^3}, & \eta < 1 \\ -\frac{1.4399}{\eta^2} + \frac{0.7099}{\eta} + 0.6681 + 0.0636\eta, & \eta > 1 \end{cases} \quad (5.27)$$

where η is the ratio of indices of refraction. Equation (5.26) simplifies with Equation (5.9)

$$\phi(r) - 2AD \frac{\partial \phi(r)}{\partial z} = 0, \quad (5.28)$$

where

$$A = \frac{1 + F_{dr}}{1 - F_{dr}}, \quad (5.29)$$

takes into account the effects of internal diffuse reflection.

5.4 Approximate boundary condition

Unfortunately, the above surface boundary condition is a Robin (or type III) condition, in this case difficult to solve analytically or efficiently. We approximate it fairly well, however, using a simpler condition.

Note that boundary condition in Equation 5.28 is the net *inward* flux. The net *outward* flux has the form

$$\phi_0 + 2AD \frac{\partial \phi(r)}{\partial z} = 0, \quad (5.30)$$

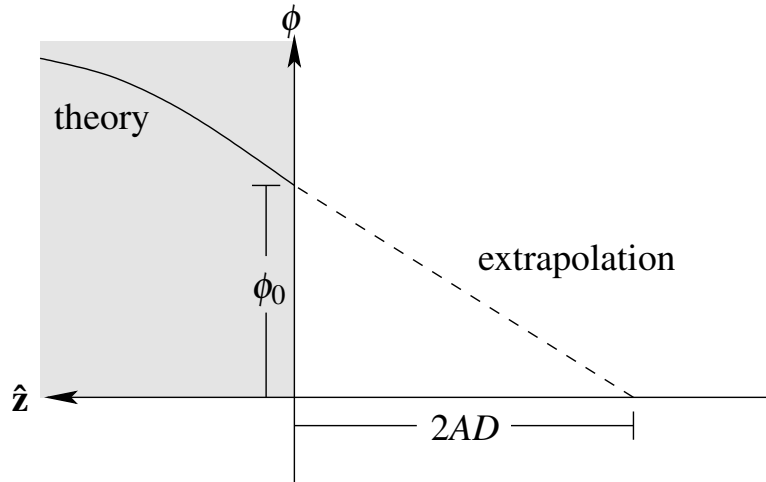


Figure 5.1: Extrapolated fluence.

where, ϕ_0 is the flux at the boundary. We extrapolate the flux beyond the boundary by rearranging

$$\frac{\partial \phi(r)}{\partial z} = -\frac{\phi_0}{2AD}. \quad (5.31)$$

If we assume that the flux decreases linearly outside the diffusing material, then the slope of the line is $-\phi_0/(2AD)$ (Figure 5.1). The flux will vanish at a distance $2AD$ beyond the boundary [36]. Thus, we approximate our surface boundary conditions with the simple Dirichlet condition

$$\phi(2AD) = 0 \quad (5.32)$$

This distance $2AD$ above the surface is called the *extrapolation distance* or *extrapolated boundary* [32, 36].

5.5 The diffusion dipole approximation

In the previous sections we derived a simplified diffusion equation by assuming isotropic scattering in a highly scattering homogeneous material. We found that determining the flux directed out of the material at its surface is enough to find the photon current exiting the material. In this section we put all the pieces together to construct the diffusion dipole model and approximate the reflectance with the BSSRDF.

Equation 5.32 states that the fluence vanishes at $2AD$ above the surface. This condition is satisfied using the method of images. A positive source is embedded within the medium, with a virtual negative source mirrored about the extrapolated boundary. Since having the sources any distance from the boundary –so long as the two sources are equidistant to it and along the normal direction–, the question is how far away should they be?

If the semi-infinite material is highly scattering and scatters isotropically, the light distribution will start to become randomized after about one mean free path (the average distance light travels before an interaction occurs). We approximate an incident ray of illumination with a point source embedded at a depth of one mean free path ($z_r = 1/\sigma'_t$) [32, 87]. The point source has the same intensity as the incident illumination.

To then satisfy Equation 5.32, we place a virtual source above the real source, mirrored about the extrapolated boundary at a height $z_v = z_r + 4AD$ above the surface (see Figure 5.2). The sum of the flux from both sources gives zero at the extrapolated boundary. Again, $D = 1/(3\sigma'_t)$, and $A = \frac{1+F_{dr}}{1-F_{dr}}$. The total fluence is the sum of the individual contributions from the positive real source and its virtual mirror

$$\phi(r) = \frac{\Phi}{4\pi D} \left(\frac{e^{-\sigma_{tr}d_r}}{d_r} - \frac{e^{-\sigma_{tr}d_v}}{d_v} \right), \quad (5.33)$$

where d_r and d_v are distances from r to the source and mirror source, respectively

$$\begin{aligned} d_r &= \sqrt{r^2 + z_r^2} \\ d_v &= \sqrt{r^2 + z_v^2}. \end{aligned} \quad (5.34)$$

r is the lateral distance relative to the center point of the sources, and z is the depth of r (Figure 5.2). Φ is the irradiance at the illuminated point \vec{x}_i .

Using Equations 5.17 and 5.33, dividing by the incident flux, we obtain the diffuse reflectance of the BSSRDF (Equation 5.1) using the diffusion dipole approximation as presented in [32, 62]

$$\begin{aligned} R_d(r) &= -D \frac{d}{dz} \left[\frac{1}{4\pi D} \left(\frac{e^{-\sigma_{tr}d_r}}{d_r} - \frac{e^{-\sigma_{tr}d_v}}{d_v} \right) \right] \\ &= \frac{\alpha'}{4\pi} \left[\frac{z_r(1 + \sigma_{tr}d_r)e^{-\sigma_{tr}d_r}}{d_r^3} + \frac{z_v(1 + \sigma_{tr}d_v)e^{-\sigma_{tr}d_v}}{d_v^3} \right], \end{aligned} \quad (5.35)$$

where $\alpha' = \sigma'_s/\sigma'_t$ is the *reduced albedo*.

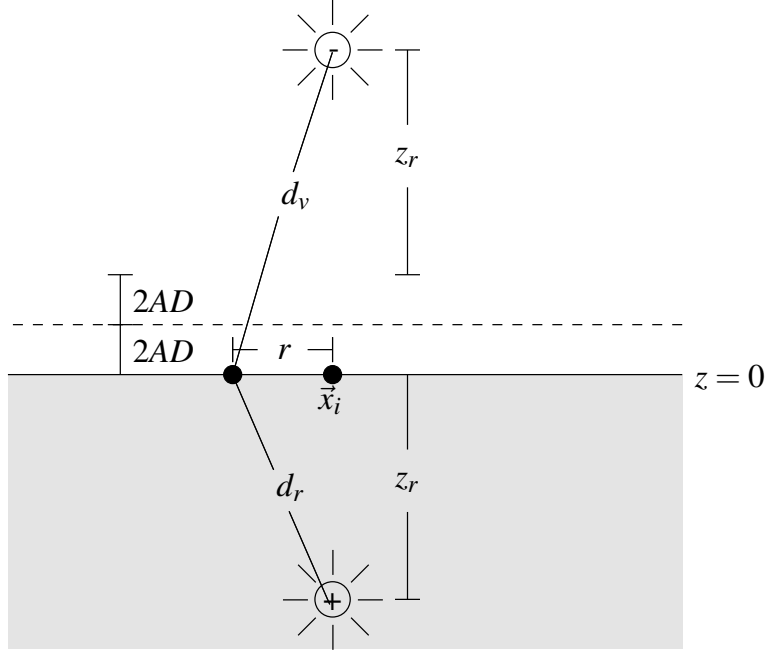


Figure 5.2: An incident ray of light is converted into a real source embedded in the material, and a virtual source mirrored about the extrapolated boundary at $2AD$ above the surface. The total fluence is the sum of the fluences of the two sources.

A sample plot of radiant exitance vs. radial distance is shown in Figure 5.4. The falloff of radiant exitance is quite steep, somewhat resembling a Gaussian in log-space. We refer to this plot as a *diffusion profile* or *diffusion kernel*. The diffuse radiance is approximated by constructing a dipole at many points \vec{x}_i near \vec{x}_o (the point of interest), and summing their contributions by evaluating Equation 5.35 to find $R(\|\vec{x}_o - \vec{x}_i\|)$. This summation approximates the integral over the surface

$$R(r) = \int_0^\infty R_d(r)r dr \quad (5.36)$$

which is the reflectance in the BSSRDF (Equation 5.1).

Light that exits the material near the source is largely due to single scattering. Single scattered light is directly evaluated by tracing refracted rays into the material and computing the reduced intensity (Equation 2.4), attenuating along both the incident and exitant directions. This allows in part internal features of the material to cast volumetric shadows



Figure 5.3: The diffusion dipole can simulate the complex appearance of translucent materials. Images used with permission.

within the object. The amount of single scattering is approximated by assuming that the scattering material and the surrounding medium have the same index of refraction. Using Snell's Law (Equation 2.17), the distance light travels from the scattering event to the surface is

$$s'_i = s_i \frac{|\vec{\omega}_i \cdot \vec{n}_i|}{\sqrt{1 - \left(\frac{1}{\eta}\right)^2 (1 - |\vec{\omega}_o \cdot \vec{n}_o|)}}^{\dagger} \quad (5.37)$$

where s_i is the observed distance, and s'_i is the estimated refracted distance. The amount of light scattered out is the amount of incident light scattered once, and attenuated along both the incident and exitant paths.

5.6 Discussion

By sampling incident light over the surface, the diffusion dipole simulates light that enters the material, scatters multiple times, and exits the material in a different location,

[†]Note that this equation appears incorrectly in [62] as $s'_i = s_i \frac{|\vec{\omega}_i \cdot \vec{n}_i|}{\sqrt{1 - \left(\frac{1}{\eta}\right)^2 (1 - |\vec{\omega}_i \cdot \vec{n}_i|)}}$

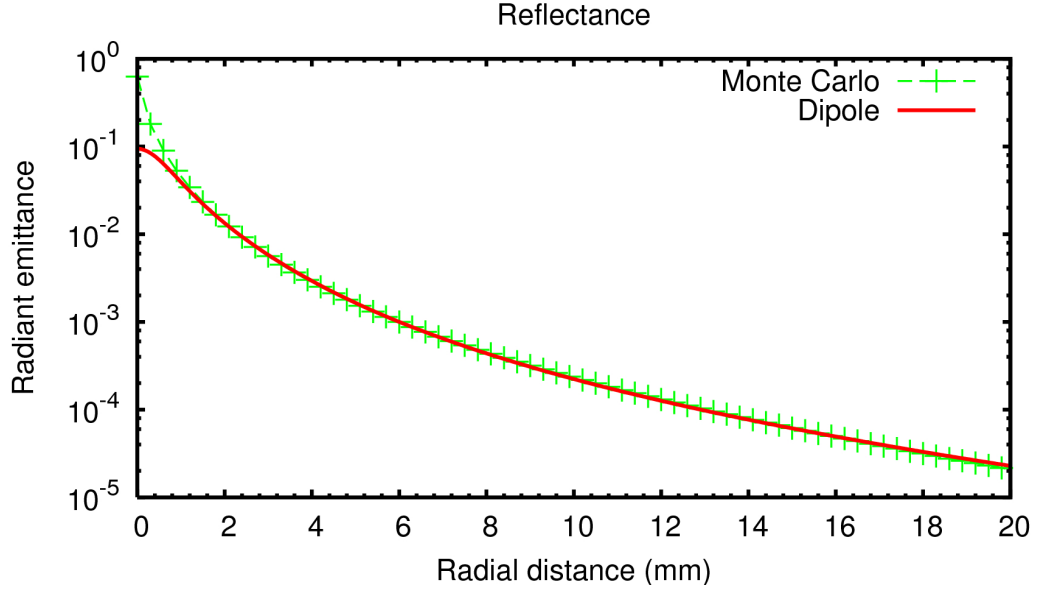


Figure 5.4: An example plot of a diffusion profile of a highly scattering material. The plot shows reflected radiant emittance vs. radial distance, comparing the dipole reflectance to a Monte Carlo simulation.

something that is impossible to simulate correctly with previous BRDF models (for example, see Figure 5.3). The dipole model well approximates the diffuse radiance from optically thick, highly scattering, homogeneous materials. It can be efficiently implemented, and compares well to ground truth Monte Carlo path tracing simulations.

The dipole does have its limitations, however. Recall that the approximations made above assumed that the material has a high albedo. Although the diffusion dipole is quite accurate for high albedo materials, it is less so as the albedo decreases. Figure 5.5 compares the reflectance profile of semi-infinite materials with different albedos to Monte Carlo packet tracing simulations. Note that as the albedo decreases, the effectiveness of the dipole approximate decreases with it [32, 86]. This is intuitively correct, light does not “diffuse” very far in a material that is highly absorbent, or in one that hardly scatters at all. The problem is with the assumption that light is diffusely scattered one mean free path below the surface. This same problem is also evident in low scattering materials, even in the case of high albedo, as the near-source inaccuracies of the dipole

are accentuated.

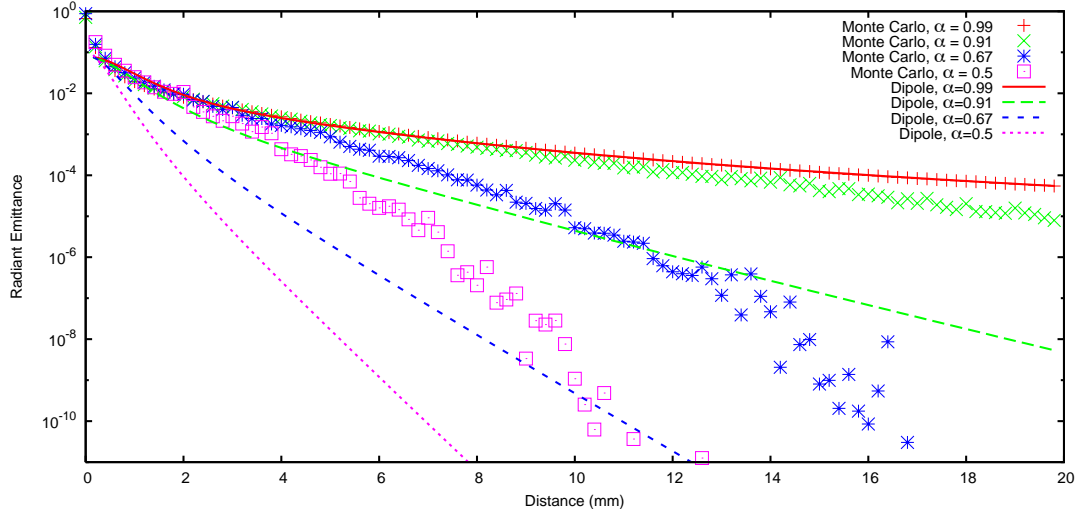


Figure 5.5: Dipole diffusion profiles compared to Monte Carlo photon packet tracing for various albedos. Note that the dipole becomes increasingly more inaccurate as the albedo decreases.

Recall that the diffusion dipole approximation is derived for a semi-infinite medium. In the case of a thin slab, in particular one with a thickness of only a few mean free paths, light may exit the bottom of the slab instead of scattering back to the top surface. The dipole cannot predict this situation. We will explore this limitation in further detail in Chapter 7.

The parameters to the dipole are difficult to determine when trying to simulate real materials. In particular, manually choosing parameters is challenging, as the dipole represents a non-linear transform of the input optical properties to the output diffusion profile. This makes intuitively predicting the reflectance given a set of parameters difficult. This issue is explored in Chapter 8.

The dipole approximation is not a volumetric technique, it assumes that the material is completely homogeneous. This precludes the simulation of light in layered materials (discussed in the next Chapter), and also prevents the embedding of objects within a scattering material. Though the single scattering approximation described above would capture some volumetric shadowing or reflection from embedded objects, any loss from

multiple scattering would be ignored. In addition, for low-scattering materials, the single scattering approximation becomes significantly invalid when there is an actual index of refraction mismatch at the surface.

Despite these few drawbacks, the dipole gives good results for high albedo, optically thick materials, which encompasses a wide range of physical objects, such as skin, milk, and marble. It requires minimal storage (only the space for a diffusion profile, if necessary), and is significantly faster than Monte Carlo methods [62]. The dipole approximation is also useful for measuring optical parameters from highly scattering materials [32, 62, 64, 129].

Chapter 6

Hybrid methods

The efficiency of the diffusion dipole makes it an attractive technique, but it is inaccurate for low albedo materials and near the source. Also, diffusion is limited to homogeneous materials. In this Chapter we discuss recent attempts to couple diffusion with other techniques to improve its accuracy and extend it a broader range of materials. Although there has also been recent work related to directly applying measured properties of translucent materials to objects similar to texture mapping [37, 88], in this Chapter we restrict ourselves to actual reflection models.

6.1 Diffusion and packet tracing

Wang and Jacques [123] and Wang [122] have introduced a hybrid method that couples the packet tracing Monte Carlo method with the diffusion dipole. This technique was introduced to the graphics community by Li et al. [40]. Here, photons are traced from the light and into the material, as in a normal packet tracing simulation. Once a photon reaches a certain depth (usually one mean free path) and does not return on the next step of the simulation, it becomes a positive pole of a diffusion dipole source with a power equal to the energy transported by that photon. Thus, photons that trace deeply into a material likely to scatter many times, and the diffusion approximation becomes applicable.

The hybrid method improves significantly on the accuracy of diffusion near the

source, giving results indistinguishable from a full Monte Carlo simulation [123]. The technique also works for think slabs, effectively giving a more general method for light scattering in translucent materials. Unfortunately, as slab thickness decreases, and also for low albedo materials, photons may have to travel further from the source before diffusion can be applied, and the computational expense of the method also increases. In addition, the method is only valid for single slabs, and cannot handle any significant heterogeneity (such as layers).

6.2 Diffusion and photon mapping

Chen et al. [16] were motivated by the problem of simulating translucent materials with heterogeneities near the surface. They measured the spatially varying surface reflectance using a shell texture function (STF). Chen et al. argued similarly to Wang and Jacques [123] that light that penetrates deeply into the material undergoes more scattering, and is thus more diffuse. Light that scatters near the surface is described by the STF, a volume composed of voxels. The properties of each voxel are determined in part by manually choosing parameters, and in part through a complex 3D scanning process. This gives a local albedo, phase function, and extinction coefficient for each voxel, which completely determines the optical properties. Light transport in the STF region is simulated using volumetric photon mapping from light sources uniformly distributed around the upward and downward hemispheres, thus depositing power in the voxels. This implicitly assumes that the local lighting over a surface is uniform. During rendering, camera rays are ray-marched through the STF region until they reach two mean free paths into the material. The remaining radiance is computed by sampling using rays from the light and using the dipole approximation. An additional photon tracing path is required to correct for lighting near shadow boundaries, i.e. when the lighting is not uniformly incident.

Similar to the hybrid method, calculating the STF can be an expensive process, as it requires at least one photon tracing step as a precomputation, and possibly another expensive step near shadow boundaries. The STF, however, is able to capture local

heterogeneities in the material, while diffusion cannot. The STF method still assumes that the inner core of the material is semi-infinite, as it relies on the diffusion approximation.

6.3 Diffusion and texture functions

Tong et al. [108] found a different way to model local heterogeneity in translucent materials by coupling bidirectional texture functions (BTF) [20] with the diffusion dipole. Their goal was to develop a model that reproduced data measured with a fairly sophisticated setup. A BTF encodes the appearance of a local surface patch under the hemisphere of viewing and lighting directions, and includes local texture and normal data. To extend the BTF to model the transport from an incident point to a different exitant point, Tong et al. split a small area around a point into two parts, a local area that contains heterogeneities, and a global area surrounding the local area that is homogeneous. Similar to the above methods, light that is incident far from an exitant point is more likely to undergo multiple scattering, and is well approximated by the diffusion dipole. The parameters to the dipole are acquired by fitting measured data to the dipole function. Incident light near an exitant point, however, is modulated by mesostructure functions, similar to a BRDF, also acquired through direct measurement.

Again, similar to the Chen et al.’s method, this technique only applies for materials that are optically thick, as it relies on the diffusion dipole approximation. Also, the range of measured data used for estimating the dipole parameters is somewhat ill-defined, as data near the source is ignored. Because the light incident within the local area is modulated only by the mesostructure functions, the Tong et al. model essentially assumes that the reflectance profile is flat near the source, rather than increasing hyper-exponentially, as both the dipole and Monte Carlo simulations predict. This tends to give materials a “hard” look when top lit, as the often significant local subsurface scattering contribution is ignored.

Chapter 7

A new model for thin and layered materials

As discussed in Chapter 5, the diffusion dipole is limited to semi-infinite homogeneous materials. This approximation breaks down in the case of thin scattering slabs and multi-layered translucent materials. In this chapter, we remove the semi-infinite restriction and present a new technique for simulating the reflection and transmission of light from arbitrary systems of diffusing layers. We use multiple dipoles to account for light scattering in thin slabs, and extend this model to account for mismatching indices at the top and bottom of the slab, and to handle a rough interface at the top surface. To model multiple layers, we convolve the diffusion profiles of individual layers using an efficient frequency space technique similar to Kubelka-Munk theory. To illustrate the robustness of our approach, we compare results generated by our method to those computed by Monte Carlo simulations with data taken from the optics literature, and show good agreement. We also provide several qualitative examples that demonstrate the diffusion of light in thin slabs and multi-layered materials such as paint, paper, and human skin.

As will be shown in this Chapter, our method generalizes to an arbitrary number of layers, and enables the composition of arbitrary multi-layered materials with different optical parameters for each layer. It is both accurate and efficient and easily integrated into existing implementations that use the dipole diffusion approximation. This Chapter

also shows that the far-source reflectance and transmittance is dominated by inter-layer scattering, which has a potentially large impact when attempting to recover optical parameters from measurements.

7.1 Background

Since the introduction of the diffusion dipole to graphics [62], little work in the computer graphics literature has extended the model significantly. The previous Chapter has outlined several hybrid methods that couple diffusion with various techniques, but the underlying diffusion dipole model has remained unchanged.

As mentioned in Chapter 2, diffusion theory is commonly used in fields other than computer graphics; there is much related work in optics and medical physics. Many organic tissues, such as human skin, internal organs, and plant leaves, are composed of multiple layers [46, 115], which can have a significant impact on both the simulation of reflectance and transmittance and on the recovery of optical parameters [31].

Most previous techniques for deriving reflectance solutions for layered translucent materials use approximate boundary conditions between diffusing layers to give expressions for the fluence rate in both layers [21, 67, 69, 91, 100, 112, 113]. For the boundary between two layers at some depth d , these boundary conditions enforce the continuity of the flux and its gradient across the boundary

$$\phi_1(r) = \eta\phi_2(r), \quad \text{at } z = d, \quad (7.1)$$

$$D_1 \frac{\partial \phi_1(r)}{\partial z} = D_2 \frac{\partial \phi_2(r)}{\partial z}, \quad \text{at } z = d, \quad (7.2)$$

where $\eta = n_1/n_2$ is the ratio of indices of refraction of the layers, and D_1 and D_2 are the diffusion constants of each layer. Schmitt et al. [100] derived Green's functions satisfying these boundary conditions between two turbid layers to determine both the optical properties and steady-state reflectance of human skin. Keijzer et al. [67] has used an approximation for Fresnel reflectance and used these boundary conditions in conjunction with Equation 5.26 to obtain expressions for the fluence rates in a medium consisting of two finite-width layers. An extension to more layers is unclear.

Frequency domain analysis of simple layer configurations has been used by Kielne et al. [68, 69] to find both the steady-state and time-domain reflectance from a semi-infinite medium covered by a thin diffusing slab. Tualle et al. [113] has developed a rapid method for computing the time-domain fluence of a system of two layers, but although Tualle et al. [112] has recently extended Kienle's work to more than two layers, the resulting geometry is still assumed to be semi-infinite. Other time- and frequency-domain approximate solutions for the reflectance and transmittance of a system of layers have also been proposed [3, 9, 79, 80, 95, 118].

None of the above methods are suitable for calculating the steady-state reflectance and transmittance profiles from arbitrary systems of layers, as they still require solving approximations to the boundary conditions above [94]. Many make the additional assumption that the index of refraction of all the layers is constant.

In this Chapter we avoid the complexity of these conditions by determining the reflectance and transmittance profiles of each layer independently, and convolving those profiles to give an accurate approximation of the overall reflectance and transmittance. Previous authors have used convolution techniques to approximate the effects of finite width beams [125], and to obtain the fluence rates from different source distributions [112, 113], but it has not previously been used to combine the profiles of turbid layers. We explicitly assume that diffusion applies in each layer, that is, that the layer is optically thick and has a high albedo.

7.2 Light scattering in thin slabs

The dipole approximation was derived for the case of a semi-infinite medium. It assumes that any light entering the material will either be absorbed or return to the surface. For thin slabs this assumption breaks down as light is transmitted through the slab, which reduces the amount of light diffusing back to the surface. This means that the dipole will overestimate the reflectance of thin slabs, and it cannot correctly predict the transmittance.

We can account for light scattering in slabs by taking the changed boundary condition

into account. For a slab of thickness d , we define a boundary condition for the bottom surface analogous to Equation 5.26. Diffuse light transmitted through the slab does not return, and the upward diffuse radiance is equal to the reflected downward radiance at the bottom surface

$$\int_{\Omega_-} L_d(r, \vec{\omega}) (\vec{n} \cdot \vec{\omega}) d\vec{\omega} = F_{dr} \int_{\Omega_+} L_d(r, \vec{\omega}) (-\vec{n} \cdot \vec{\omega}) d\vec{\omega} \quad \text{at } z = d. \quad (7.3)$$

Simplifying this equation gives a result similar to Equation 5.28,

$$\phi(r) + 2AD \frac{\partial \phi(r)}{\partial z} = 0 \quad \text{at } z = d, \quad (7.4)$$

where we make the assumption that the non-scattering mediums above and below the slab have the same index of refraction. In the next section we will show how to handle the case where the indices differ. In this case of matched boundaries, Equation 7.4 states that the flux vanishes at depth $d + z_b$, which is z_b below the bottom of the slab.

We can approximate Equation 7.4 similar to the top condition as before by mirroring the top dipole about $z = d + z_b$. The net fluence from both dipoles results in zero fluence at $z = d + z_b$ (the lower dotted line in Figure 1b) [86]. Reinforcing the condition at $z = z_b$ (the top dotted line) requires mirroring the bottom dipole about the top line. Both boundary conditions are approximated simultaneously only when there is an infinite array of dipoles [17, 122] (Figure 7.1(b)). When the ratios of indices of refraction, and thus the extrapolation distances, are the same at both the top and bottom interfaces, the z -coordinates of the dipole sources are given by

$$\begin{aligned} z_{r,i} &= 2i(d + 2z_b) + z_{r,0} \\ z_{v,i} &= 2i(d + 2z_b) - z_{r,0} - 2z_b, \quad i = -n, \dots, n, \end{aligned} \quad (7.5)$$

where $2n + 1$ is the number of dipoles, d is the slab thickness, and $z_b = 2AD$ is the extrapolation distance. Each even positive and negative i satisfies the top condition, while each odd i satisfies the bottom. The reflectance due to $2n + 1$ dipoles is the sum of their individual contributions

$$R_d(r) = \sum_{i=-n}^n \frac{\alpha' z_{r,i} (1 + \sigma_{tr} d_{r,i}) e^{-\sigma_{tr} d_{r,i}}}{4\pi d_{r,i}^3} - \frac{\alpha' z_{v,i} (1 + \sigma_{tr} d_{v,i}) e^{-\sigma_{tr} d_{v,i}}}{4\pi d_{v,i}^3}, \quad (7.6)$$

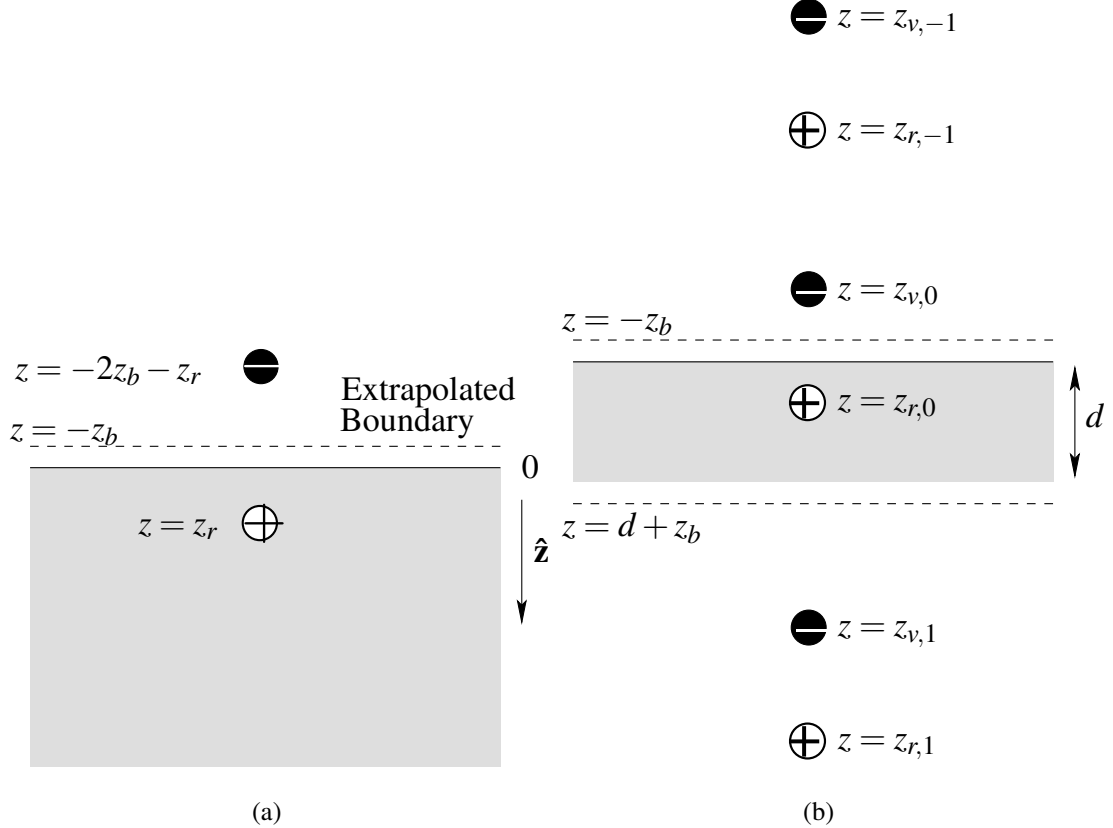


Figure 7.1: Dipole configuration for semi-infinite geometry (left), and the multipole configuration for thin slabs (right).

where $d_{r,i} = \sqrt{r^2 + z_{r,i}^2}$ and $d_{v,i} = \sqrt{r^2 + z_{v,i}^2}$ are the distances to the dipole sources from a given point on the surface of the object. Note that when $n = 0$, Equation 7.6 simplifies to Equation 5.35. Adjusting for the depth of the slab gives the diffuse transmittance

$$T_d(r) = \sum_{i=-n}^n \frac{\alpha'(d - z_{r,i})(1 + \sigma_{tr}d_{r,i})e^{-\sigma_{tr}d_{r,i}}}{4\pi d_{r,i}^3} - \frac{\alpha'(d - z_{v,i})(1 + \sigma_{tr}d_{v,i})e^{-\sigma_{tr}d_{v,i}}}{4\pi d_{v,i}^3}. \quad (7.7)$$

This multipole approximation is used in the same way as the dipole. An incident ray of light is converted into an isotropic point source embedded at depth $z_{r,0}$ in the slab, and the diffuse reflectance and transmittance are given by Equations 7.6 and 7.7. In practice, since the contribution of each dipole decreases quickly with distance, the actual number required in this multipole configuration depends on the slab thickness and the optical properties of the material. Wang [122] has shown that these expressions compare well

to Monte Carlo simulations in situations where diffusion theory is applicable, i.e. when $\sigma'_s \gg \sigma_a$ and the slab is at least a few mean free paths thick.

Figures 7.2–7.5 compare the Monte Carlo traced reflectance and transmittance of thin slabs from 2 to 20 mean free paths to the responses predicted by the dipole and multipole methods. The dipole transmittance is calculated using the linear distance from the incident light to exitant location (i.e. assuming the points are on the same surface). Note that because the dipole does not account for light that exits the bottom of the slab, it predicts light will continue to scatter and exit the top of the material. For thicker slabs, the dipole performs well, but is noticeably divergent for thin slabs. The dipole also incorrectly predicts both the intensity and shape of the transmittance profiles in all cases. The multipole accurately predicts both the reflectance and transmittance in all cases. This is also evident in the total reflectance and transmittance predicted by the two models, shown in Table 7.1.

Table 7.1: Comparison of the total reflectance and transmission predicted by the dipole and multipole models compared to Monte Carlo for the plots in Figures 7.2–7.5.

Mfp	Total Reflectance			Total Transmittance		
	MC	Multipole	Dipole	MC	Multipole	Dipole
2	51.6%	49.8%	90.2%	49.8%	48.1%	26.5%
10	83.4%	83.8%	90.2%	13.8%	13.8%	3.0%
20	89.0%	89.0%	90.2%	6.0%	5.9%	0.7%

7.3 Multiple layers

The multipole approximation has been used to compute reflectance and transmittance from slabs in the space and time domains [17, 122], but only when the non-scattering materials above and below the slab are assumed to have the same index of refraction. When dealing with multi-layered materials, however, this is often not the case. Many materials (e.g. skin, plant leaves), are composed of layers with differing indices of refraction.

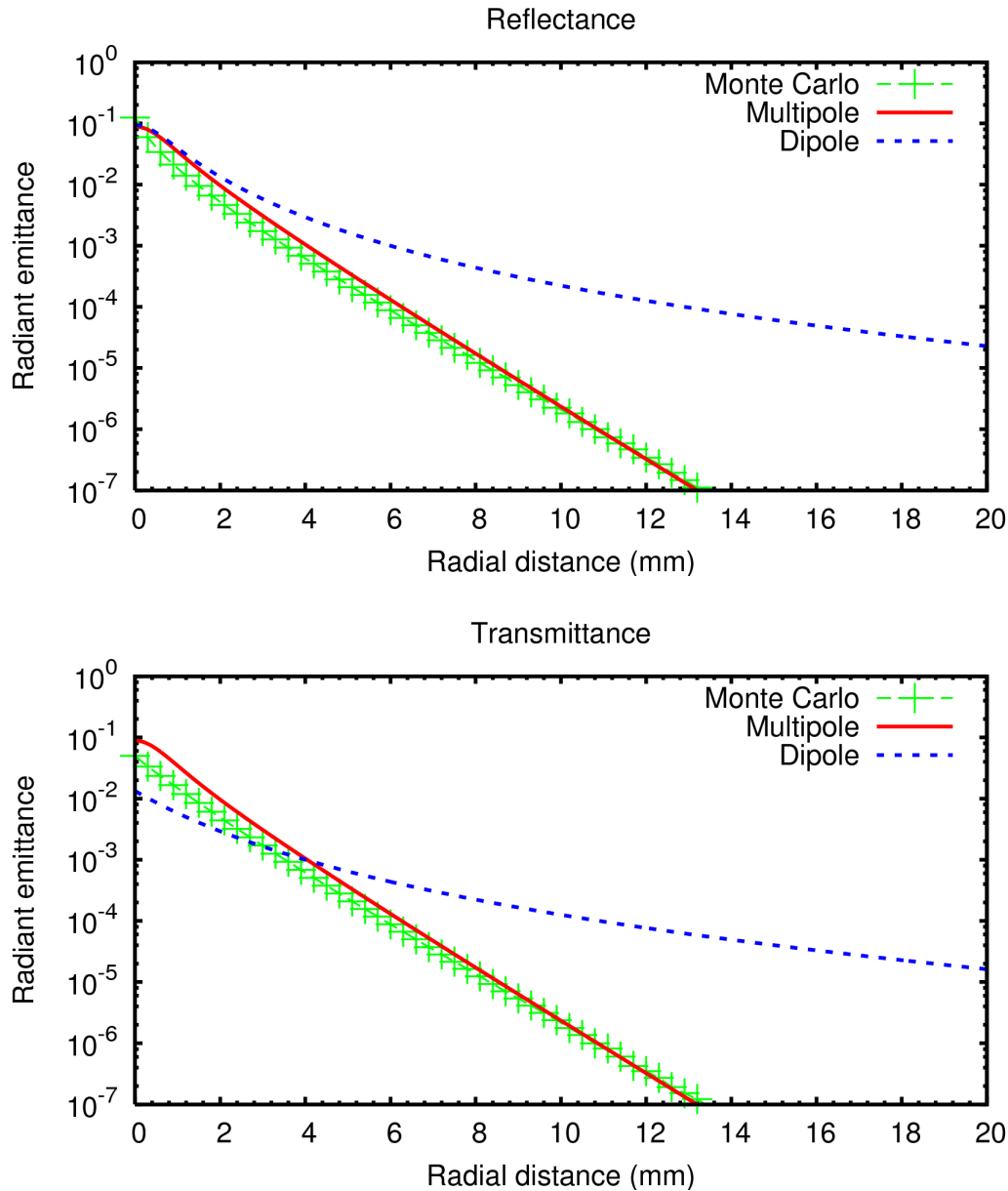


Figure 7.2: Comparison of the reflectance and transmission profiles of slabs of varying thickness predicted by the dipole and the multipole to Monte Carlo simulations. The slab thickness is 2 mean free paths, and the mean free path length is 1mm.

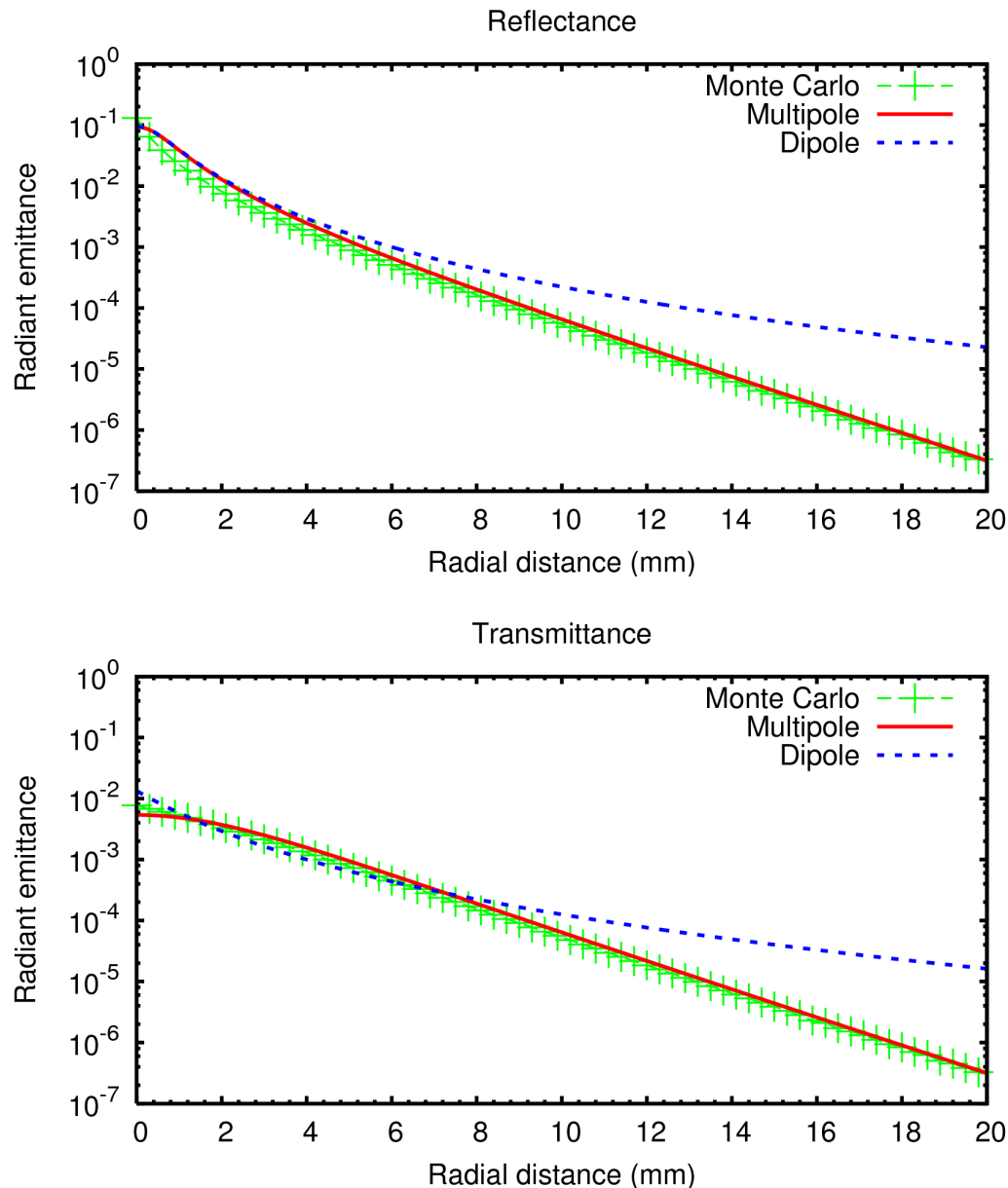


Figure 7.3: Comparison of the reflectance and transmission profiles of slabs of varying thickness predicted by the dipole and the multipole to Monte Carlo simulations. The slab thickness is 5 mean free paths, and the mean free path length is 1mm.

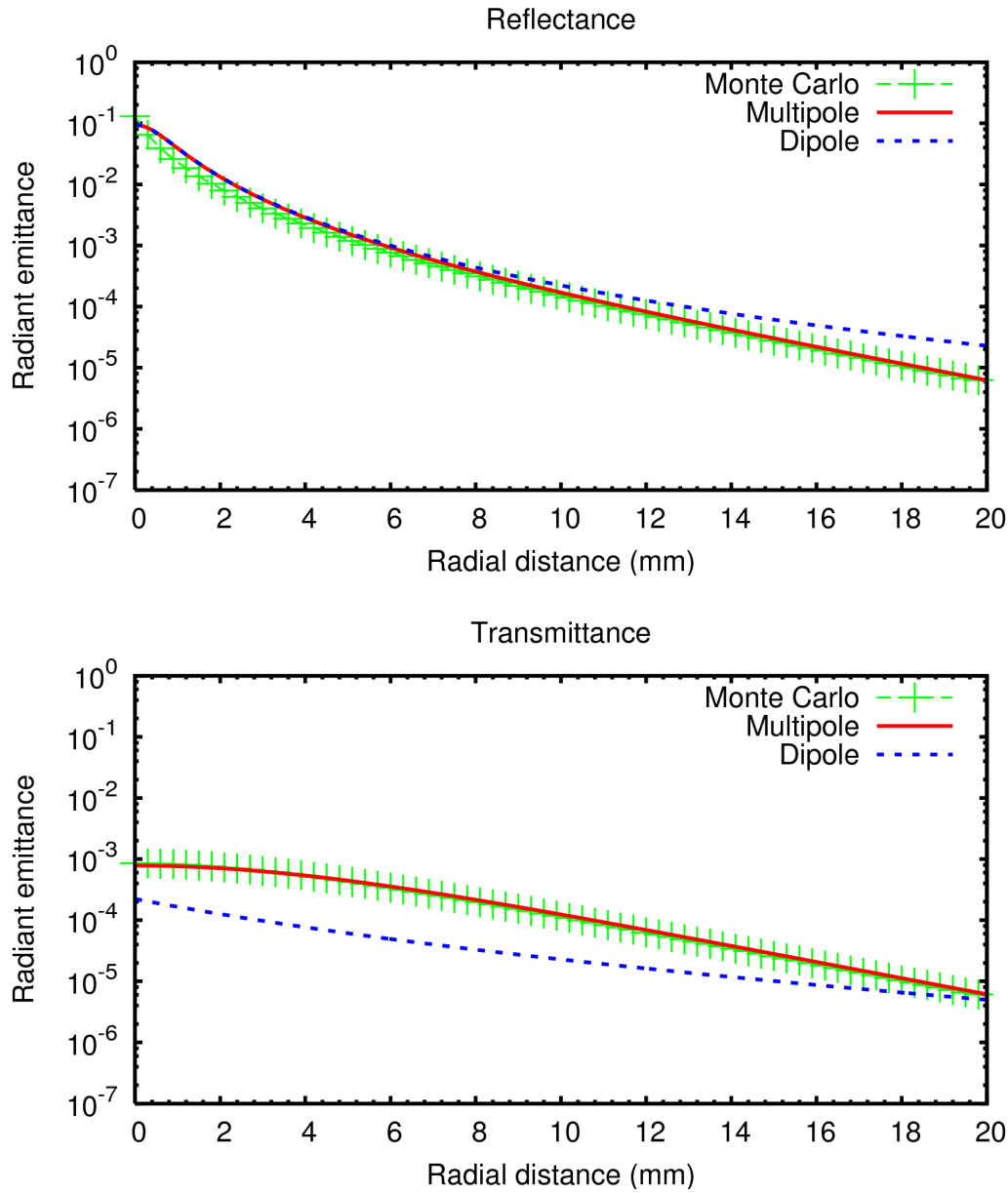


Figure 7.4: Comparison of the reflectance and transmission profiles of slabs of varying thickness predicted by the dipole and the multipole to Monte Carlo simulations. The slab thickness is 10 mean free paths, and the mean free path length is 1mm.

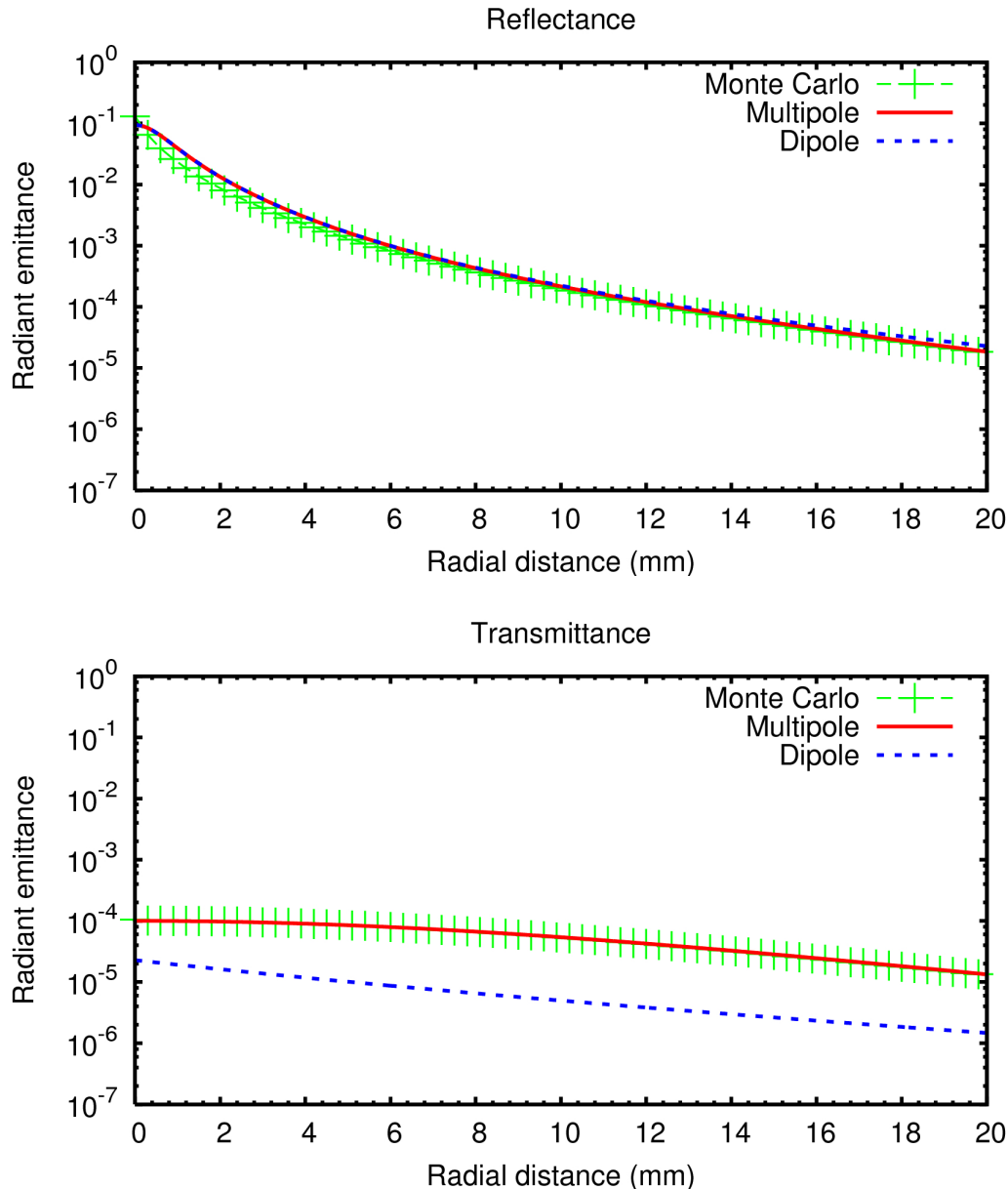


Figure 7.5: Comparison of the reflectance and transmission profiles of slabs of varying thickness predicted by the dipole and the multipole to Monte Carlo simulations. The slab thickness is 20 mean free paths, and the mean free path length is 1mm.

To account for mismatched indices, most recent work involves solving difficult boundary conditions or their approximations at the interface between diffusing layers [30, 94]. This gives expressions for the fluence rate in both layers, and can be used to determine the reflectance [21, 67, 69, 80, 91, 100, 112, 113]. As discussed at the start of this Chapter, this results in complex expressions that can be expensive to evaluate, and in models that have no clear extension to arbitrary systems of layers. Most models also make the further assumption that the final layer is still semi-infinite. In addition, these models do not directly provide the steady-state space-resolved reflectance and transmittance profiles.

To model the effects of Fresnel reflectance between mismatched layers, we extend the boundary conditions from the single slab case. We will deal with light that transmits across boundaries between layers in the following section.

When the index of refraction ratios η_{top} and η_{bottom} at the two interfaces of the slab are mismatched, the different Fresnel reflectances give rise to different EBCs at the top and bottom of the slab

$$\phi(r) - 2A_{\text{top}}D \frac{\partial \phi(r)}{\partial z} = 0, \quad \text{at } z=0, \quad (7.8)$$

$$\phi(r) + 2A_{\text{bottom}}D \frac{\partial \phi(r)}{\partial z} = 0, \quad \text{at } z=d, \quad (7.9)$$

where A_{top} and A_{bottom} are calculated using the appropriate relative index of refraction

$$A_{\text{top}} = \frac{1 + r_s(\eta_{\text{top}})}{1 - r_s(\eta_{\text{top}})}, \quad A_{\text{bottom}} = \frac{1 + r_s(\eta_{\text{bottom}})}{1 - r_s(\eta_{\text{bottom}})}$$

These two conditions give different extrapolated boundaries where the fluence is forced to zero. We can approximately satisfy both conditions simultaneously by mirroring about the distance from the top extrapolated boundary to the bottom extrapolated boundary (see Figure 7.6)

$$\begin{aligned} z_{p,i} &= 2i(d + z_{b,\text{top}} + z_{b,\text{bottom}}) + z_{r,0} \\ z_{n,i} &= 2i(d + z_{b,\text{top}} + z_{b,\text{bottom}}) - z_{r,0} - 2z_{b,\text{top}}, \end{aligned} \quad (7.10)$$

where each z_b is computed using the appropriate A . When the Fresnel reflectances at the top and bottom are the same, $A_{\text{top}} = A_{\text{bottom}}$, and the formulas in Equation 7.10 reduce to those in Equation 7.5.

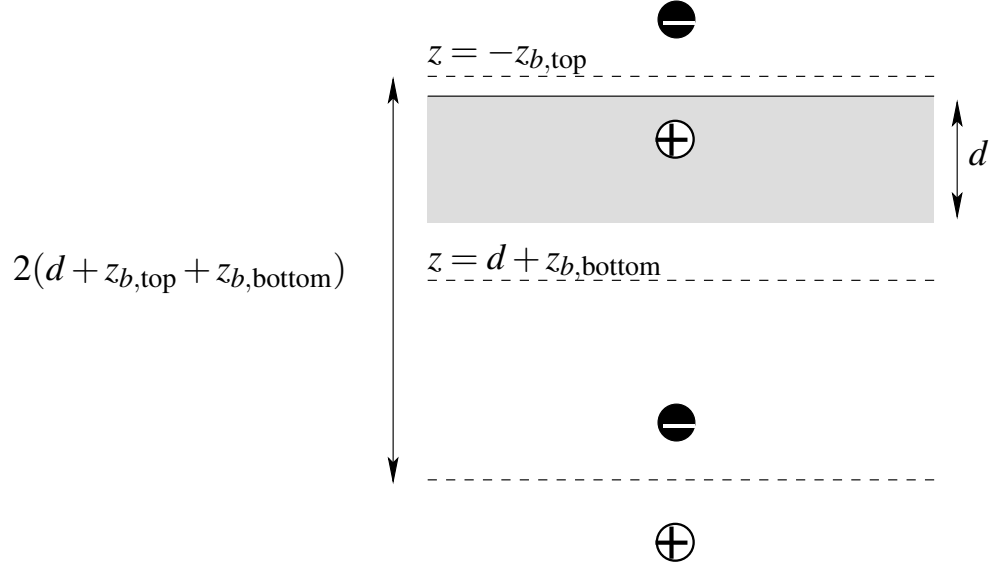


Figure 7.6: The mirroring distance of the multipole is changed in the case of mismatched indices. donnerF2.pdf.

7.4 Inter-layer scattering

Calculating the reflectance and transmittance profiles of a multi-layered scattering material requires modeling the light that scatters between layers. To account for this inter-layer scattering, we convolve the profiles of adjacent layers together, and apply reasoning similar to Kubelka-Munk theory to correct for more complex light transport.

Similar to the Hanrahan-Krueger BRDF model, Kubelka-Munk theory uses 1D radiative transport to describe light propagation through turbid materials [75]. It is extended to multiple turbid layers by multiplying the reflectance and transmittance of adjacent layers together [74]. Instead of 1D scalar values for reflectance and transmittance, we compute 3D diffusion profiles, and use convolution instead of multiplication. In the following we derive simple expressions for the total reflectance and transmittance of systems of layers, while avoiding the difficult boundary conditions between layers.

As an example, consider the problem of finding the transmittance profile of a system of two layers of finite-thickness. If diffusion theory is applicable to both layers ($\sigma'_s \gg \sigma_a$ and the slab is at least a few mean free paths thick), it is reasonably accurate to assume that

all interactions between the layers are due to multiple scattering. This removes the need to model light scattering across more than one layer at a time. Since the method of the previous section deals with the effects of internal reflectance in the case of mismatched indices, a base transmittance profile of both layers that includes the effects of internal diffuse reflection is found by convolving the profiles of the individual layers. That is, given the incident flux $\Phi(x, y, \vec{\omega})$ at a surface, we compute the radiant emittance profile, M , through the slab at (x, y) by convolving the incident flux, Φ , with the transmittance profile, T

$$M(r) = \int_{-\infty}^{\infty} \int_{-\infty}^{\infty} \Phi(x', y', \vec{\omega}) T(r'') dx' dy' = \Phi(x, y, \vec{\omega}) * T(r), \quad (7.11)$$

where $r'' = \sqrt{(x - x')^2 + (y - y')^2}$ and $*$ is the convolution operator.

Both the dipole and multipole methods assume that the emitted light is diffuse. They also assume that the angle of incidence has no effect on the reflection or transmission response of a material. This effectively equates the impulse response of a slab to its diffuse response. Note that the multipole gives the impulse response of a slab.

We can combine the profiles of two different layers by assuming that all interactions between the two layers are due to multiple scattering. This assumption is reasonably accurate as long as diffusion theory is applicable to the individual layers — i.e. they have a thickness of at least a few mean free paths. Based on this assumption, we can compute the profile T_{12} of the light transmitted through two slabs with transmittance profiles T_1 and T_2 by convolving the profiles

$$T_{12}(r) = \int_{-\infty}^{\infty} \int_{-\infty}^{\infty} T_1(r') T_2(r'') dx' dy' = T_1(r) * T_2(r), \quad (7.12)$$

where $r' = \sqrt{x'^2 + y'^2}$.

The above expression implies, however, that none of the light transmitted into the second layer returns to the first, which does not consider the full range of interactions between the layers. Since $T_1(r)$ light reaches top of the second layer, $T_1(r) * R_2(r)$ light will be scattered back. Of that, $T_1(r) * R_2(r) * R_1(r)$ will be scattered back into the second layer, and $T_1(r) * R_2(r) * R_1(r) * T_2(r)$ will be transmitted out the bottom of the slab (see Figure 7.7). This contribution can be important, particularly when calculating the total

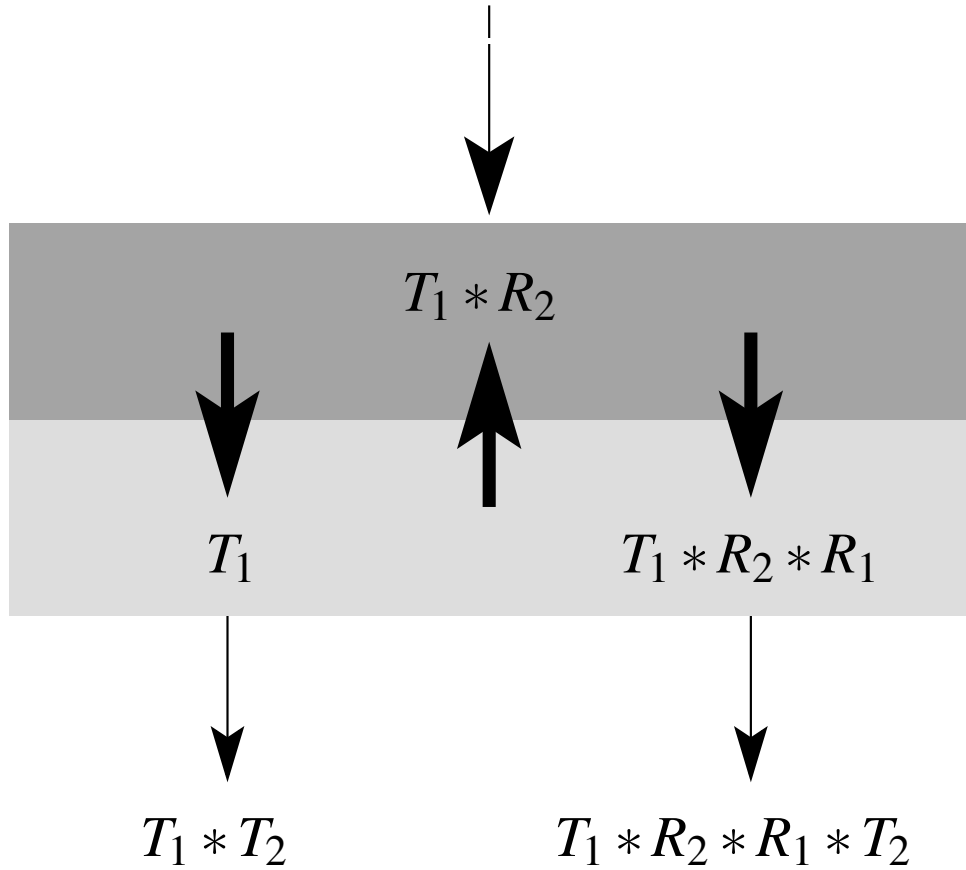


Figure 7.7: The first two modes of the inter-scattering of light between two turbid layers.

diffuse reflectance and transmittance. To account for such additional scattering events across the interface between layers we correct Equation 7.12 with additional terms for each possible scattering mode

$$T_{12} = T_1 * T_2 + T_1 * R_2 * R_1 * T_2 + T_1 * R_2 * R_1 * R_2 * R_1 * T_2 + \dots \quad (7.13)$$

where we have omitted the dependence on r for brevity. This series of convolutions is evaluated efficiently using Fourier theory, which changes each convolution into point-wise products in frequency space

$$\begin{aligned} \mathcal{T}_{12} &= \mathcal{T}_1 \mathcal{T}_2 + \mathcal{T}_1 \mathcal{R}_2 \mathcal{R}_1 \mathcal{T}_2 + \mathcal{T}_1 \mathcal{R}_2 \mathcal{R}_1 \mathcal{R}_2 \mathcal{R}_1 \mathcal{T}_2 + \dots \\ &= \mathcal{T}_1 \mathcal{T}_2 (1 + \mathcal{R}_2 \mathcal{R}_1 + (\mathcal{R}_2 \mathcal{R}_1)^2 + (\mathcal{R}_2 \mathcal{R}_1)^3 + \dots), \end{aligned} \quad (7.14)$$

where \mathcal{R} and \mathcal{T} are Fourier-transformed diffuse reflectance and transmittance profiles. The resulting expression is a geometric series of point-wise products. As $\mathcal{R}_1\mathcal{R}_2 < 1$, Equation 7.14 simplifies to

$$\mathcal{T}_{12} = \frac{\mathcal{T}_1\mathcal{T}_2}{1 - \mathcal{R}_2\mathcal{R}_1}. \quad (7.15)$$

A similar analysis to above produces a similar formula for the reflectance of two layers

$$\mathcal{R}_{12} = \mathcal{R}_1 + \frac{\mathcal{T}_1\mathcal{R}_2\mathcal{T}_1}{1 - \mathcal{R}_2\mathcal{R}_1}. \quad (7.16)$$

This method extends to more than two layers by recursive substitution of Equations 7.15 and 7.16 in for \mathcal{R}_1 or \mathcal{T}_1 , and re-evaluating the formulas. The real-space reflectance and transmittance profiles of a many-layered material are computed by computing the inverse Fourier transform of the overall frequency profiles. The real-space profiles are then used with Equation 5.36 to find the total diffuse reflectance and transmittance. In practice, since the profiles are by definition radially symmetric, we use the discrete Hankel transform to efficiently convolve the profiles.

Note that Equations 7.15 and 7.16 are identical to Kubelka's [74], but applied in frequency space. They can also be considered as an application of the multipole approximation as a scattering function in operator form [89].

7.4.1 Accuracy of the multipole and convolution method

In this subsection we compare results computed using the method outlined in the proceeding sections to Monte Carlo simulations of steady-state reflectance and transmittance, using previously published data. The Monte Carlo simulations were performed similar to existing standard methods [124], though using in-house code. The individual layer profiles were calculated using Equations 7.6 and 7.7, taking into account any mismatch in the indices as described above. Since there is no analytical Fourier transform of Equations 7.6 and 7.7, we exploited the radial symmetry of the problem and used a discrete zero-order Hankel transform to convolve the responses [10]. Although the Hankel transform was faster than a full 2D Fourier transform over the surface, it produced noisy results when insufficient samples were used. Relative errors were calculated as the difference between Monte Carlo and convolution divided by Monte Carlo [122]. To

ensure accuracy even far from the source, Monte Carlo simulations were performed using 10 million photon packets, and took on average several hours to complete on a workstation. The convolution calculations required only a few seconds to compute.

Kienle et al. has previously investigated the steady-state reflectance of a two-layered turbid slabs [69]. In their experiments they employed a semi-infinite slab covered by a thin layer. Figures 7.8 and 7.10 reproduce the experiments recorded in Kienle et al. [69] Figures 3 and 4, where we compare Monte Carlo simulations to convolved reflectance, with and without the Kubelka-Munk correction described in the previous section. Five dipole pairs were used in the multipole, with 5000 radial samples when performing the convolution. The plots show good agreement for varying scattering and absorption, and for different thicknesses of the top layer. Note that the uncorrected and corrected convolution diverge at approximately 5mm, where the influence of inter-layer scattering becomes significant. Figures 7.9 and 7.11 show the relative error of the uncorrected and corrected convolution compared to Monte Carlo. Note that the Kubelka-Munk correction significantly decreases the error in the convolution, particularly far from the source.

Figure 7.12 shows the steady-state reflectance from a four-layered turbid model. The model parameters are taken from Eda and Okada [27], who used a Monte Carlo model to predict the steady-state reflectance of a human neonatal brain. These parameters are summarized in the figure caption. Although the index of refraction was not reported, we assumed a constant index of 1.4, a common value for human tissue. Although the reference describes a five-layer model, we discarded the internal low-scattering layer, which was thin and transparent enough to not contribute significantly to the results. In the plot, five dipole pairs were used in the multipole, and 5000 radial samples for the convolutions. The addition of the Kubelka-Munk correction terms again improves the accuracy of the convolution, suggesting that inter-layer scattering significantly affects the overall reflectance of turbid layered materials, even those with matching boundaries. This is seen when looking at the relative error in Figure 7.12 (bottom); inter-layer scattering is the dominant mode far from the source.

In Figures 7.13 and 7.14, the steady-state reflectance and transmittance of a two-layered slab are shown. The parameters used are $\sigma'_{s1} = 1.0\text{mm}^{-1}$, $\sigma'_{s2} = 4.0\text{mm}^{-1}$, $\sigma'_{a1} = 0.005\text{mm}^{-1}$, $\sigma'_{a2} = 0.001\text{mm}^{-1}$, $d_1 = 5\text{mm}$, $d_2 = 1\text{mm}$, $n_1 = 1.1$, and $n_2 = 1.4$.

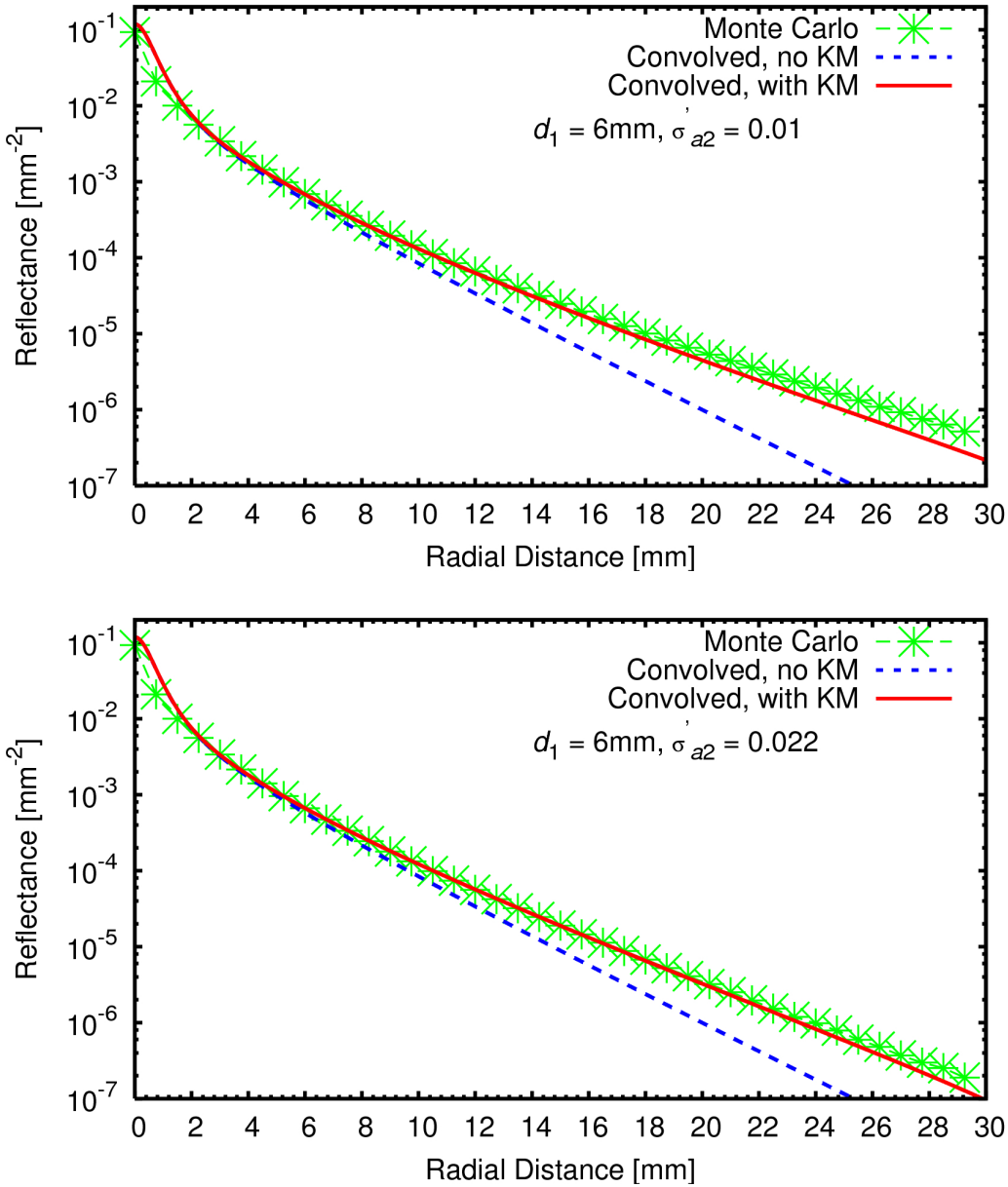


Figure 7.8: Comparison of the convolved multipole with Monte Carlo simulation using parameters from Kienle [69], Figure 3. The parameters are $\sigma'_{s1} = 1.3 \text{ mm}^{-1}$, $\sigma'_{s2} = 1.0 \text{ mm}^{-1}$, $\sigma'_{a1} = 0.005 \text{ mm}^{-1}$, and (top) $\sigma'_{a2} = 0.01 \text{ mm}^{-1}$ or (bottom) $\sigma'_{a2} = 0.022 \text{ mm}^{-1}$. The thickness of the top layer is $d_1 = 6 \text{ mm}$, $d_2 = \infty \text{ mm}$, and $n_1 = n_2 = 1.4$.

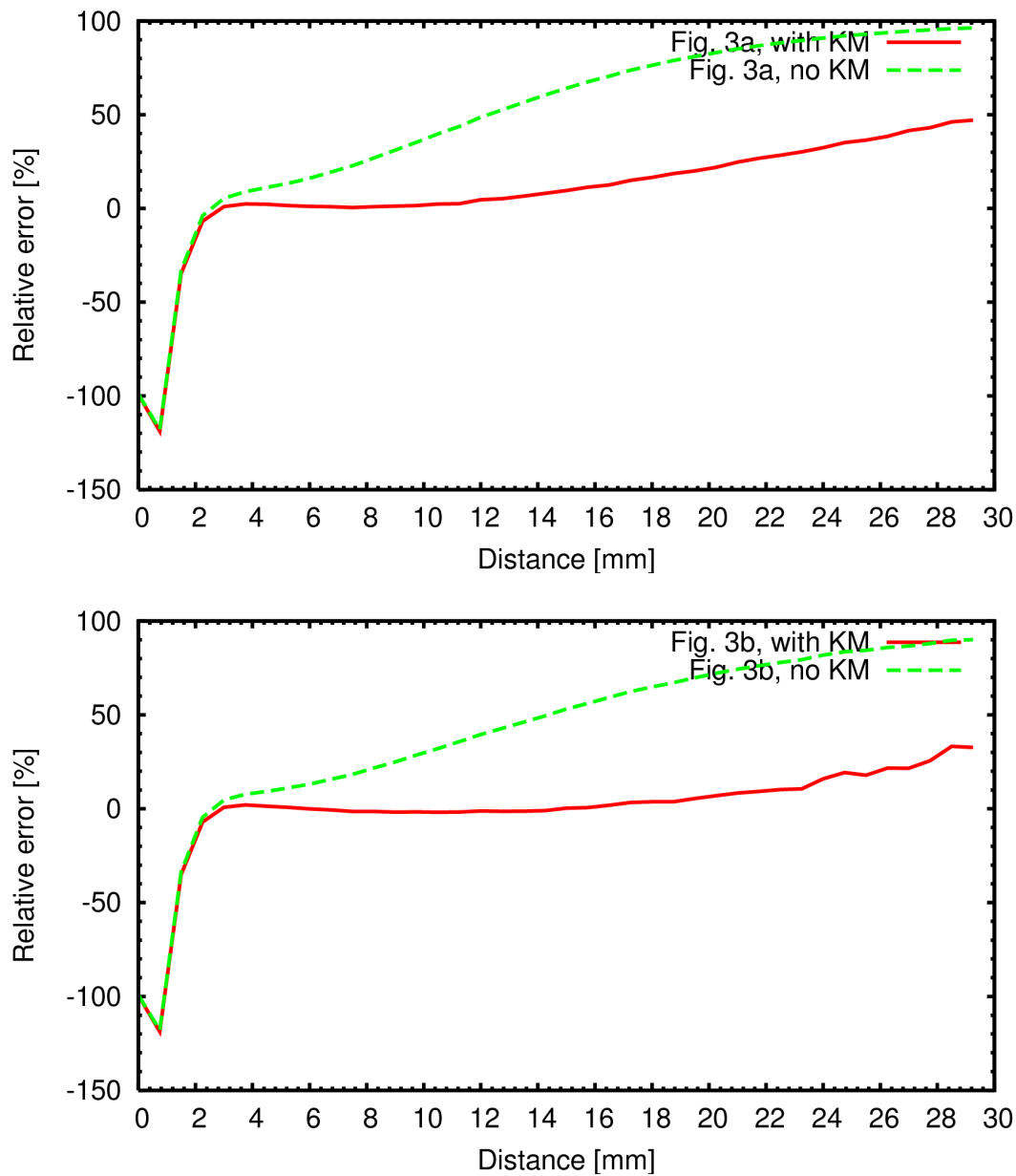


Figure 7.9: Relative error of Figures 7.8 (top) and 7.8 (bottom).

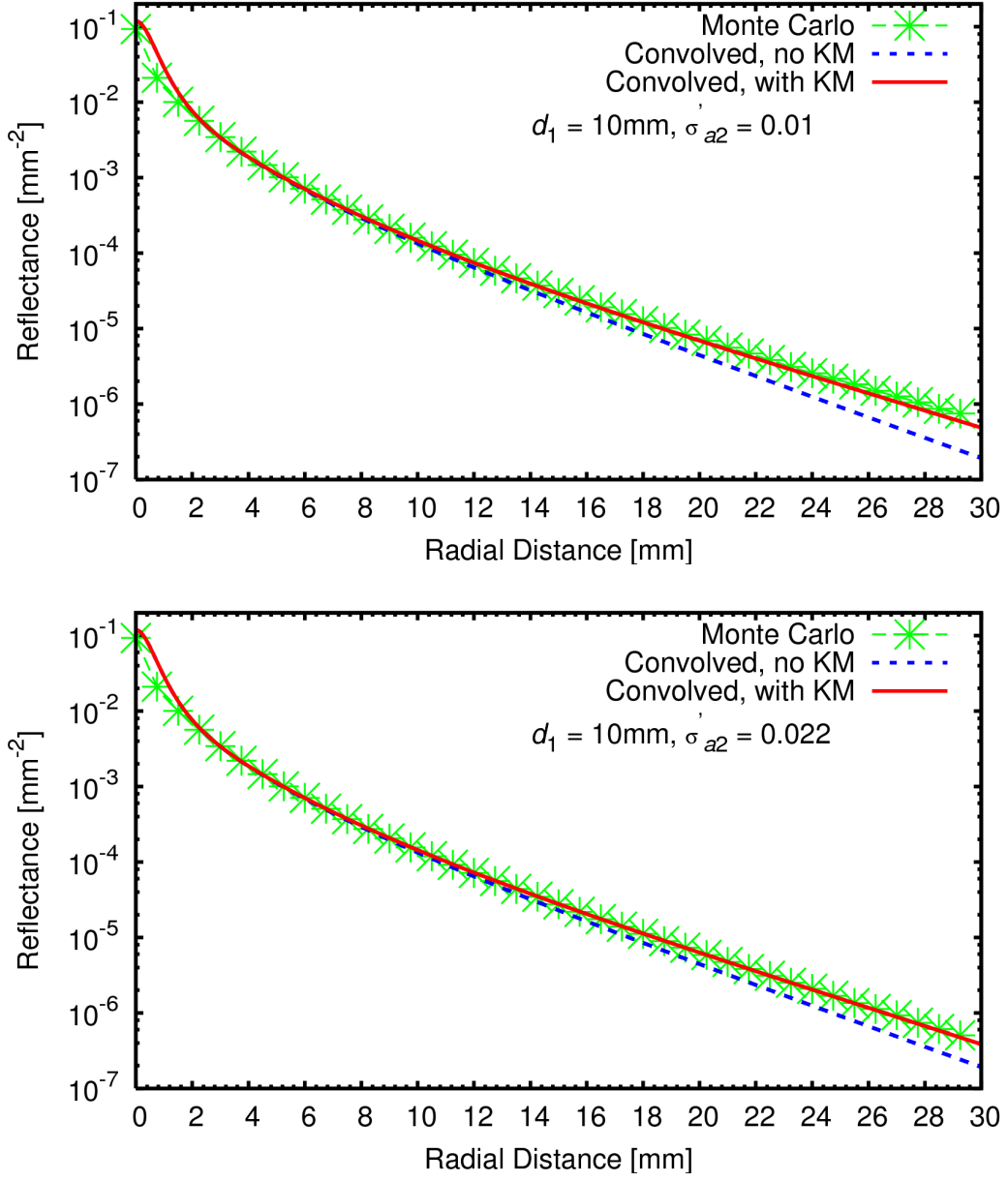


Figure 7.10: Comparison of the convolved multipole with Monte Carlo simulation using parameters from Kienle [69], Figure 4. The parameters of the right plot are $\sigma'_{s1} = 1.3\text{mm}^{-1}$, $\sigma'_{s2} = 1.0\text{mm}^{-1}$, $\sigma'_{a1} = 0.005\text{mm}^{-1}$, and (top) $\sigma'_{a2} = 0.01\text{mm}^{-1}$ or (bottom) $\sigma'_{a2} = 0.022\text{mm}^{-1}$. The thickness of the top layer is $d_1 = 10\text{mm}$, $d_2 = \infty\text{mm}$, and $n_1 = n_2 = 1.4$.

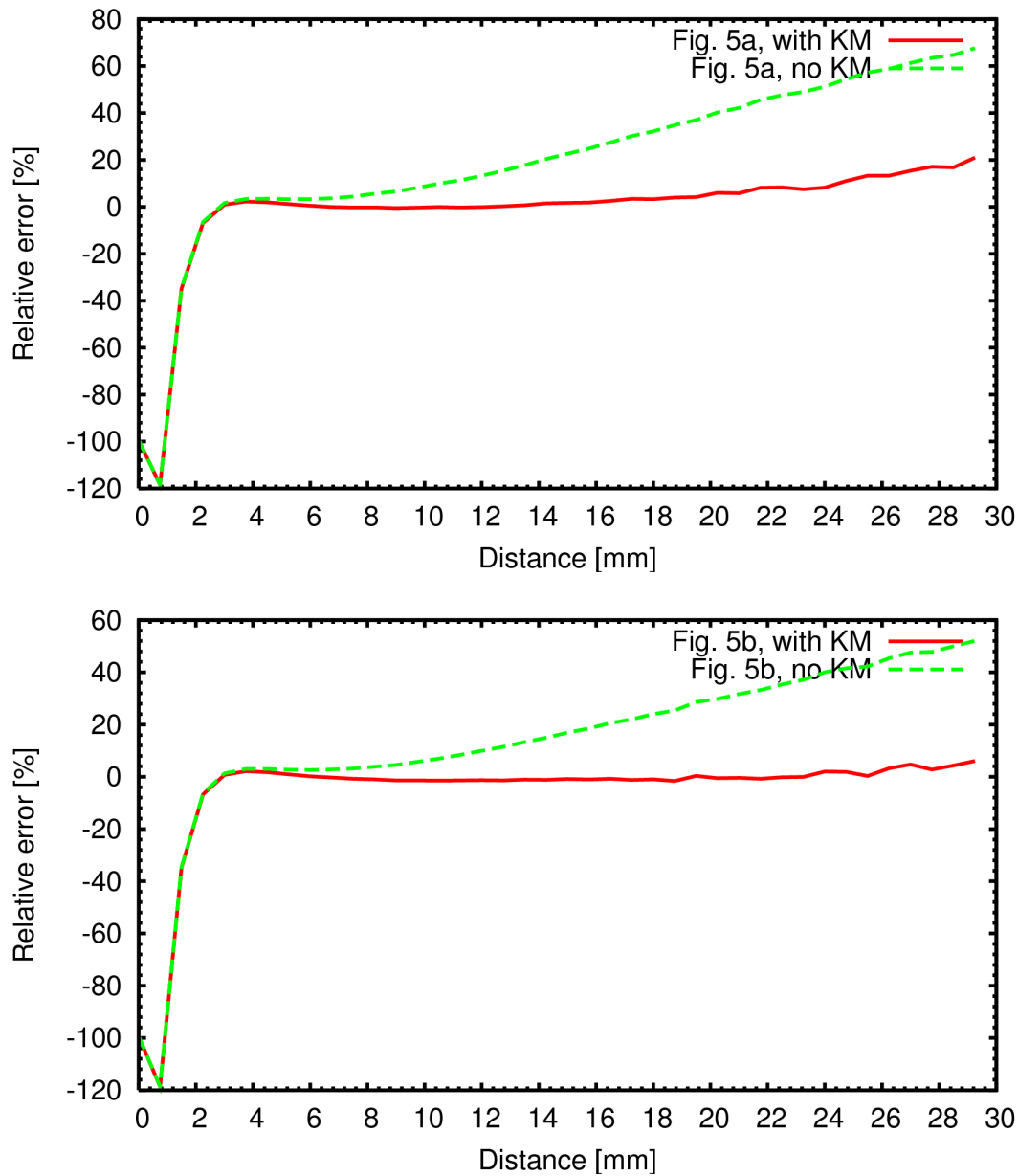


Figure 7.11: Relative error of Figures 7.10 (top) and 7.10 (bottom).

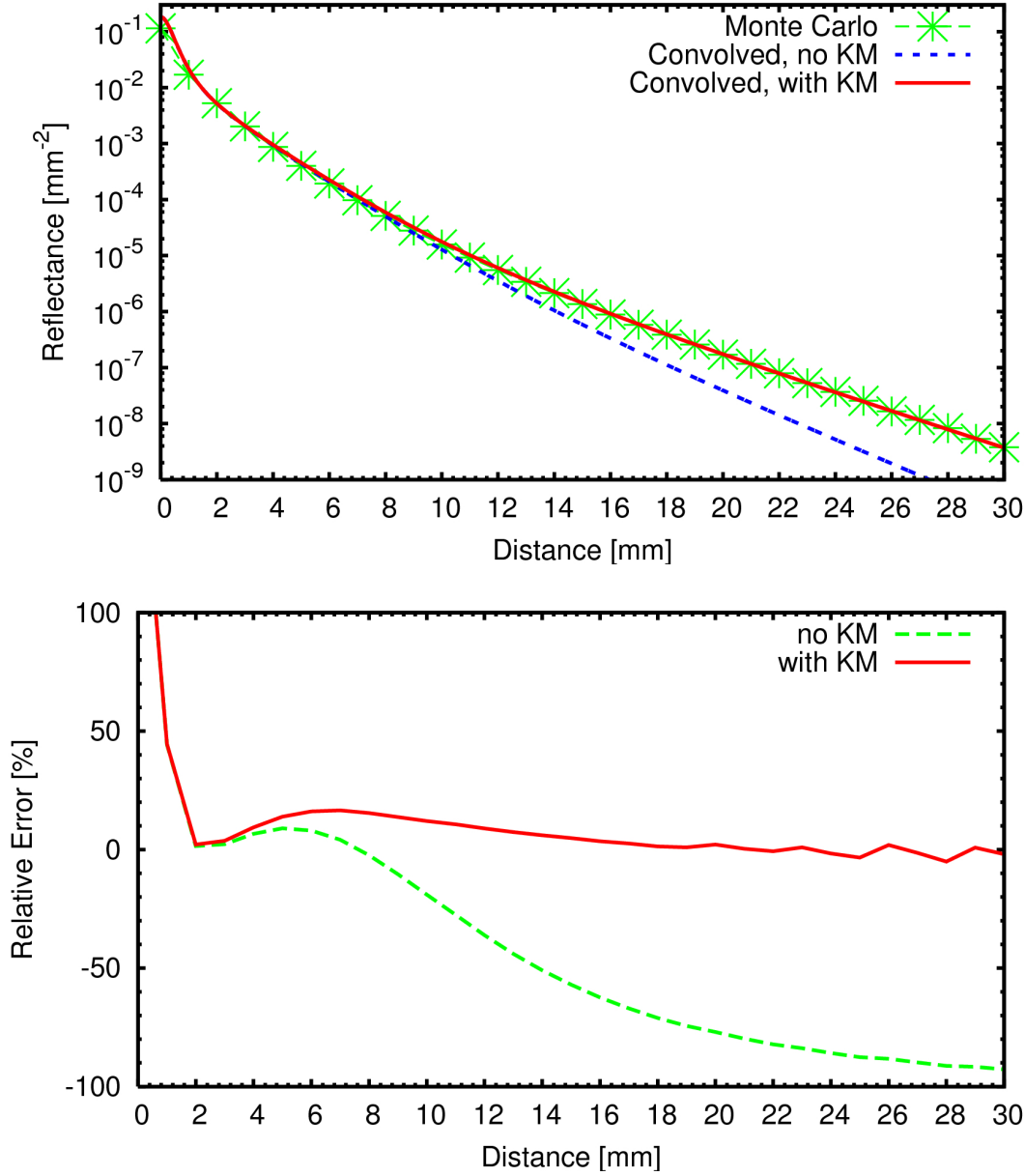


Figure 7.12: (top) Comparison of the convolved multipole with Monte Carlo simulation using parameters from Eda and Okada [27]. The parameters are $\sigma'_{s1} = 1.882 \text{ mm}^{-1}$, $\sigma'_{s2} = 1.584 \text{ mm}^{-1}$, $\sigma'_{s3} = 0.452 \text{ mm}^{-1}$, $\sigma'_{s4} = 0.963 \text{ mm}^{-1}$, $\sigma'_{a1} = 0.018 \text{ mm}^{-1}$, $\sigma'_{a2} = 0.016 \text{ mm}^{-1}$, $\sigma'_{a3} = 0.048 \text{ mm}^{-1}$, $\sigma'_{a2} = 0.037 \text{ mm}^{-1}$, $d_1 = d_2 = 2 \text{ mm}$, $d_3 = 3 \text{ mm}$, $d_4 = \infty$, $n_1 = n_2 = n_3 = n_4 = 1.4$. (bottom) Relative error with and without Kubelka-Munk correction to the convolution.

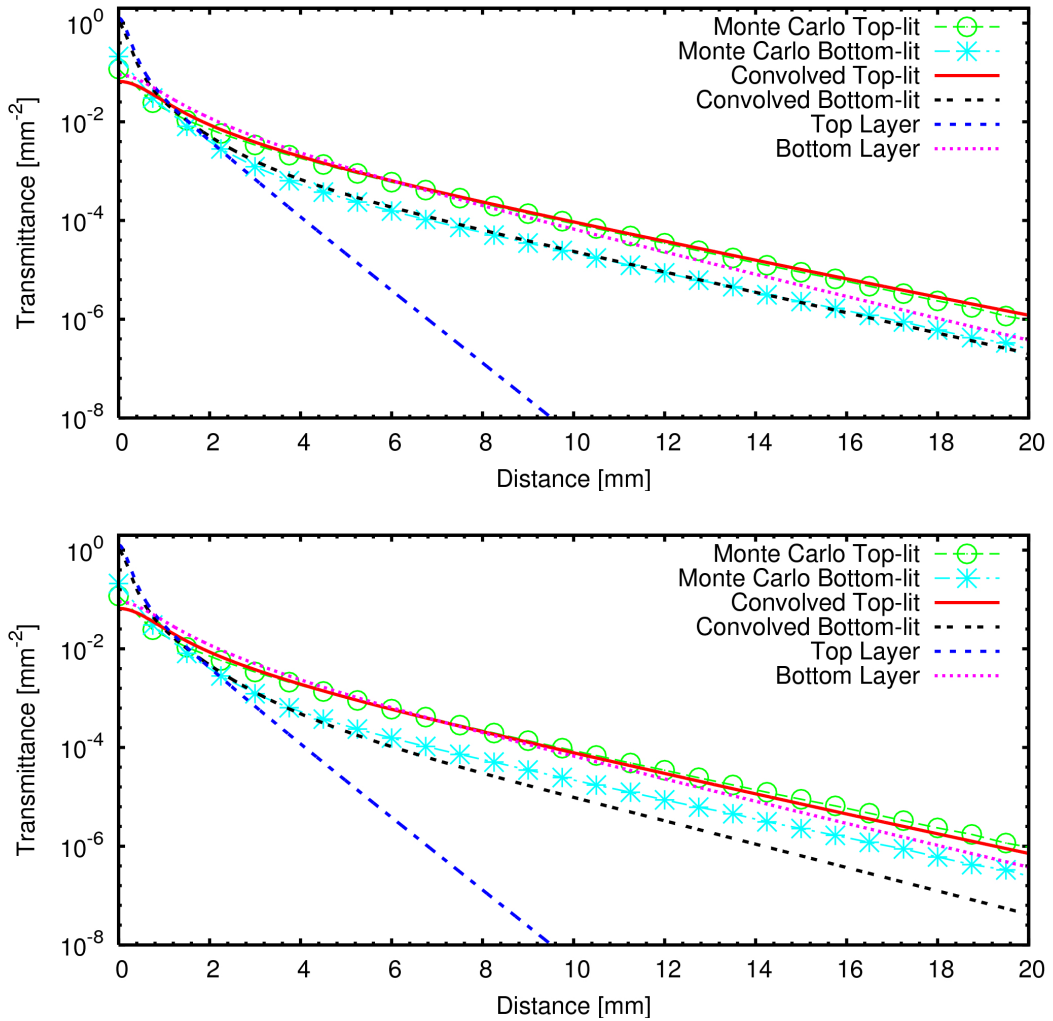


Figure 7.13: Reflectance of a two-layered material with (top), and without (bottom) Kubelka-Munk correction. The circles and long dashed lines are when the material is lit from above, while the crosses and solid lines are when the material is lit from below. The properties of the layers are $\sigma'_{s1} = 1.0 \text{ mm}^{-1}$, $\sigma'_{s2} = 4.0 \text{ mm}^{-1}$, $\sigma'_{a1} = 0.005 \text{ mm}^{-1}$, $\sigma'_{a2} = 0.001 \text{ mm}^{-1}$, $d_1 = 5 \text{ mm}$, $d_2 = 1 \text{ mm}$, $n_1 = 1.1$, and $n_2 = 1.4$. The order of parameters is reversed to calculate the bottom-lit case. The short dashed lines show the reflectances of the top and bottom layers individually.

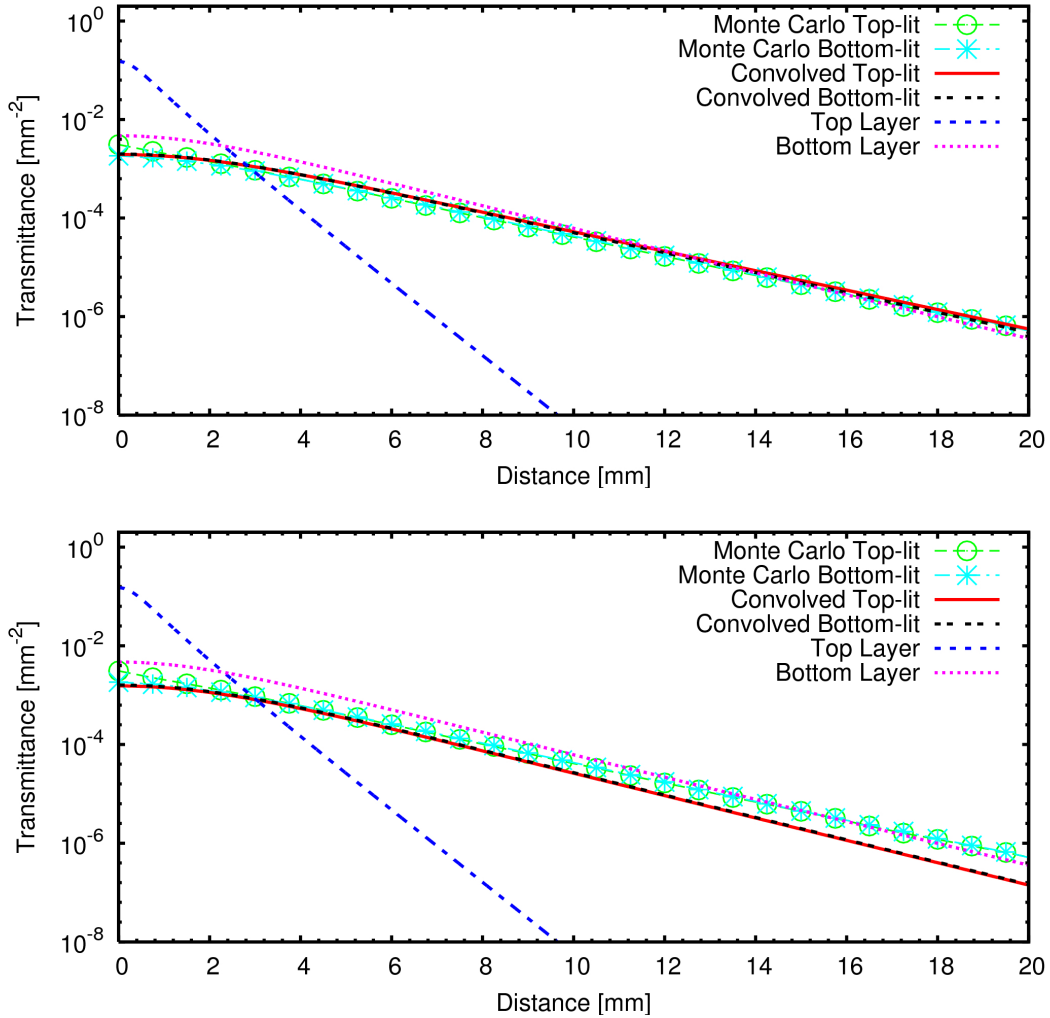


Figure 7.14: Transmittance of a two-layered material with (top), and without (bottom) Kubelka-Munk correction. The circles and dashed lines are when the material is lit from above, while the crosses and solid lines are when the material is lit from below. The parameters of the layers are given in Fig. 7.13. The total diffuse transmittance in the top-lit case is 8.8% without, and 13.0% with Kubelka-Munk correction, compared to 13.1% as calculated by Monte Carlo. In the bottom lit-case, the total diffuse transmittance is 9.1% without, and 12.9% with Kubelka-Munk correction, compared to 12.3% as calculated by Monte Carlo. The short dashed lines show the transmittances of the top and bottom layers individually.

Five dipole pairs were used in the multipole, with 5000 radial samples for the convolutions. The left half of each figure shows the uncorrected convolution, while the right half adds the effects of inter-layer scattering. Both figures also show the reflectance or transmittance of the individual layers, to illustrate that it is the interaction of light between the layers captured by the convolution methods that gives the correct response.

In particular, Figure 7.14 suggests that a significant amount of transmitted light is due to inter-layer scattering. This is also shown when calculating the total diffuse transmittance using numerical integration of Equation 5.36. Compared to a Monte Carlo reference of 13.1% for the top-lit case, the uncorrected convolution gave 8.8% for total diffuse transmittance, while adding the effects of multiple scattering increased the total diffuse transmittance to 13.0%. For the bottom-lit case, adding the effects of multiple scattering using the Kubelka-Munk correction terms increased the calculated total diffuse transmittance from 9.1% to 12.9%, compared to a 12.3% reference. Note also that the convolution captures the non-polarity of transmitted light, while the reflectance profiles differ significantly. This bi-coloration is an important characteristic of many thin layered turbid materials, such as plant leaves [46].

7.5 Rough surfaces

This Chapter has so far assumed that the top surface of the material is smooth. We can account for rough surfaces by modifying the boundary condition that states how the diffused light is reflected at the surface. This can be done by replacing the Fresnel term in Equation 5.26 by an appropriate BRDF. In the following, we will assume that a microfacet model can be used to describe the roughness of the surface, and we model the surface reflection using a Torrance-Sparrow BRDF [109]

$$f_r(\vec{x}, \vec{\omega}_o, \vec{\omega}_i) = \frac{F(\vec{x}, \vec{\omega}_o, \vec{\omega}_i)D(\vec{x}, \vec{\omega}_o, \vec{\omega}_i, \sigma)G(\vec{x}, \vec{\omega}_o, \vec{\omega}_i)}{4(\vec{\omega}_i \cdot \vec{n})(\vec{\omega}_o \cdot \vec{n})}, \quad (7.17)$$

where \vec{n} is the surface normal, and D , G , and F are the microfacet distribution, geometric term, and the Fresnel term (see [35] for details). In the case of a smooth surface the diffuse Fresnel term, F_{dr} , given in Equation 5.27 specifies the fraction of diffuse light reflected at the surface. In the case of a rough surface we replace this term by an average

diffuse reflection, ρ_d . For the Torrance-Sparrow model there is no analytic approximation of the diffuse reflection, and we compute it using Monte Carlo sampling by evaluating the BRDF for random diffuse incident directions and averaging the resulting value for the reflection (this is done once for a given material).⁴

Once the diffuse reflection factor, ρ_d , is computed we can modify the A term (Equation 5.29) used in the computation of the extrapolation distance as follows:

$$A = \frac{1 + \rho_d}{1 - \rho_d}. \quad (7.18)$$

In addition, the BSSRDF (Equation 5.1) is changed by replacing both Fresnel terms with a diffuse transmission function

$$S_d(\vec{x}_i, \vec{\omega}_i; \vec{x}_o, \vec{\omega}_o) = \frac{1}{\pi} \rho_{dt}(x_i, \vec{\omega}_i) R(||\vec{x}_i - \vec{x}_o||) \rho_{dt}(x_o, \vec{\omega}_o), \quad (7.19)$$

where

$$\rho_{dt}(x, \vec{\omega}_o) = 1.0 - \int_{2\pi} f_r(x, \vec{\omega}_o, \vec{\omega}_i) (\vec{\omega}_i \cdot \vec{n}) d\vec{\omega}_i. \quad (7.20)$$

We assume all light that is not reflected by the BRDF model is transmitted into the material. Since ρ_{dt} is a fairly smooth function, we use numerical integration and generate a small table for different incoming angles. The use of ρ_{dt} is an approximation, as the transmitted light has a directional distribution described by a BRDF for transmitted light [105]. Since we use a diffusion model, however, this distribution can be ignored, and we consider all transmitted light to be diffuse.

The final model for the appearance of a rough translucent material consists of the diffusion model plus the BRDF for the reflection of light by the rough surface. As the surface roughness increases this model predicts that less light will be transmitted into the material, while more light is reflected directly by the surface. This results in a desaturation of the color of the translucent material as the importance of the (often white) surface reflection grows.

7.6 Rendering with the Multi-Layer Model

The multi-layered diffusion model is computed by evaluating the multipole for each layer, and using the Fourier transform technique described in the previous section to obtain

the total diffuse transmittance and reflectance of the material. Because no analytical transform of the multipole equation exists, we use the discrete Fourier transform to generate tabulated reflectance and transmittance profiles. Discretely sampling the profiles is computational efficient compared to re-evaluating the multipole for every pixel. This is particularly beneficial when capturing the properties of highly scattering extremely thin layers, where a large number of dipole pairs may be required. For thicker, less scattering single slabs, the analytic multipole model can be used directly. Both the analytic multipole and the tabulated profiles can be rendered using the same techniques as the dipole method.

The multi-layer model provides both a reflectance and a transmittance profile, but the geometry to be rendered determines how they should be used. As with the dipole model these profiles are only valid for planar slabs, and can only be used as approximations for other types of geometry. When modeling a multi-layered material such as skin it is sufficient in most cases to use only the reflectance profile to model the diffusion of light. In the case of complex thin (a few mean-free paths) geometry it is possible to blend the reflection and transmission profiles, depending on the normals \vec{n}_l and \vec{n}_s at the location of the incident light and the point being shaded

$$P_d(r) = \frac{1}{2}(\vec{n}_s \cdot \vec{n}_l + 1)R_d(r) + \frac{1}{2}(1 - \vec{n}_s \cdot \vec{n}_l)T_d(r) . \quad (7.21)$$

This equation computes a new profile as the weighted average of the reflected and transmitted profiles. Note that only the reflected profile is used if the normals point in the same direction, while only the transmitted profile is used if they point in opposite directions. One potential improvement to this formula would be to take into account the relative position of the two points as well (e.g. if the normals are facing each other). However, since the geometry between the point being shaded and the point being illuminated is unknown, there is no guarantee of accuracy. For applications that require high degrees of precision for small complex geometry, it is better to use Monte Carlo photon tracing or a multi-grid diffusion solver.

7.6.1 Texturing

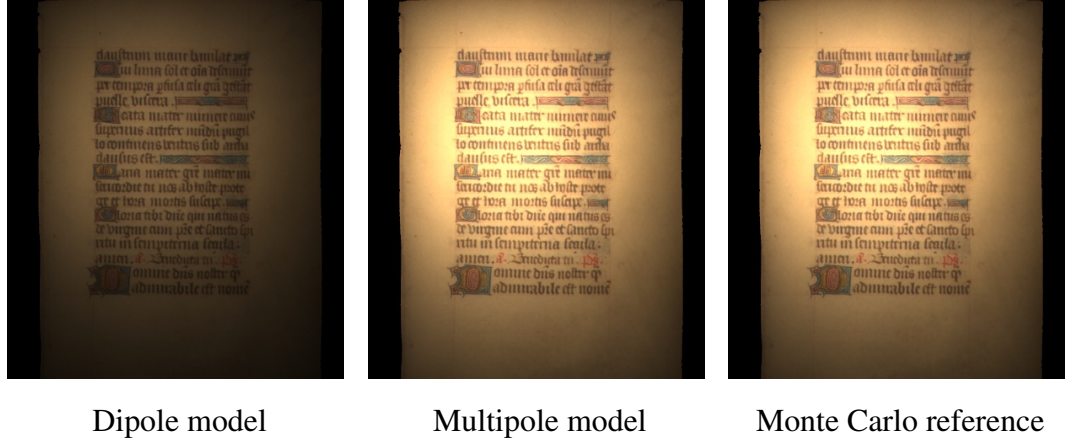
Texturing a multi-layered translucent material can be done in a number of ways. If the texture contains information about the scattering properties of each layer then it is possible to approximate the spatially varying reflectance and transmittance profiles by convolving the spatially varying reflectance and/or transmittance profiles for the individual layers (assuming that the surface is locally homogeneous). This process is costly as it has to be done for every point on the surface or for every texture element.

A simpler technique that works well in practice is to assume that the texture is given as an albedo map (e.g. diffuse reflectance) similar to textures used to shade opaque materials. This approach has been used on translucent materials based on the dipole model [49, 59]. If we further assume that only nearby texture values influence each other then we can account for texturing using the following approach.

- First, we convolve the texture with the reflectance profile (and the transmittance profile if thin geometry is being shaded). This effectively blurs the texture according to the diffusion of light (a similar approach has been used on the irradiance value by Borshukov and Lewis [13]).
- Next, we normalize the texture such that the average is a white color. This is done to ensure that the color of the diffusion process is used, rather than the texture color. If the texture color is important then the texture can be normalized by the reflectance and/or transmittance value predicted by the multipole method (we have not used this approach).
- Finally, during rendering we compute the effective diffusion of light using the reflectance and/or transmittance profile, and scale the predicted radiant emittance by the normalized texture value.

7.7 Visual results

We have already shown the accuracy of the combined multipole and convolution technique. In this section we present visual examples that show the ability of the method to



Dipole model

Multipole model

Monte Carlo reference

Figure 7.15: A piece of parchment illuminated from behind. Note, how the dipole model (left) underestimates the amount of transmitted light, while the multipole model (middle) matches the reference image computed using Monte Carlo photon tracing (right).

simulate light transport in various types of scattering materials. We have implemented the multi-layered diffusion model in a Monte Carlo ray tracer that supports direct sampling of scattering profiles as described in [62]. The images were rendered on a 2.8GHz Pentium IV, and the rendering times for the individual images were from one to five minutes. Preprocessing time to generate the scattering profiles ranged from five seconds to under one second, using 1000 dipole pairs to ensure accuracy.

Figure 7.15 compares the accuracy of the multipole method with the dipole method and Monte Carlo photon tracing. The scene contains a thin piece of parchment illuminated from behind. The parchment is roughly 1 mm. thick, which corresponds to approximately four mean free paths. The dipole predicts a transmittance of about 3.3% compared with 22.6% for the multipole and 21.5% for the Monte Carlo reference result. As a consequence, the parchment is too dark when rendered with the dipole diffusion model, while the multipole model more precisely predicts the correct appearance.

Figure 7.16 shows the effect of adding a thin layer of paint onto a thicker buddha statue made of jade. The paint is highly scattering of white light, while the jade absorbs most non-green light. Adding the paint layer causes the reflected light to become more white, and attenuates the amount of light that reaches the jade, causing the statue to look

more opaque. The transmitted light, however, remains green as it still scatters through the jade material.

As an example of the effect of surface roughness, Figure 7.18 demonstrates several renderings of a marble statue with different surface roughness values. As the surface roughness increases, the surface changes from having an oily appearance to looking more dry and rough. Another important change is the desaturation of the color of the statue due to an increase in the amount of reflected light, and a reduction in the amount of lighting due to subsurface scattering.

Figure 7.17 displays renderings of a leaf composed of a thick absorbing layer over a thin highly scattering layer, similar to [46], with absorption parameters taken from [33]. Note that while the orientation of the leaf affects the reflectance, the transmittance is nearly the same. This bicoloration is an important visual element of many leaves. For the leaf model, we applied both thickness and bump maps on the geometry to simulate the appearance of the leaf veins. The thickness map is effectively used as a displacement map, which increases the distance of the diffused lighting. This gives the effect of thickness, but it is only an approximation as the overall reflectance profile changes as a function of the thickness of each layer. The leaf color is caused by multiple scattering; no textures have been used.

Multiple layered models have been shown to be effective in simulating the optical properties of human skin [114]. In Figure 7.19 we demonstrate a three layer model of human skin applied to a high-resolution digital scan of a head. No bump map was used; the surface detail is due to the actual geometry of the model. The parameters for each layer are from Tuchin [114] and summarized in Table 7.2. The left images show the contribution each layer gives to the overall appearance, as well as the contribution of surface roughness at the top surface of the skin. The right image shows the full combination of all the layers with no texturing. The images in Figure 7.20 add texturing as described in the previous section. Note that although the individual layers may not appear to be skin-like, this is often the case of actual photographs of the bloodless top layers of human skin. Also, it is the overall reflectance from the convolution of these layers that gives the final appearance. The bloody dermis layer is assumed to be semi-infinite, which is often done to simulate the effects of internal tissues, while the highly

Table 7.2: Optical parameters used in generating the images in Figures 7.19– 7.21. η is the index of refraction, and d is the thickness of the layer.

	σ_a (mm^{-1})			σ_s (mm^{-1})			η	g	d (mm)
	R	G	B	R	G	B			
epidermis	2.1	2.1	5.0	48.0	60.0	65.0	1.4	0.0	.03
upper dermis	0.16	0.19	0.30	32.0	40.0	46.0	1.34	0.25	.05
bloody dermis	0.085	1.0	25.0	4.5	4.7	4.8	1.4	0.8	∞

scattering upper layers determine the softness and tint of the skin. Figure 7.20 also shows a comparison between the multilayer model and the dipole model using the parameters provided in [62]. The dipole overestimates the amount of scattering, giving the face a waxy, translucent look that blurs the features of the skin. The multi-layered model results in a less blurry appearance due to the improved approximation of the highly scattering epidermal and dermal layers compared with the bloody dermis. The overall appearance of the skin is still translucent as can be seen when the light is bleeding into shadowed regions, or when the skin is illuminated from behind (e.g. at the ear). Figure 7.21 shows a full rendering of the head with the complete model.

Note that parameters to the dipole model cannot always be used in the multipole model directly, as the dipole parameters are designed to capture the overall appearance of a semi-infinite sample of the material. Instead, the images in Figures 7.19– 7.21 have been rendered using parameters from existing work in tissue optics. These parameters are more intuitive than the parameters in the dipole model, since the specific properties of each layer can be modified (e.g. blood concentration or melanin) to change the overall appearance.

7.8 Summary and discussion

This Chapter presented a method for efficiently calculating the steady-state diffuse reflectance and transmittance profiles of arbitrary systems of diffusing layers, and introduced an efficient method for rendering them. We avoided solving complex boundary

conditions by convolving the reflectance and transmittance of profiles of individual layers. To improve accuracy, we corrected the convolution to account for inter-layer scattering using methods similar to Kubelka-Munk theory, but applied in frequency space using 3D diffusion profiles. We compared with Monte Carlo simulation using parameters taken from previously published work as examples of its applicability, and have shown good agreement. The correction to the convolution improves the accuracy of reflectance calculations far from the source, and has a significant impact on the calculation of transmittance, and the profiles of many-layered materials. The separation of the diffusion profiles into single-layer and inter-layer scattering has also shown an interesting result: far-source reflectance and transmittance in multi-layered materials is primarily due to inter-layer scattering. In particular, since the transmittance profile is due entirely to inter-layer scattering, accurate simulation of this phenomenon is essential. This suggests that the corrected convolution may be well suited for parameter estimation of multi-layered turbid materials using a combined reflectance and transmittance approach.

The primary source of error in the convolved responses near the source is the diffusion approximation itself. Near-source radiant emittance is dominated by single scattering, and is not accurately captured by either the dipole or multipole method. Also, though layered structures can be simulated, the embedding of arbitrary objects in layered materials is still not supported. In addition, it is difficult to measure the optical properties of layered materials, or to construct them intelligently. This issue is explored more in the next Chapter. Still, the new model is efficient and accurate, and it renders thin and layered materials such as paper, leaves, and skin faithfully.

7.9 Acknowledgments

Chapter 7, in part, is a reproduction of the material published in C. Donner and H. W. Jensen. *Light diffusion in multi-layered translucent materials*. *ACM Trans. Graphic.*, 24(3):1032–1039, 2005; and C. Donner and H. W. Jensen. *Rapid simulation of steady-state spatially-resolved reflectance and transmittance profiles of multi-layered turbid materials*. *J. Opt. Soc. Am.*, 23(6):1382–1390, 2006. The dissertation author was the

primary investigator and author of both papers.



Figure 7.16: A buddha statuette sprayed with a thin layer of white paint. The first and third images are front-lit, the second and fourth back-lit.

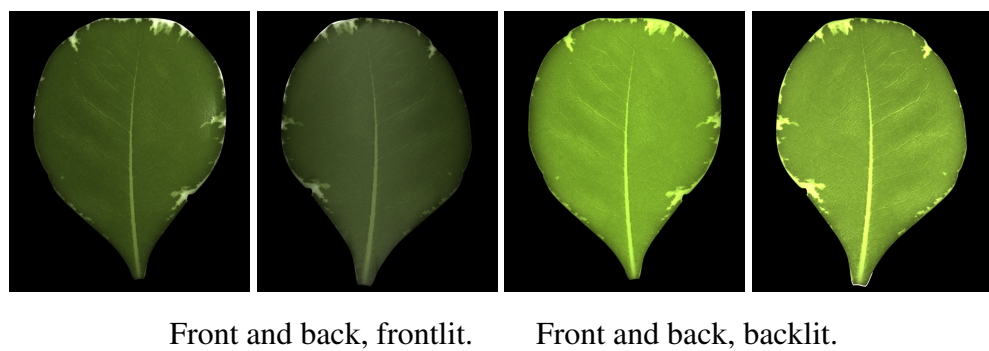


Figure 7.17: A layered leaf lit from front and behind. The reflectances of the front and back sides of the leaf differ significantly, while the transmittance is nearly identical. Note that the color is due to multiple scattering; no textures are applied.



Figure 7.18: A translucent marble statue with surface roughness 0.1 on the left, 0.5 in the middle, and 1.0 on the right. The smaller images show the subsurface scattering component and the roughness component of the smooth (0.1) and the rough (1.0) translucent statues. Note how the smooth version is more shiny and brighter due to a higher subsurface scattering component. As the surface gets rougher the surface reflection increases, which reduces the amount of subsurface scattering, and the overall result is a desaturation of the color of the marble material.

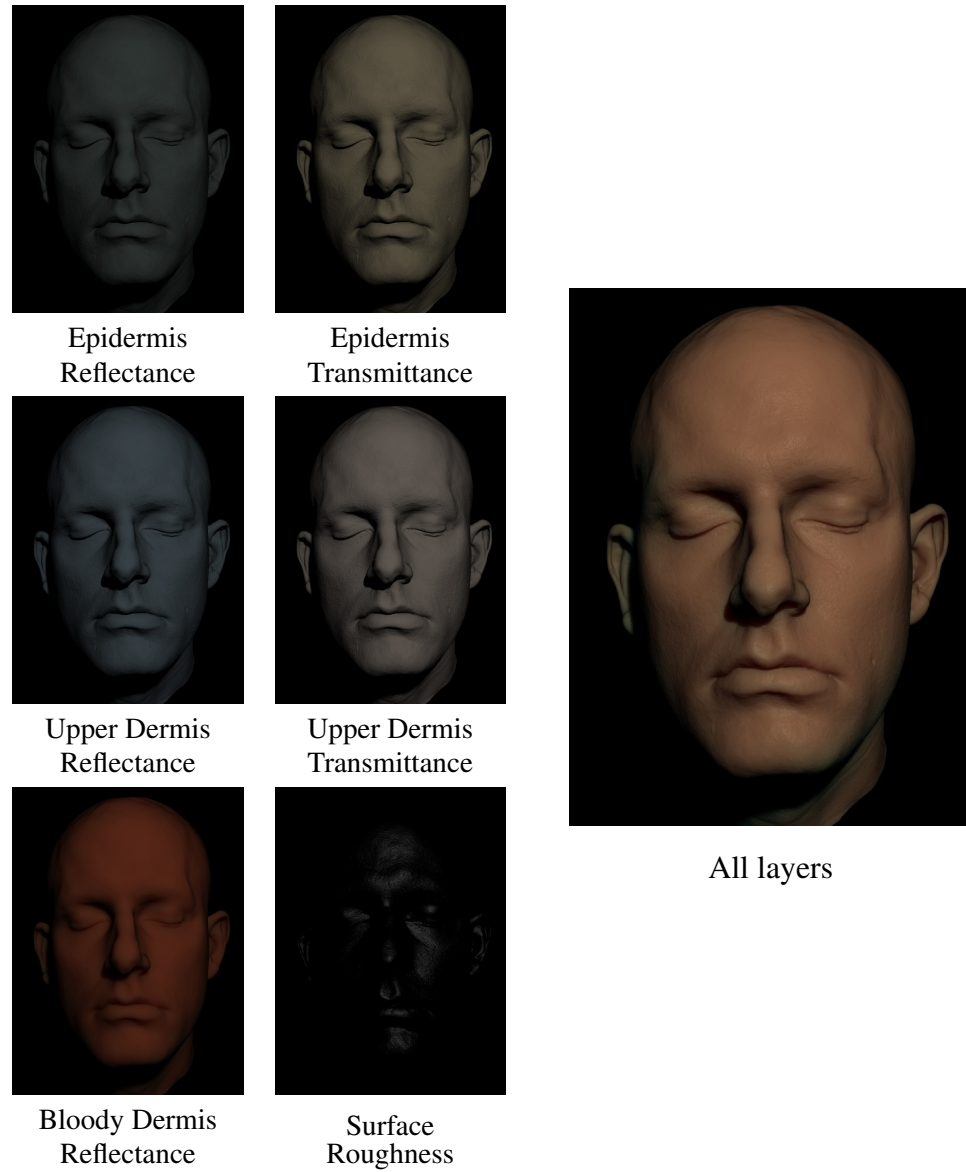
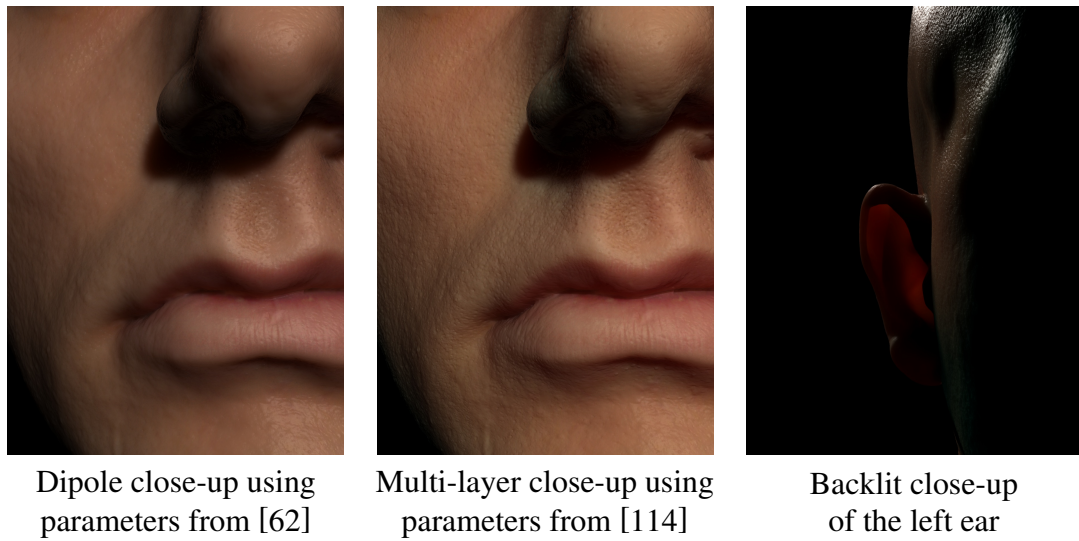


Figure 7.19: A multi-layered model of human skin using measured parameters for the individual skin layers [114]. The left images show the reflectance and transmittance of the epidermis, upper dermis, and the bloody dermis layers. The right image shows the combination of these layers using the multi-layer model.



Dipole close-up using parameters from [62]

Multi-layer close-up using parameters from [114]

Backlit close-up of the left ear

Figure 7.20: Closeups of the complete model in the case of rendering human skin. The top left and center images compare the dipole model using the parameters from [62] with the multi-layer model. Note how the combination of the different layers results in skin that captures both the translucency of the bloody dermis as well as the localized scattering in the epidermis. The top right image shows light scattering through the backlit ear.

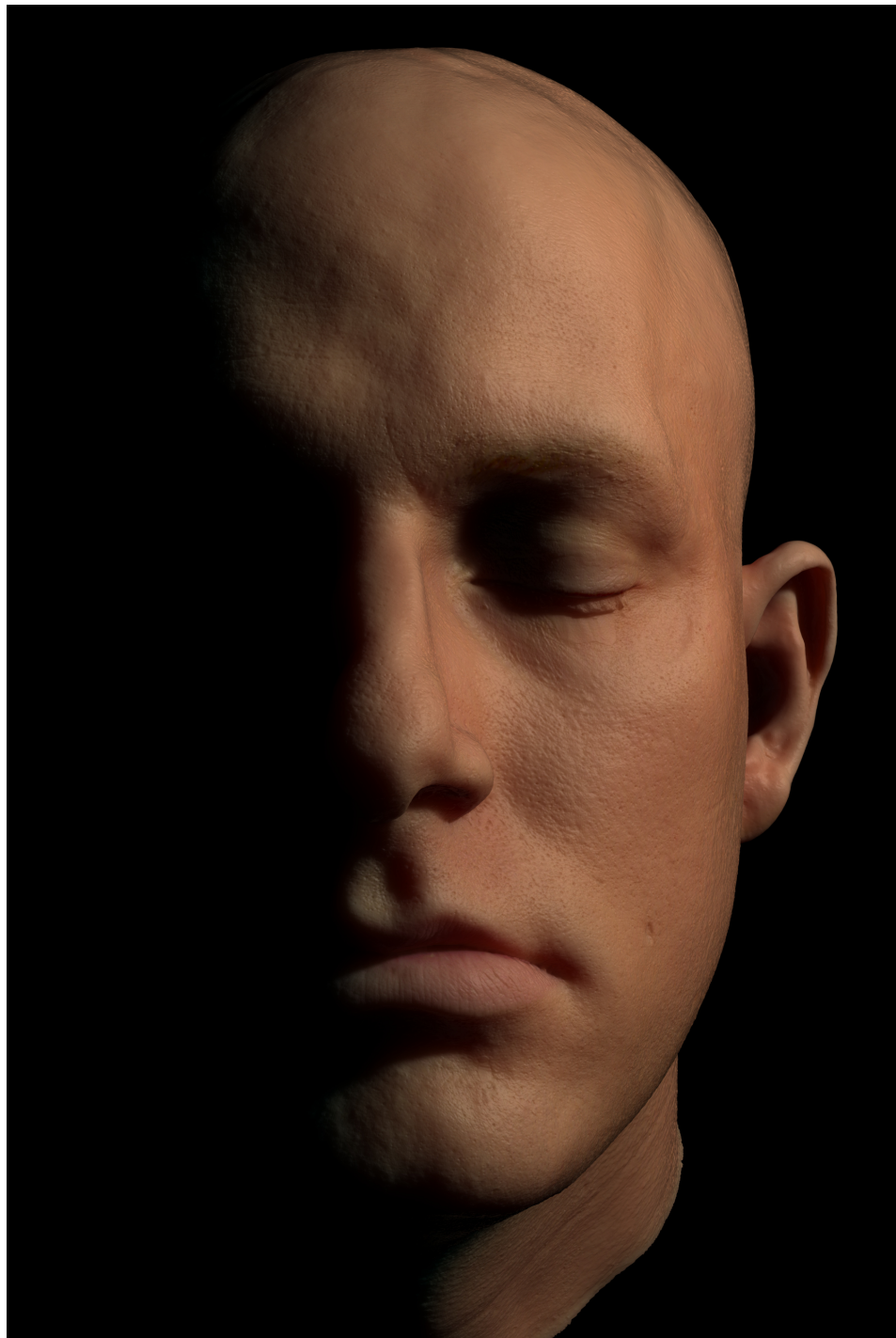


Figure 7.21: A full-face image using the complete model.

Chapter 8

A spectral shading model for human skin

One of the limitations of both the dipole and multipole concerns the selection of parameters. Both models require knowing the RGB reduced scattering and absorption coefficients, the phase function, and in the case of the multipole the thickness of each layer. As an example, consider the skin model from the previous chapter. For the three diffusing layers, there are a total of 7 parameters per layer, for a total of 21 parameters. Which parameters are most important for the overall appearance, and how do they interact? In particular, the interaction between the scattering and absorption coefficients are not only non-linear, but also deceptively counterintuitive. The final appearance produced by a diffusion profile depends on the relative strength of absorption and scattering, as well as the scale of the material. This presents the following problem: how can we choose parameters for a subsurface scattering model that produce predictable, intuitive changes in appearance?

This Chapter resolves that problem for the specific case of shading human skin. The model accounts for subsurface scattering using a BRDF, and surface scattering using the multipole method described in the previous chapter. To be practical, it uses only four parameters to simulate the interaction of light with human skin. These four parameters control the amount of oil, melanin and hemoglobin in the skin, which makes it possible to match specific skin types, and also give a more intuitive control to the BSSRDF. Using

these parameters, we generate custom wavelength dependent diffusion profiles for a two-layer skin model that account for subsurface scattering within the skin. Similar to the model in the previous Chapter, we combine the subsurface scattering simulation with a Torrance-Sparrow BRDF model to simulate the interaction of light with an oily layer at the surface of the skin. Qualitative and quantitative results demonstrate that this simple four parameter model makes it possible to accurately simulate the range of natural appearance of human skin including African, Asian, and Caucasian skin types.

8.1 Background

Simulating the appearance of human skin is a challenging problem due to the complex structure of the skin. Furthermore, even small variations in color and shade significantly influence the perception of skin, as they convey information about a person’s health, ethnicity, and physiological state. A physically accurate shading model that takes into account the full spectral interactions of light with tissue is essential for realistic renderings of human skin.

Debevec et al. [22] measured the reflectance field of human faces, allowing for rendering of skin under varying illumination conditions with excellent results. Jensen and Buhler [59], Hery [49] and Weyrich et al. [129] have investigated methods to measure the surface and subsurface properties of human faces. While these techniques can be used to reproduce measured data accurately, there is no clear way to modify model parameters arbitrarily to generate a desired appearance.

Tsumura et al. [110, 111] developed an image-based technique to recover and subsequently model the concentrations of melanin and hemoglobin in skin. Their method makes the assumption that melanin and blood have completely independent effects on skin color, which has been shown to not be the case [106]. Also, their technique is limited to specific camera-light combinations.

Krishnaswamy and Baranoski [72] developed the BioSpec model for simulating light interaction with human skin. The BioSpec model is based on a detailed model of human skin that uses physically obtained biological parameters to simulate the transport of light

through the different layers of skin. It models the spectral scattering and absorption properties of the skin, using brute-force Monte Carlo ray tracing to simulate scattering within the skin model. This makes the BioSpec model significantly more costly than diffusion style methods. In addition, there is no clear way to accelerate the BioSpec model using diffusion-based techniques, as it does not compute radially symmetric profiles. The model is quite complex having almost two dozen input parameters, and the interactions between parameters, as well their individual and combined effects on overall appearance, is complicated. It is also unclear how to determine these parameters for a desired skin type, making it difficult to use the BioSpec model for simulating the appearance of human skin.

In this Chapter, we present a practical physically-based spectral shading model for rendering human skin. The model accounts for subsurface scattering within the skin and surface reflection of the oily surface. It is controlled by four physically meaningful parameters that control the amount of melanin, hemoglobin, and the oiliness of the skin. We use the multipole to efficiently calculate spectral diffusion profiles for a two-layer model of the skin. These diffusion profiles are used during rendering to simulate the subsurface scattering of light within the skin. To account for the reflection of light by the oily skin surface we use a Torrance-Sparrow BRDF. We demonstrate our model by simulating different skin types (African, Asian and Caucasian), and show that it reproduces the spectral reflectance behavior characteristics of human skin.

8.2 The structure of skin and its interaction with light

The physical structure and chemical makeup of skin is a well studied topic in various scientific fields. Skin is known to have a distinct layered structure, with smaller-scale structures (hair follicles, wrinkles, sweat glands, capillary veins, etc.), all of which have some effect on appearance [50].

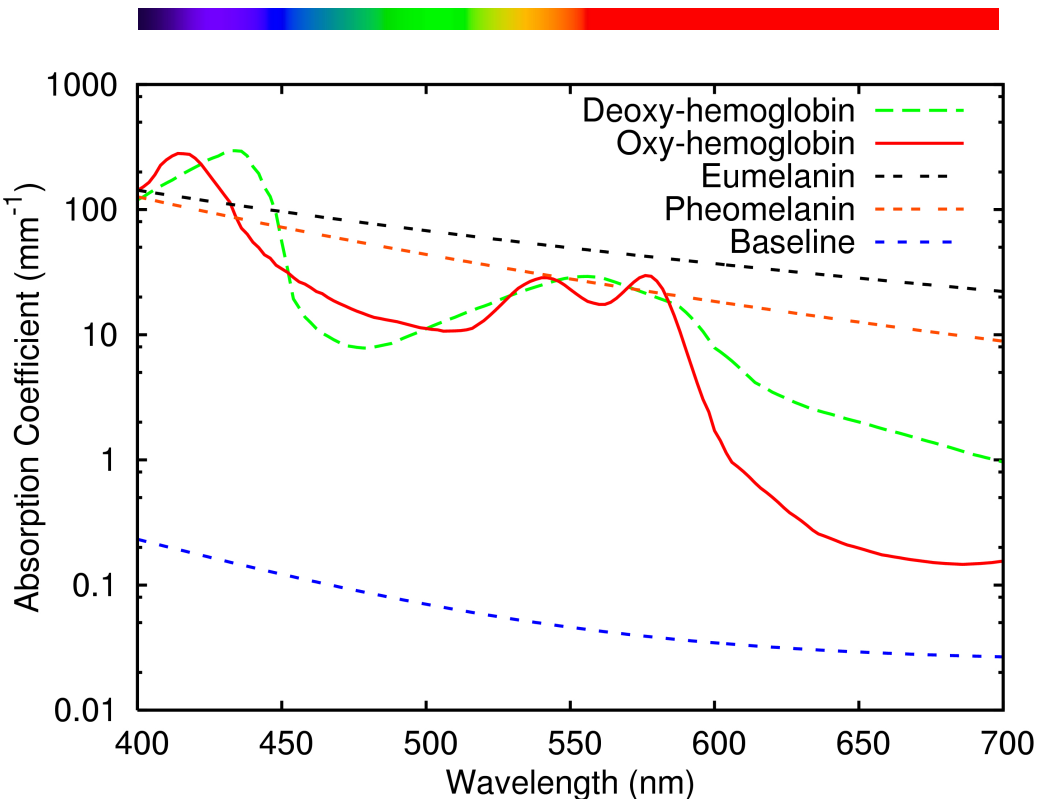


Figure 8.1: Spectral absorption coefficients of hemoglobin, melanins, and baseline skin absorption.

8.2.1 Absorption of light

The most striking feature of skin is its color, which is determined by absorbing chromophores distributed in the different layers. The most prominent chromophores that affect skin appearance are hemoglobin and melanin [4]. Hemoglobin is responsible for carrying oxygen throughout the body, and is the primary constituent of red blood cells. It comes in both oxygenated and deoxygenated forms, each with a slightly different properties. The absorption spectra of both oxy- and deoxy- hemoglobin are shown in Figure 8.1. Note the characteristic peaks in oxy-hemoglobin at 542nm and 547nm.

The other chromophore, melanin, is not actually a pure substance, but is composed of different polymers, and varies in color from light yellow to very dark brown or black [1]. Lighter melanin is composed mostly of *pheomelanin*, while the darker type is

generally *eumelanin*. Different concentrations of these basic molecular building blocks are believed to produce the various pigmentation of skin and hair seen in the natural world. Both melanins have a characteristically broad and smooth absorption band, with highest absorption in the UV range, decaying as wavelength increases (see Figure 8.1). This property likely makes them good safeguards against solar radiation. Recent work suggests that the *type*, rather than total concentration, of melanin is the primary factor in skin coloring [1]. Although the most significant absorber in the darkest skin is eumelanin, in somewhat lighter skin colors (e.g. Asian skin), there is a wide range of concentrations of the different types of melanin [1, 2, 52, 121]. The particular type distribution varies by individual, even within a single ethnic group.

There are small concentrations of other chromophores carried in the blood, such as bilirubin and beta-carotene, but their visible contribution in healthy skin is negligible [4, 81]. The other structures in skin, such as internal cellular structures and organelles, also play some small part in absorbing light.

8.2.2 Scattering of light

Besides having a complex absorption spectrum, skin is also a highly scattering material. This is primarily due to high frequency changes in index of refraction within the small-scale structures of the skin, and in particular due to collagen and elastin fibrils that run beneath the surface [4]. The distribution of these fibrils generally decreases in concentration with depth [81]. Chromophores also play a small role in the scattering of light within the skin.

8.2.3 Skin layers

Skin has a definite layered structure. The highest level of the skin is the *stratum corneum*, and is quite thin, highly scattering, but absorbs almost no light. The layers below the stratum corneum are associated with the epidermis, and this is where most of the melanin in skin is found [4]. Below the epidermal layers is the dermis, where the vascular network carrying nutrients to tissues via the blood is found. The dermal

layers contain most of the blood in healthy skin. Even deeper below the dermis is the subcutaneous tissue, such as fat, but it has little effect on visible appearance [81].

The skin also secretes an oily substance, the sebum, which contributes to the direct surface reflection of light [84]. Light that is not reflected off the surface scatters amongst the tissues of the skin, where it is either absorbed by chromophores, or scattered out.

8.3 A two-layer model for human skin

In this section we present a new practical appearance model for skin. We draw on some of the ideas behind both the BioSpec [72] and the previous two chapters, but focus on developing a model with a minimal set of parameters most important for skin appearance. The goal is a model that is realistic, but also intuitive and simple to control. We use four parameters to control the oiliness, hemoglobin concentration, melanin concentration, and a blend factor between the different types of melanin. Each of these is discussed in more detail below.

Our shading model consists of three terms

- a surface reflection term for directly reflected light due to oil,
- a spectral subsurface scattering term for light transported through the skin,
- and a texturing term using a surface albedo map.

The skin color produced by our model is given as the sum of the surface reflection and the texture-modulated subsurface scattering terms.

8.3.1 Surface reflection

Direct reflection is due mostly to oil on the surface of the skin, as well as the skin's intrinsic roughness. We also include scattering from the stratum corneum in this term, as this thin highly scattering layer does not significantly blur the incident light.

As before, we model direct reflection with the Torrance-Sparrow microfacet BRDF [109], which has been previously shown to give good visual results when fitting specular

highlights from skin [22, 129]. Again, the BRDF is

$$f_r = \rho_s \frac{F(\vec{x}, \vec{\omega}_o, \vec{\omega}_i) D(\vec{x}, \vec{\omega}_o, \vec{\omega}_i, \sigma) G(\vec{x}, \vec{\omega}_o, \vec{\omega}_i)}{4(\vec{\omega}_i \cdot \vec{n})(\vec{\omega}_o \cdot \vec{n})}$$

where $\vec{\omega}_i$ and $\vec{\omega}_o$ are the incoming and outgoing lighting directions, F is the Fresnel reflectance, G is the geometry term, and D is the Beckmann microfacet distribution [18]. The parameter σ controls the RMS slope of the microfacets, and is often referred to as the “roughness” parameter. We have found that values for σ in the range $0.2 - 0.4$ give good results for skin, and we use $\sigma = 0.35$ for all our results. Rather than change σ , we use ρ_s as a linear scale to control the oiliness of the skin surface.

Similarly to the previous Chapter, we calculate an average diffuse reflectance by integrating the BRDF over the outgoing hemisphere

$$\rho_{dr}(\vec{x}, \vec{\omega}_i) = \int_{2\pi} f_r(r, \vec{\omega}_o, \vec{\omega}_i)(\vec{\omega}_i \cdot \vec{n}) d\vec{\omega}_o. \quad (8.1)$$

Any light that is not reflected is assumed to transmit into the skin, thus the subsurface scattering term is modulated by $(1 - \rho_{dr})$. This helps ensure conservation of energy. In most cases, less than 10% of the incident light is reflected at the surface, making this a good approximation of the actual light distribution.

8.3.2 Subsurface scattering

We simulate subsurface scattering in a two layered model of the skin (see Figure 8.2). Many other authors have found a two-layer model to be sufficient for skin [103, 107, 111, 116], though existing models range from a single layer [62] to seven layers [81]. Closer analysis of the properties of different layers of skin, however, shows that there is little variation in their optical properties [81], and that a two-layer separation into an epidermal and dermal layer is adequate [4].

To model the scattering and absorption of light in the skin, we have developed a two layer skin model, representing the skin as an epidermis and dermis. We use the multipole diffusion model to compute spectral diffusion profiles that can be directly used for rendering. To use the multipole it is necessary to know the optical properties of each layer, namely their absorption and reduced scattering coefficients σ_a and σ'_s . For skin,

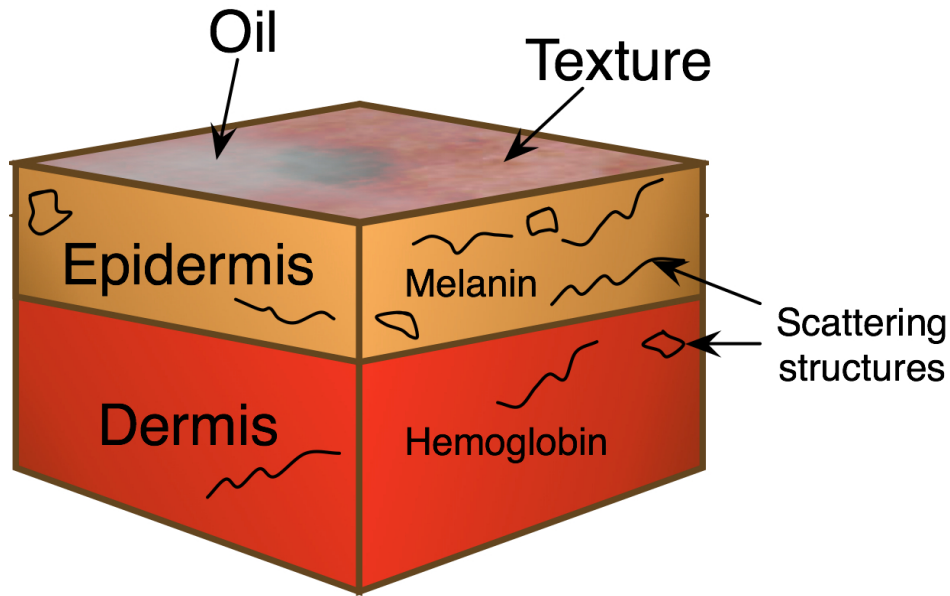


Figure 8.2: Two layer model of skin.

these coefficients are determined by the chemical composition and structure of each layer, and we describe those elements in the following sections.

8.3.3 Absorption by the epidermis

The primary chromophore in the upper areas of skin is melanin. As mentioned previously, melanin is not a pure substance, but rather a complex combination of different molecules. Both the amount and type of melanin present in the skin are thought to contribute to overall color. The two extreme types of melanin are brown-black eumelanin, and yellowish-red pheomelanin.

Because both types of melanin have fairly featureless absorption spectra, increasing with shorter wavelength, their absorption spectra are approximated well by simple power laws [96]

$$\sigma_a^{em}(\lambda) = 6.6 \times 10^{10} \times \lambda^{-3.33} \text{ mm}^{-1} \quad (8.2)$$

$$\sigma_a^{pm}(\lambda) = 2.9 \times 10^{14} \times \lambda^{-4.75} \text{ mm}^{-1} \quad (8.3)$$

where λ is the wavelength of light in nanometers, σ_a^{em} is the spectral absorption coef-

ficient of eumelanin, and σ_a^{pm} of pheomelanin. Equation 8.2 fits data from [55], while Equation 8.3 is our empirical fit to data from data in [98]. Baseline skin absorption from other small scale tissues in the epidermis (organells, cell membranes, fibrils, etc.) is approximated by [54]

$$\sigma_a^{baseline}(\lambda) = 0.0244 + 8.53e^{-(\lambda-154)/66.2} \text{ mm}^{-1} \quad (8.4)$$

We assume that both melanin and the small scale tissues are uniformly distributed throughout the epidermis. We define the total spectral absorption of the epidermis to be a combination of absorption from both

$$\begin{aligned} \sigma_a^{epi}(\lambda) = & C_m (\beta_m \sigma_a^{em}(\lambda) + (1 - \beta_m) \sigma_a^{pm}(\lambda)) \\ & + (1 - C_m) \sigma_a^{baseline} \end{aligned} \quad (8.5)$$

where C_m is the total volume fraction of melanin in the epidermis, and β_m controls the amount of eumelanin relative to pheomelanin, and allow for a light tan or yellowish appearance. Low values of β_m give primarily pheomelanin, while values of β_m near 1 give primarily eumelanin, and give skin a brown or black appearance. Note that both kinds of melanin are found in various concentrations in most individuals, regardless of race, though it is generally thought that certain skin types are more likely to contain higher amounts of pheomelanin, such as Asian skin [47]. Darker skin types, such as African skin, contain higher total concentrations of melanin, mostly eumelanin.

8.3.4 Absorption in the dermis

The dermal layer approximates the deeper areas of skin that contain the vascular capillary network carrying blood. Here the primary chromophore is hemoglobin [103]. Hemoglobin exists in both an oxygenated and deoxygenated state within the dermis, each with a somewhat different absorption spectrum as shown in Figure 8.1. Again, we assume that hemoglobin is uniformly distributed in the dermis. We define the total spectral absorption of the dermis as a combination of absorption from hemoglobin and small scale structures

$$\sigma_a^{derm}(\lambda) = C_h \left(\gamma \sigma_a^{oxy}(\lambda) + (1 - \gamma) \sigma_a^{deoxy}(\lambda) \right) + (1 - C_h) \sigma_a^{baseline} \quad (8.6)$$

where C_h is the fractional amount of hemoglobin in the dermis (usually about 0.1% – 20% depending on location and skin type), and γ is the blood oxygenation ratio between deoxy- and oxy-hemoglobin. γ varies only slightly over different skin types and body locations from about 0.6 – 0.8 [133]. In our model we fix γ to be 0.75.

8.3.5 Scattering and thickness

The spectral scattering of light due to elastin and collagen fibrils, as well as other small-scale structures and chromophores in the skin, is approximated well by power laws that model a combination of Mie and Rayleigh theory [6]

$$\sigma'_s(\lambda) = 14.74\lambda^{-0.22} + 2.2 \times 10^{11} \times \lambda^{-4}. \quad (8.7)$$

The deeper regions of the skin are generally less scattering than the upper areas, as there is a lower concentration of scatterers [53]. We assume that the reduced scattering coefficient is constant throughout each layer, but we scale the reduced scattering coefficient by 50% in the dermis, where the skin is more translucent.

We fix the thickness of the epidermal layer to 0.25mm, as chromophore pigmentation dominates the effects of changing thickness [97]. For simplicity, we also assume a constant index of refraction of 1.4 throughout the skin, as the actual index changes only slightly [81]. Since little light reaches subcutaneous tissue, we assume the dermis to be semi-infinitely thick.

The above equations generate spectral absorption and reduced scattering coefficients for the two skin layers. These become wavelength dependent inputs to the multipole model, which generates spectral diffusion profiles for each layer and convolves them together to provide a single, spectral diffusion profile for skin.

8.3.6 Texturing

An efficient way to locally modify the subsurface scattering term is to modulate it with an albedo texture. This includes fine scale details such as freckles, splotches, etc. Rather than requiring recalculation of diffusion profiles over the entire skin surface, we enable this local change directly with texture maps.

Table 8.1: Parameters to our model.

Parameter	Description	Typical range
C_h	Hemoglobin fraction	0.001 – 0.1
C_m	Melanin fraction	0 – 0.5
β_m	Melanin type blend	0 – 1
ρ_s	Oiliness	0 – 1

Since most textures include overall color data, they may include global melanin and hemoglobin pigments. These can be approximately removed by normalizing the texture as in the previous Chapter. Since we know the chromophore contribution *a priori*, we can remove an assumed chromophore contribution. This is done by first finding the total diffuse reflectance (Equation 5.36) calculated using assumed values of C_h , C_m , and β_m . Each pixel in the texture is then divided by this total diffuse reflectance rather than the texture average, leaving only local color variation. Removing global color from the texture in this way also provides an easy way to match existing images of skin, as the multiplication of the subsurface scattering term recovers the original texture color.

8.4 Implementation

Table 8.1 summarizes the four parameters to our model, with typical values. To use the model the user chooses values for each of the parameters C_m , β_m and C_h . These parameters, using Equations 8.2-8.7, directly give the spectral scattering and absorption coefficients of both the epidermis and dermis. We currently sample every 2nm from 400nm to 700nm to ensure accurate representation of the spectra, but such high-resolution sampling is not required. We have also tried converting these spectra to RGB absorption and reduced scattering coefficients, but this tends to overly smooth the effective spectra. The complex spectral interactions between the diffusion profiles of the layers are lost, leading to undesirable and unrealistic results. This finding is consistent with previous work [72].

Using the diffusion multipole, we calculate diffusion profiles for both layers using their spectral properties, and convolve them together to get a spectral diffusion profile for

skin. During rendering, this profile is sampled using standard Monte Carlo techniques as described in [62] to generate the subsurface scattering component. In our current implementation, the profile generation is done as a pre-process, and takes a few seconds. Conversion to RGB to generate images is done by first converting the calculated subsurface scattering color to XYZ and then RGB using the standard CIE 2° color matching functions, with the D65 illuminant. This resulting RGB value is scaled by the diffuse surface BRDF and albedo texture, and surface reflection is added as described in the previous sections using the parameter ρ_s . Overall rendering times are comparable to those of [62], as the spectral sampling adds little overhead to the underlying algorithm.

8.5 Results

We have implemented the skin model in a Monte Carlo ray tracer capable of sampling spectral diffusion profiles. In the following, we examine how the four parameters of the model influence the appearance of rendered skin, and we show examples for different skin types. Unless explicitly stated, the images are of untextured skin. The rendering times for all images are below 10 minutes on a standard PC.

Many of the following figures show rendered images of small patch of skin on the right cheek of a model of a human head. We show only this patch of skin rather than the full face to better illustrate the change in overall skin color. When an entire face is shown, other facial characteristics (bone structure, eye shape, etc.), are distracting and adversely influence the perception of how “real” the skin looks.

Figure 8.3 shows the effect of changing the melanin volume fraction C_m . The image shows a patch of skin on the right side of a face. Although only a single parameter is adjusted in this figure, a wide range of different skin types is simulated. From left to right, the changes in skin coloration reflect an increase in total melanin fraction from 0.1% to 50%. The leftmost images correspond to light Caucasian skin, while the rightmost images correspond to dark African skin. The middle images resemble tanned Caucasian or light Asian skin. The melanin blend β_m is held constant at 0.7, indicating 70% eumelanin and 30% pheomelanin, which gives these skin patches a characteristic beige/tan/brown

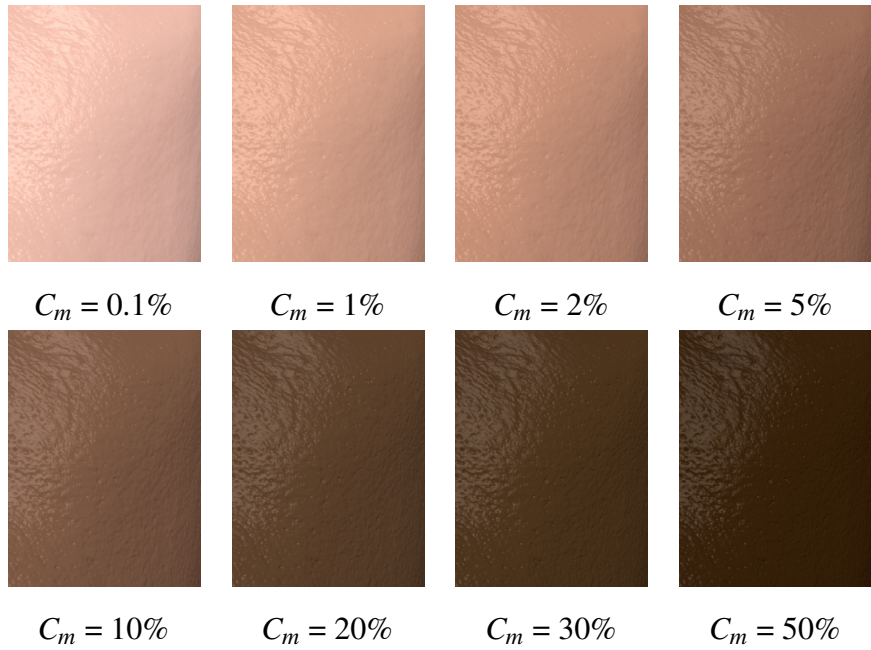


Figure 8.3: Change in skin color of a skin patch as melanin volume fraction C_m is increased from 0.1% to 50%. Note the change in color from light Caucasian skin to dark African skin as the total amount melanin increases. The melanin blend β_m is fixed at 0.7, which is 70% eumelanin, and 30% pheomelanin. The hemoglobin fraction C_h is constant at 0.5%, and the oiliness ρ_s is 0.5.

appearance.

To illustrate the effect of changing hemoglobin volume fraction, Figure 8.4 shows the effect on skin color as C_h increases from 0.1% to 20% from left to right. Low values of C_h generate pale translucent skin, while higher values give pink and purple skin. Note that the skin does not become red, as in the case of a sunburn, as hemoglobin is only increasing in the dermis, and not the epidermis. Simulating this effect would require adding an additional hemoglobin fraction to the epidermis.

Next, in Figure 8.5, we show the effects of adjusting the melanin blend β_m from 0 to 1 from left to right. Lower values of β_m (higher pheomelanin content) give the skin a more yellowish appearance, which is common in dark Asian skin. Higher values of β_m (higher eumelanin content), make the skin a pure brown, consistent with African skin. Note that β_m does not have a significant effect on lightly pigmented skin (low values of

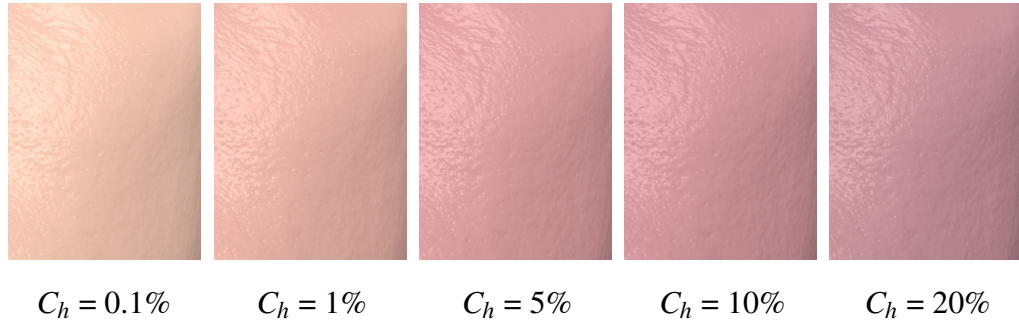


Figure 8.4: Change in skin color of a skin patch as the hemoglobin fraction C_h is increased from 0.1% to 20%. Less hemoglobin gives rise to a pale, translucent appearance to the skin, while more hemoglobin makes the skin look pink, and then purple. Total melanin fraction C_h is fixed at 1%, with β_m at 0.5. The oiliness ρ_s is 0.5.

C_m), since it has low amounts of total melanin.

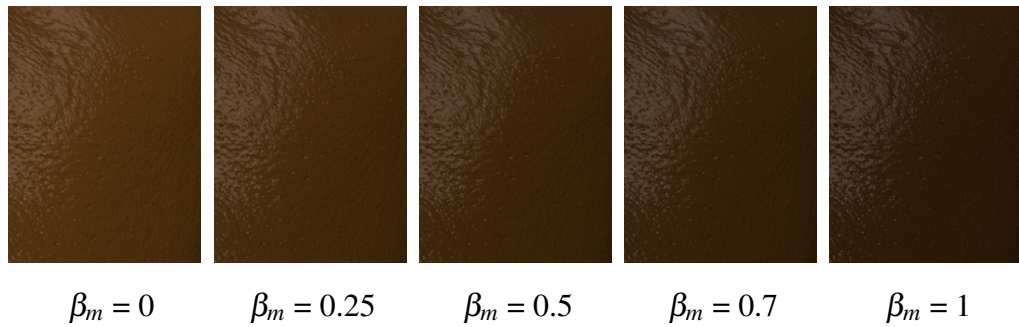


Figure 8.5: Change in skin color of a skin patch as the melanin blend β_m increases from 0 to 1. Lower values of β_m (more pheomelanin) give the skin a more yellowish appearance, while higher values (more eumelanin) give pure shades of tan and brown. The hemoglobin fraction C_h is constant at 0.1%, the total melanin volume fraction C_m is 50%, and the oiliness ρ_s is 0.5.

Figure 8.6 shows the effects of adjusting the oiliness, ρ_s ; the surface roughness σ is fixed at 0.35. Too little oil leaves the skin looking dry and diffuse, while too much gives the skin a wet and overly shiny appearance. In this figure, the amount of oil is kept constant over the surface of the skin, but it could easily be varied spatially with a parameter texture map, as the surface contribution is independent of the subsurface and texture components.

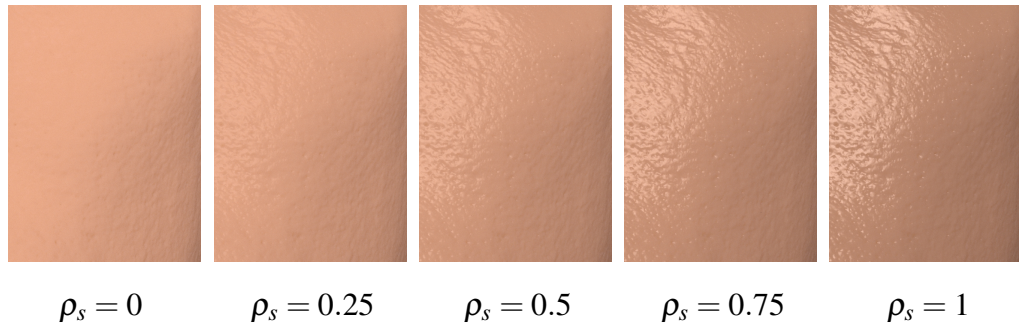


Figure 8.6: Effect of changing ρ_s . Little or no oil leaves the skin looking featureless and diffuse, while increasing ρ_s adds specular detail to the surface, resulting in a more realistic appearance. Higher amounts of oil tend to desaturate the skin color, as more light is directly reflected at the skin’s surface.

Figure 8.7 demonstrates the overall effects of changing only the three chromophore parameters of the model (C_m , C_h , and β_m). The parameters used are summarized in the figure captions. From left to right, melanin increases, and from top to bottom hemoglobin increases while the melanin blend changes decreases. Caucasian skin corresponds roughly to the upper left corner of the figure, with dark African skin in the upper right. Asian skin tends to fall near the middle of the figure, though there is the possibility for wide variation.

Using the four model parameters, it is simple to transition from the characteristics of one skin type to another by slightly adjusting the parameters. Figure 8.9 shows possible combinations of parameters to simulate different racial skin tones. On left side of the figure is light colored skin corresponding to Caucasian skin, while the right side image showing African skin has a much higher volume fraction of melanin. Both extremes have high concentrations of eumelanin. The middle image, corresponding to Asian skin, has a blend of eumelanin and pheomelanin. The far right image shows the effect of applying an albedo texture to the Caucasian skin; this increases the realism of the face as it adds variation as well as making the lips more reddish. The lower row of thin images show sections of photographs of real skin samples taken of the side of the face and neck from people of the corresponding ethnicities. These photographs were taken in a dark room under similar lighting conditions.

For a quantitative validation of the accuracy our model, Figure 8.8 compares generated total diffuse reflectance spectra to actual measured data from the NCSU spectral database [120]. The spectra were calculated using Equation 5.36, completely decoupled from rendering. Note the simulated spectra capture the characteristic “W” shape in the middle of the visible spectrum due to the peaks in the hemoglobin absorption in the dermis, and the flattening of the spectra as melanin content increases. As shown in the figure, our model well approximates the shape of skin reflectance spectra, despite the simplicity of the model. The tradeoff for practicality is unfortunately a loss in precision, particularly below 450nm, but this does not seem to adversely affect the final color of skin during rendering. The parameters used to generate each profile are listed in the figure legend.

In Figure 8.10 we show different combinations of lighting and viewing directions on textured Caucasian skin (both pale and with a tan). The texture is an albedo texture map applied to the face using the technique in the previous Chapter. Figure 8.11 shows the model in various lighting conditions.

8.5.1 Spectral vs RGB diffusion profiles

The BSSRDF is commonly implemented in an RGB shader; the original dipole model was presented as a three channel model [62]. To realistically capture the appearance of skin using the model described in this Chapter requires full spectral profiles. Figure 8.12 compares two closeup images of the head model. The left image was rendered using spectral profiles sampled every 2nm as described in this Chapter. The right image was rendered using RGB profiles, similar to the previous Chapter, but, generated by converting each slice of the spectral profile into an RGB triplet.

The spectral and RGB profiles used to generate the images in Figure 8.12 are shown for comparison in Figure 8.13. Note that the RGB profiles do not always have valid values over the entire distance range as the spectral profiles. This is because spectral data can represent colors not found in the RGB space, and a slice of the spectral profile may map to negative values, particularly further from the source as intensities become small. The RGB triplet cannot fully reproduce the complex reflectance characteristics

shown in the spectral profiles. The RGB profiles comprise three slices of a much larger domain; this very coarse approximation causes overestimation of the far-source radiant emittance, particularly in the red channel, giving the overly translucent appearance in the RGB profile image at the right of Figure 8.12. This is most evident near the lips and nose where most of the detail of the skin is lost.

This problem has also been identified in dermatology and pigment cell research, where researchers have recently become aware of the limitations of RGB and CIE LAB colorspace when capturing and predicting the reflectance spectrum of skin. Though there are weak correlations between chromophore concentrations in skin and channels in the LAB colorspace, these correlations are not strong enough to predict the LAB color of a particular skin type [106].

Using spectral instead of RGB profiles does not significantly increase render time, as importance sampling of the profiles is unchanged from before. The only extra computation is in converting the computed reflected or transmitted radiance back to RGB space, which is not significant. It should be noted, however, that it *is* possible to render images of skin without fully spectral profiles, as done in Chapter 7. To make use of the method outlined in this Chapter, however, requires the full reflectance spectrum to be evaluated, as the optical properties of skin are represented spectrally. If a similar $\text{RGB} \rightarrow \text{RGB}$ mapping exists, but since the multipole represents a non-linear transform from optical properties to diffusion profiles, there is no clear extension from the model presented in this Chapter.

8.6 Summary

This Chapter presented a practical spectral shading model for human skin, that uses four physically based parameters to simulate a wide range of skin appearance including African, Asian and Caucasian skin. We model the skin as a two-layer translucent material, accounting for spectral absorption and scattering within the layers with the multipole model, and the surface reflectance with a specular BRDF. The four parameters to the model are total melanin content, melanin type, hemoglobin content, and surface oiliness.

Despite its relative simplicity, the model gives a good appearance when rendering, and also closely simulates the spectral reflectance of real skin samples.

8.7 Acknowledgments

Chapter 8, in part, is a reproduction of the material published in C. Donner and H. W. Jensen. *A spectral BSSRDF for shading human skin*. In *Rendering Techniques*, pages 409–417, 2006; and C. Donner and H. W. Jensen. *A spectral shading model for human skin*. In *ACM SIGGRAPH Sketches and Applications*, 2006. The dissertation author was the primary investigator and author of both papers.

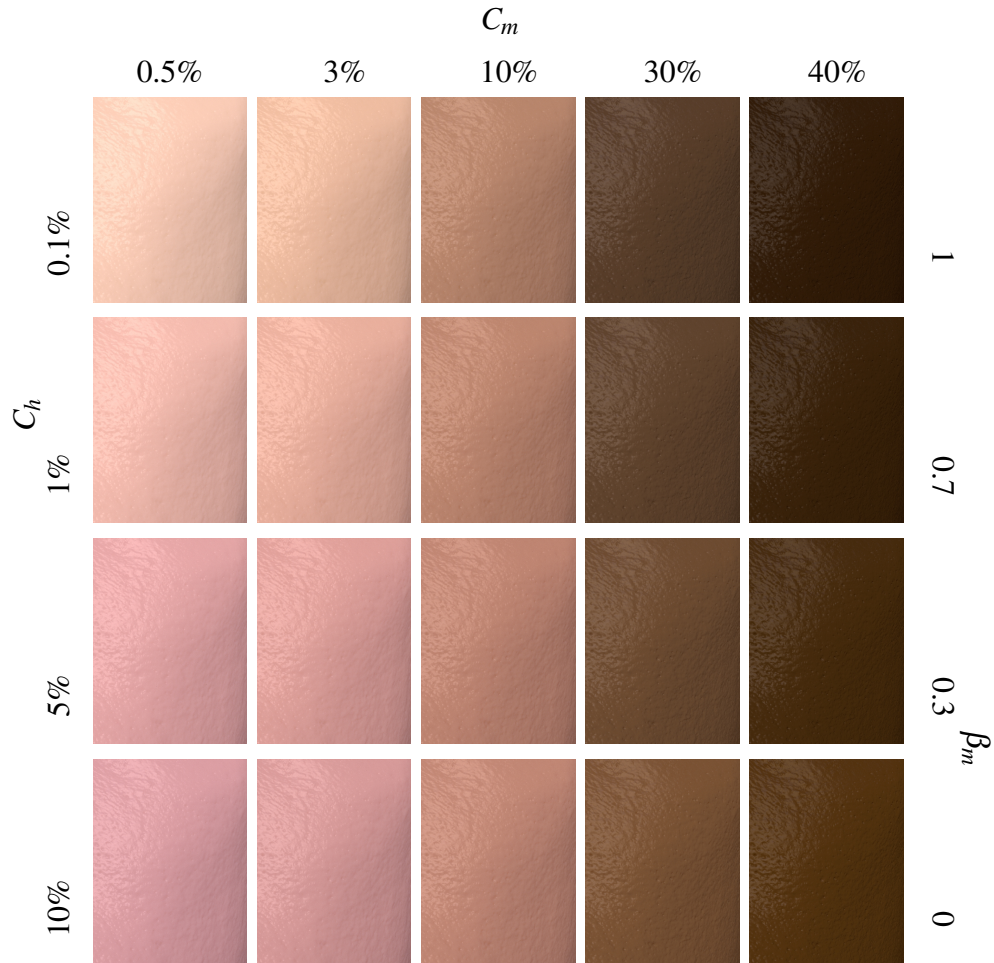


Figure 8.7: Images showing the change in skin subsurface reflectance and color bleeding over the range of appearance produced by melanin, melanin blend, and hemoglobin change. The sweatiness/oiliness was kept constant at $\rho_s = 0.4$. Note that darker skin appears wetter because more of the light transmitted into the skin is absorbed, even if surface reflectance is the same compared to lighter skin. Also, the effects of higher blood concentration are less apparent in darker skin, as melanin absorption dominates. From top to bottom, the melanin blend β_m changes from 1 to 0.7, 0.3, and 0, and hemoglobin fraction C_h increases from 0.1% to 1%, 5%, and 10%. From left to right, the total melanin fraction increases from 0.1% to 0.5%, 3%, 20%, and 50%.

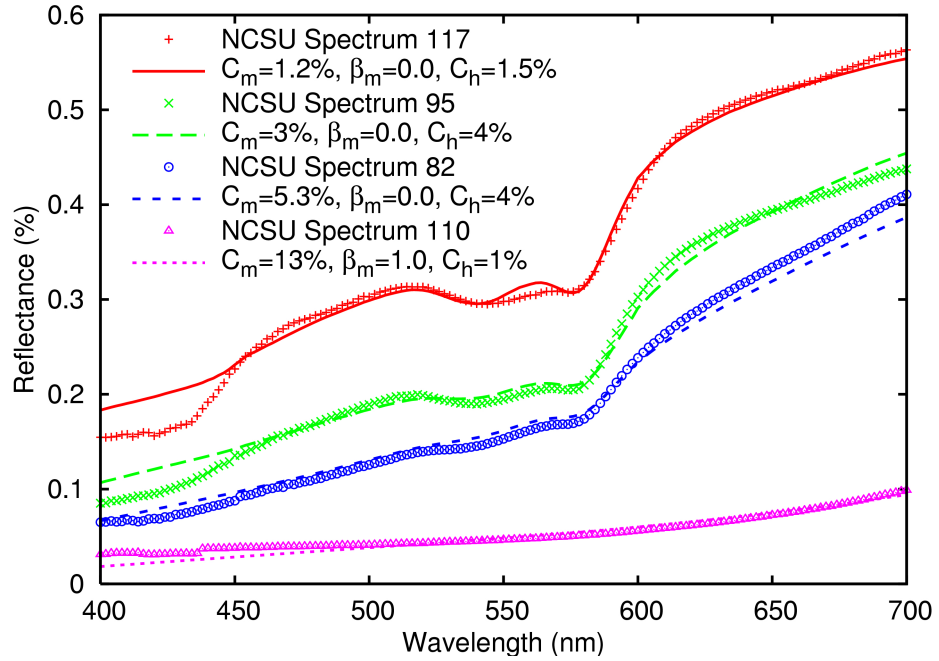


Figure 8.8: Calculated total diffuse reflectance spectra compared to measured data from [120]. From top to bottom, we compare with light Caucasian skin (spectrum number 117 in [120]), dark Caucasian skin (spectrum 95), Asian skin (spectrum 82) and African-American skin (spectrum 110).

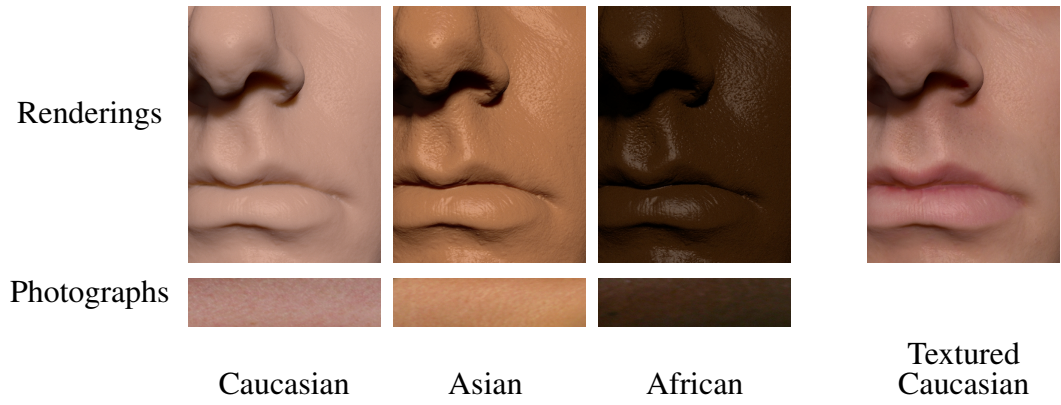


Figure 8.9: Different skin types simulated with our model (top) compared to actual photographs of real skin samples (bottom). For Caucasian skin, $C_m = 0.5\%$, $\beta_m = 0.7$, $C_h = 0.5\%$, and $\rho_s = 0.3$. For Asian skin, $C_m = 15\%$, $\beta_m = 0$, $C_h = 1\%$, and $\rho_s = 0.3$. For African skin, $C_m = 50\%$, $\beta_m = 0.7$, $C_h = 5\%$, and $\rho_s = 0.3$. The far right image applies an albedo texture to the Caucasian skin.



Figure 8.10: Applying skin parameters to an entire face with texturing. The left image showing light pale Caucasian skin was generated with $C_m = 0.3\%$, $\beta_m = 0.25$, $C_h = 0.5\%$, and $\rho_s = 0.3$. The right image showing well-tanned Caucasian were generated with $C_m = 2\%$, $\beta_m = 0.25$, $C_h = 0.1\%$, and $\rho_s = 0.25$.

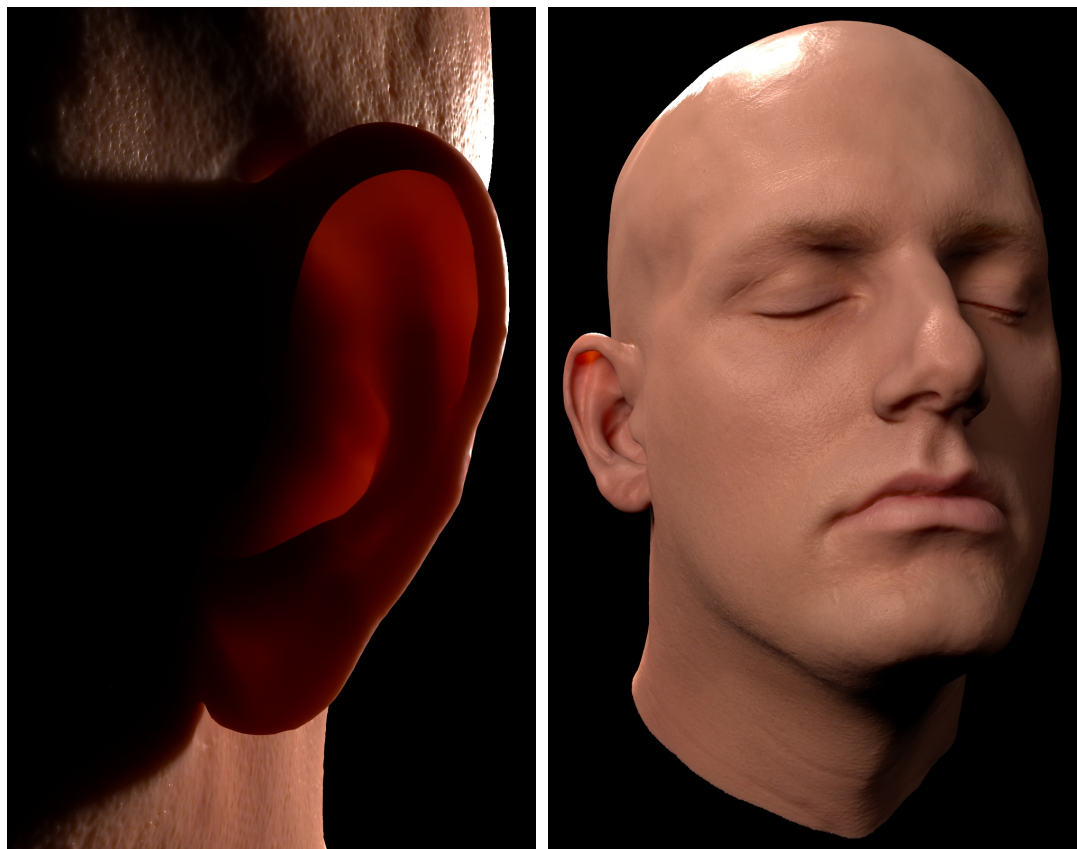


Figure 8.11: Applying skin parameters to an entire face with texturing. The left image shows how our model captures the scattering of light through thin areas such as the ear, while the right shows the skin illuminated from several directions. For both images, the parameters are $C_m = 0.2\%$, $\beta_m = 0.5$, $C_h = 1\%$, and $\rho_s = 0.25$.



Figure 8.12: Closeup of the head model using a spectral diffusion profile (left) and a RGB diffusion profiles (right). Note the color difference, and excessive translucency when using the RGB profiles. The RGB profile was generated directly from the spectral profile. For both images, the parameters are $C_m = 0.3\%$, $\beta_m = 0$, $C_h = 1\%$, and $\rho_s = 0.4$.

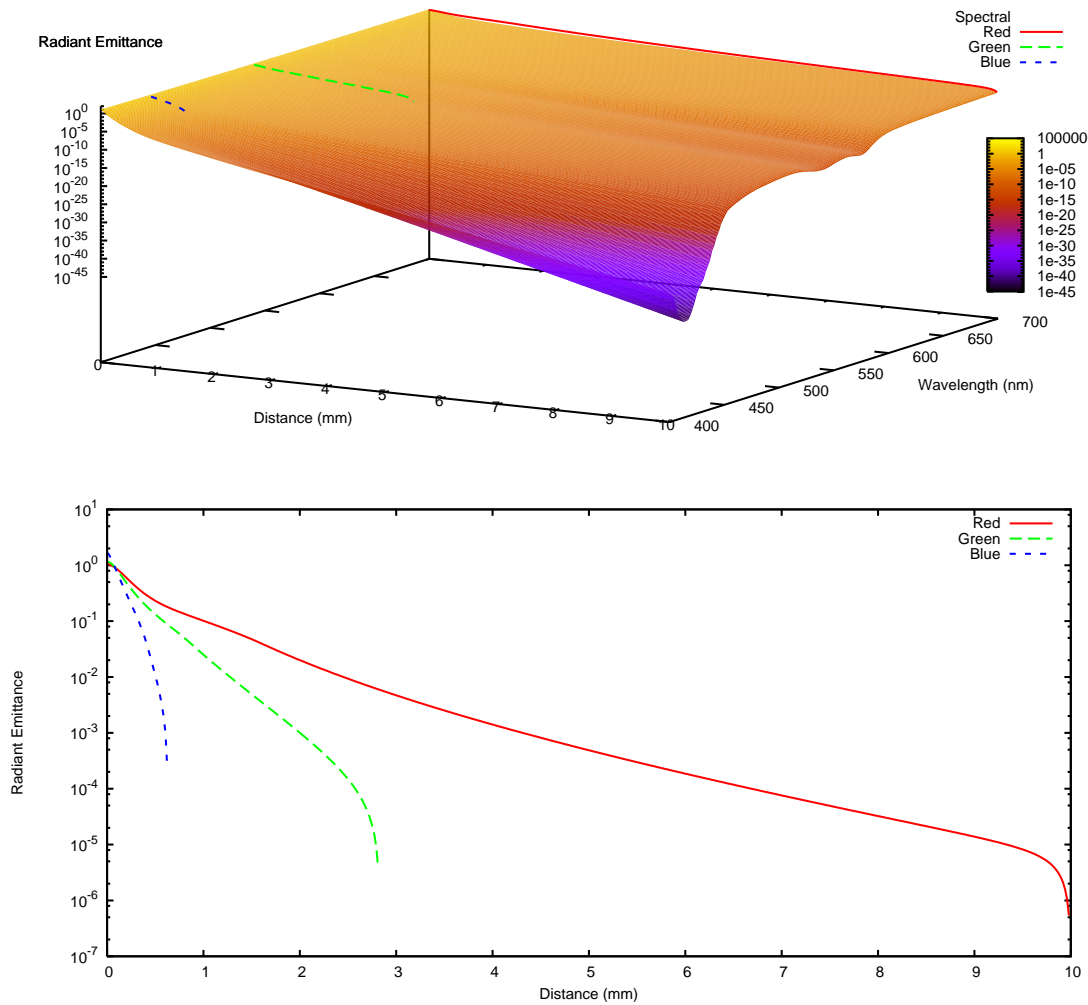


Figure 8.13: The full spectral profiles for the parameters given in Figure 8.12 (top), and a closeup of the RGB diffusion profiles (bottom). The RGB profiles do not span the full distance range (particularly the blue and green channels), as the spectrum represents colors outside of the RGB colorspace. The RGB profiles represent a small slice of the full spectral profile, and cannot reproduce its accuracy.

Chapter 9

Conclusions

This dissertation takes the field of computer graphics towards photorealistic image synthesis of scattering materials. It has introduced a new model spectral shading model for human skin, based on a new more general model of light transport in thin and multi-layered scattering materials, the multipole. We have shown that these new models are practical and efficient, as well as accurate, and are suitable for creating photorealistic images of translucent materials.

We have also given a full derivation of the diffusion dipole method, starting from the theory of radiative transport. This enabled us to analyze the limitations of the dipole model, producing directions where it could be extended and improved upon. Specifically, we found that the dipole is limited by its assumptions of semi-infinite geometry, high albedo, and homogeneity.

The diffusion multipole method has significant advantages over the dipole method, and is in fact generalizes to the dipole as the thickness of the material approaches infinity. The multipole is based on the same approximations as the dipole, namely the diffusion approximation. The multipole, however, extends to model layered materials through a novel frequency space technique that efficiently convolves together the infinite modes of multiple scattering between diffusing layers. This avoids the use of difficult boundary conditions between diffusing layers, and allows for a model that handles arbitrary configurations of diffusing layers, including those with mismatched indices of refraction at their boundaries. We have compared the results of the multipole method

with Monte Carlo simulation using parameters taken from previously published work as examples of its applicability, and have shown good agreement. We have also given several examples of photorealistic rendered images to show the plausibility and practicality of the shading model. In cases where diffusion is applicable, the multipole accurate describes the reflectance and transmittance of translucent slabs and layered materials.

This dissertation has also introduced a novel, practical shading model for human skin. The model builds on the multipole method, and simulates skin as a two-layer translucent material with an oily surface. Using only four parameters –total melanin content, melanin type, hemoglobin content, and surface oiliness– the model is simple, yet accurate. It provides large flexibility to simulate the color of skin with a minimum of confusion, and accurately models a wide range of skin appearance including African, Asian and Caucasian skin. Simplifying parameter selection, however, requires the use of spectral diffusion profiles, but these do not significantly affect render times.

These new models are also applicable in fields outside of computer graphics. As we have shown, the multi-layered model is simpler, just as accurate, and more general than previous work in optics and medical physics. The skin model in particular should be useful in dermatology and pigment cell research for simulating the reflectance spectrum of skin.

9.1 Future work

As we showed at the end of Chapter 5, the diffusion approximation breaks down in several cases, and it is generally difficult to predictably generate a desired appearance through the choice optical properties. We removed the semi-infinite restriction in Chapter 7, but there are still limitations on materials that the multipole method can simulate. Diffusion theory must be applicable in each layer, and each layer must be homogeneous. This adds a restriction on the minimum thickness of a layer; the positive source of the 0th order dipole pair must be contained within the slab. Thus, a layer should be at least two mean free paths thick. A more accurate model for near-source reflectance and transmittance could remove this restriction. The homogeneity assumption also prevents

the modeling of internal structures within (or spanning) layers (e.g. bones in a translucent fish, or a black rock embedded in a stratified translucent crystal). Another useful application of the multi-layer model that should be explored is to determine whether it can be used to make accurate measurements of optical properties of layered translucent materials.

We will also investigate extending the skin shading model to handle abnormal concentrations of other chromophores, such as beta-carotene and bilirubin. Such extensions will make the model more complicated, adding more terms to Equations 8.5 and 8.6, but would allow for modeling skin rashes or sunburns and other abnormal skin conditions. It would also be useful to add asperity scattering [70] due to tiny hairs (peach fuzz) on the skin, or from an additional layer of cosmetics. It also seems straightforward to use the model to automatically recover the model's parameters from real skin.

In this dissertation we have not explored one other limitation of diffusion: the assumption of high albedo. The hybrid methods presented in Chapter 6 couple the diffusion dipole with more accurate techniques such as photon packet tracing, but significantly reduce the efficiency of the method. One very interesting avenue for future research would be to derive an analytical solution for low albedo materials, either based on diffusion theory, or other approximations of radiative transport. Any such work would also have to accurately model single and low-order scattering.

Bibliography

- [1] S. Alaluf, D. Atkins, K. Barrett, M. Blount, N. Carter, and A. Heath. Ethnic variation in melanin content and composition in photoexposed and photoprotected skin. *Pigment Cell Res.*, 15:112–118, 2002.
- [2] S. Alaluf, A. Heath, N. Carter, D. Atkins, H. Mahalingam, K. Barrett, R. Kolb, and N. Smit. Variation in melanin content and composition in Type V and VI photoexposed and photoprotected human skin: the dominant role of dhi. *Pigment Cell Res.*, 14:337–347, 2001.
- [3] G. Alexandrakis, T. J. Farrell, and M. S. Patterson. Monte carlo diffusion hybrid model for photon migration in a two-layer turbid medium in the frequency domain. *Appl. Opt.*, 39(13):2235–2244, 2000.
- [4] R. R. Anderson and J. A. Parrish. The optics of human skin. *J. Invest. Dermatol.*, 77:13–19, 1981.
- [5] G. V. G. Baranoski and J. G. Rokne. Efficiently simulating scattering of light by leaves. *The Visual Computer*, 17:491–505, 2001.
- [6] A. N. Bashkaov, E. A. Genina, V. I. Kochubey, and V. V. Tuchin. Optical properties of human skin, subcutaneous and mucous tissues in the wavelength range from 400 to 2000 nm. *J. Phys. D*, 38:2543–2555, 2005.
- [7] P. Beckmann and A. Spizzichino. *The Scattering of Electromagnetic Waves from Rough Surfaces*. Pergamon Press Ltd., 1963.
- [8] A. Beer. *Grundriss des Photometrischen Calcüles*. Braunschweig, 1854.
- [9] S. D. Bianco, F. Martelli, and G. Zaccanti. Procedure for retrieving the optical properties of a two-layered medium from time-resolved reflectance measurements. *Opt. Lett.*, 36(19):4587–4599, 1997.
- [10] M. Birkinshaw. Radially symmetric fourier transforms. In *Astronomical Data Analysis Software and Systems III*, volume 61 of *ASP Conference Series*, pages 249–252, 1994.

- [11] J. F. Blinn. Models of light reflection for computer synthesized pictures. *Proceedings of 4th annual conference on Computer graphics and interactive techniques*, pages 192–198, 1977.
- [12] J. F. Blinn. Light reflection functions for simulation of clouds and dusty surfaces. In *Computer Graphics (Proceedings of ACM SIGGRAPH 1982)*, volume 16, pages 21–29. ACM, 1982.
- [13] G. Borshukov and J. P. Lewis. Realistic human face rendering for “The Matrix Reloaded”. In *ACM SIGGRAPH Sketches and Applications*, page 1. ACM, 2003.
- [14] J. Buhler, J. Gibbs, S. Peterson, and S. Singer. Visual effects in shrek, 2001.
- [15] S. Chandrasekhar. *Radiative Transfer*. Dover, 1960.
- [16] Y. Chen, X. Tong, J. Wang, S. Lin, B. Guo, and H.-Y. Shum. Shell texture functions. *ACM Trans. Graphic.*, 23:343–353, 2004.
- [17] D. Contini, F. Martelli, and G. Zaccanti. Photon migration through a turbid slab described by a model based on diffusion approximation. I. Theory. *Appl. Opt.*, 36(19):4587–4599, 1997.
- [18] R. L. Cook and K. Torrance. A reflectance model for computer graphics. In *ACM Trans. Graphic.*, pages 7–24, 1982.
- [19] C. J. Curtis, S. E. Anderson, J. E. Seims, K. W. Fleischer, and D. H. Salesin. Computer-generated watercolor. In *SIGGRAPH ’97: Proceedings of the 24th annual conference on Computer graphics and interactive techniques*, pages 421–430, New York, NY, USA, 1997. ACM Press/Addison-Wesley Publishing Co.
- [20] K. J. Dana, B. van Ginneken, S. K. Nayar, and J. J. Koenderink. Reflectance and texture of real-world surfaces. In *Proceedings of ACM SIGGRAPH 1999*, volume 18 of *Computer Graphics Proceedings*, pages 1–34, New York, 1999. ACM Press/Addison-Wesley Publishing Co.
- [21] I. Dayan, S. Havlin, and G. H. Weiss. Photon migration in a two-layer turbid medium: A diffusion analysis. *J. Mod. Opt.*, 39(7):1567–1582, 1992.
- [22] P. Debevec, T. Hawkins, C. Tchou, H.-P. Duiker, W. Sarokin, , and M. Sagar. Acquiring the reflectance field of a human face. In *Proceedings of ACM SIGGRAPH 2000*, Computer Graphics Proceedings, pages 145–156, New York, 2000. ACM Press/Addison-Wesley Publishing Co.
- [23] J. Dorsey, A. Edelman, H. W. Jensen, J. Legakis, and H. K. Pedersen. Modeling and rendering of weathered stone. In *Proceedings of ACM SIGGRAPH 1999*, Computer Graphics Proceedings, pages 225–234, New York, 1999. ACM Press/Addison-Wesley Publishing Co.

- [24] J. Dorsey and P. Hanrahan. Modeling and rendering of metallic patinas. In *SIGGRAPH '96: Proceedings of the 23rd annual conference on Computer graphics and interactive techniques*, pages 387–396, New York, NY, USA, 1996. ACM Press.
- [25] J. J. Duderstadt and L. J. Hamilton. *Nuclear reactor analysis*. Wiley, 1976.
- [26] D. R. Duncan. The colour of pigment mixtures. In *Proceedings of the Physical Society*, volume 52, pages 390–401, 1940.
- [27] S. Eda and E. Okada. Monte carlo analysis of near-infrared light propagation in a neonatal head model. *Systems and Computers in Japan*, 35(9):60–69, 2004. Translated from Denshi Joho Tsushin Gakkai Ronbunshi, Vol. J84-D-II, No. 12, December 2001, pp 2654–2661.
- [28] W. G. Egan, T. W. Hilgeman, and J. Reichman. Determination of absorption and scattering coefficients for nonhomogeneous media. 2: Experiment. *Appl. Opt.*, 12:1816–1823, 1973.
- [29] L. W. Esposito and K. Lumme. The tilt effect for Saturn’s rings. *Icarus*, 31:157–167, 1977.
- [30] G. W. Faris. Diffusion equation boundary conditions for the interface between turbid media: a comment. *J. Opt. Soc. Am. A*, 19(3):519–520, 2002.
- [31] T. J. Farrell, M. S. Patterson, and M. Essenpreis. Influence of layered tissue architecture on estimates of tissue optical properties obtained from spatially resolved diffuse reflectometry. *Appl. Opt.*, 37(10):1958–1972, 1998.
- [32] T. J. Farrell, M. S. Patterson, and B. Wilson. A diffusion theory model of spatially resolved, steady-state diffuse reflections for the noninvasive determination of tissue optical properties *in vivo*. *Med. Phys.*, 19(4):879–888, 1992.
- [33] L. Fukshansky, A. M. von Remisoksky, and J. McClendon. Absorption spectra of leaves corrected for scattering and distributional error: a radiative transfer and absorption statistics treatment. *Photochem. Photobiol.*, 57(3):538–555, 1993.
- [34] K. Furutsu. Diffusion equation derived from space-time transport equation. *J. Opt. Soc. Am.*, 70(4):360–366, 1980.
- [35] A. S. Glassner. *Principles of Digital Image Synthesis*. Morgan Kaufmann, 1995.
- [36] S. Glasstone and A. Sesonske. *Nuclear Reactor Engineering*. Van Nostrand Company, 1955.

- [37] M. Goesele, H. P. A. Lensch, J. Lang, C. Fuchs, and H. Peter Siedel. DISCO: aquisition of translucent objects. *ACM Trans. Graphic.*, 23(3):835–844, 2004.
- [38] L. Grabowski. On the theoretical photometry of diffuse reflection. *Astrophys. J.*, 39:299–306, 1914.
- [39] R. A. J. Groenhuis, H. A. Ferwerda, and J. J. T. Bosch. Scattering and absorption of turbid materials determined from reflection measurements, I: Theory. *Appl. Opt.*, 22(16):2456–2462, 1983.
- [40] K. T. H. Li, F. Pellacini. A hybrid monte carlo method for accurate and efficient subsurface scattering. In *Rendering Techniques*, pages 283–290, 2005.
- [41] C. S. Haase and G. W. Meyer. Modeling pigmented materials for realistic image synthesis. *ACM Trans. Graphic.*, 11(4):305–335, 1992.
- [42] P. Hanrahan and W. Krueger. Reflection from layered surfaces due to subsurface scattering. In *Proceedings of ACM SIGGRAPH 1993*, Computer Graphics Proceedings, pages 164–174, New York, 1993. ACM Press/Addison-Wesley Publishing Co.
- [43] B. W. Hapke. A theoretical photometric function for the lunar surface. *J. Geophys. Res.*, 68(15):4571–4586, 1963.
- [44] X. D. He, P. O. Heynen, R. L. Phillips, K. E. Torrance, D. H. Salesin, and D. P. Greenberg. A fast and accurate light reflection model. In *Computer Graphics (Proceedings of ACM SIGGRAPH 1992)*, volume 22, pages 253–254, 1992.
- [45] X. D. He, K. E. Torrance, F. X. Stillion, and D. P. Greenberg. A comprehensive physical model for light reflection. In *Computer Graphics (Proceedings of ACM SIGGRAPH 1991)*, volume 25, pages 175–186, 1991.
- [46] R. P. Hemenger. Optical properties of turbid media with specularly reflecting boundaries: applications to biological problems. *Appl. Opt.*, 16(7):2007–2012, 1977.
- [47] A. Hennessy, C. Oh, B. Diffey, K. Wakamatsu, S. Ito, and J. Rees. Eumelanin and pheomelanin concentrations in human epidermis before and after UVB radiation. *Pigment Cell Res.*, 18:220–223, 2005.
- [48] L. G. Henyey and H. L. Greenstein. Diffuse radiation in the galaxy. *Astrophys. J.*, 43:70–83, 1941.
- [49] C. Hery. Implementing a skin bssrdf. *ACM SIGGRAPH 2003 Course 9*, pages 73–88, 2003.

- [50] T. Igarashi, K. Nishino, and S. K. Nayar. The appearance of human skin. Technical Report CUCS-024-05, Columbia University, 2005.
- [51] A. Ishimaru. *Wave Propagation and Scattering in Random Media*. Oxford University Press, 1978.
- [52] S. Ito and K. Wakamatsu. Quantitative analysis of eumelanin and pheomelanin in humans, mice, and other animals: a comparative review. *Pigment Cell Res.*, 16:523–531, 2006.
- [53] S. L. Jacques. Origins of tissue optical properties in the uva, visible, and nir regions. In *OSA TOPS on Advances in Optical Imaging and Photon Migration*, volume 2, pages 364–371, 1996.
- [54] S. L. Jacques. Skin optics. *Oregon Medical Laser Center News*, page <http://omlc.ogi.edu/news/jan98/skinoptics.html>, 1998.
- [55] S. L. Jacques and D. J. McAuliffe. The melanosome: threshold temperature for explosive vaporization and internal absorption coefficient during pulsed laser irradiation. *Photochem. Photobiol.*, 53:769–775, 1991.
- [56] S. L. Jacques and S. A. Prahl. Modeling optical and thermal distributions in tissue during laser irradiation. *Lasers Surg. Med.*, 6:494–503, 1987.
- [57] H. W. Jensen. Global illumination using photon maps. In *Rendering Techniques*, pages 21–30, 1996.
- [58] H. W. Jensen. *Realistic Image Synthesis Using Photon Mapping*. AK Peters, 2001.
- [59] H. W. Jensen and J. Buhler. A rapid hierarchical rendering technique for translucent materials. *ACM Trans. Graphic.*, 21:576–581, 2002.
- [60] H. W. Jensen and P. H. Christensen. Efficient simulation of light transport in scenes with participating media using photon maps. In *Proceedings of ACM SIGGRAPH*, pages 311–320, 1998.
- [61] H. W. Jensen, J. Legakis, and J. Dorsey. Rendering of wet materials. In *Rendering Techniques*, pages 273–282, 1999.
- [62] H. W. Jensen, S. R. Marschner, M. Levoy, and P. Hanrahan. A practical model for subsurface light transport. In *Proceedings of ACM SIGGRAPH 2001*, Computer Graphics Proceedings, pages 511–518, New York, 2001. ACM Press/Addison-Wesley Publishing Co.
- [63] J. Joseph, W. Wiscombe, and J. Weinman. The delta-eddington approximation for radiative flux transfer. *Journal of the Atmospheric Sciences*, 33(12):2452—2459, 1976.

- [64] N. Joshi, C. Donner, and H. W. Jensen. Noninvasive measurement of scattering anisotropy in turbid materials by nonnormal incident illumination. *Opt. Lett.*, 31:936–938, 2006.
- [65] D. B. Judd and G. Wyszecki. *Color in business, science, and industry*. John Wiley & Sons, 1975.
- [66] J. T. Kajiya. The rendering equation. In *Proceedings of ACM SIGGRAPH*, pages 143–150, 1986.
- [67] M. Keijzer, W. M. Star, and P. R. M. Storchi. Optical diffusion in layered media. *Appl. Opt.*, 27(9):1820–1824, 1988.
- [68] A. Kienle, T. Glanzmann, G. Wagnières, and H. van den Bergh. Investigation of two-layered turbid media with time-resolved reflectance. *Appl. Opt.*, 37(28):6852–6862, 1998.
- [69] A. Kienle, M. S. Patterson, N. Dögnitz, R. Bays, G. Wagnières, and H. van den Bergh. Noninvasive determination of the optical properties of two-layered turbid media. *Appl. Opt.*, 37(4):779–791, 1998.
- [70] J. Koenderink and S. Pont. The secret of velvety skin. *Mach. Vision Appl.*, 14(4):260–268, 2003.
- [71] G. Kortüm. *Reflectance Spectroscopy*. Springer-Verlag, 1969.
- [72] A. Krishnaswamy and G. V. G. Baranowski. A biophysically-based spectral model of light interaction with human skin. In *Proceedings of EUROGRAPHICS 2004*, volume 23, 2004.
- [73] P. Kubelka. New contributions to the optics of intensely light-scattering materials. part i. *J. Opt. Soc. Am.*, 38(5):448–457, 1948.
- [74] P. Kubelka. New contributions to the optics of intensely light-scattering materials. Part II: Non homogeneous layers. *J. Opt. Soc. Am.*, 44(4):330–335, 1954.
- [75] P. Kubelka and F. Munk. Ein Beitrag zur Optik der Farbanstriche. *Zeitschrift für technische Physik*, 12:593–601, 1931. English translation by Steve Westin.
- [76] E. P. Lafourne and Y. D. Willem. Bi-directional path tracing. In *Proceedings of Third International Conference on Computational Graphics and Visualization Techniques (Compugraphics '93)*, pages 145–153, 1993.
- [77] E. P. Lafourne and Y. D. Willem. Rendering participating media with bidirectional path tracing. In *Rendering Techniques*, pages 91–100, 1996.

- [78] J. H. Lambert. *Photometria sive de mensura et grodibus liminis colorum et umbrae*. Augustae Vindelicorum, 1760. English translation by David L. DiLaura.
- [79] F. Martelli, A. Sassaroli, S. D. Bianco, Y. Yamada, and G. Zaccanti. Solution of the time-dependent diffusion equation for layered diffusive media by the eigenfunction method. *Phys. Rev. E*, 28(4):1236–1238, 2003.
- [80] F. Martelli, A. Sassaroli, Y. Yamada, and G. Zaccanti. Analytical approximate solutions of the time-domain diffusion equation in layered slabs. *J. Opt. Soc. Am. A*, 19(1):71–80, 2002.
- [81] I. V. Meglinski and S. J. Matcher. Quantitative assessment of skin layers absorption and skin reflectance spectra simulation in the visible and near-infrared spectral regions. *Physiol. Meas.*, 23:741–753, 2002.
- [82] G. Mie and L. V. Lorenz. Beiträge zur optik trüber medien, speziell kolloidaler metallösungen. *Ann. Phys. Leipzig*, 25:377–445, 1908.
- [83] J. D. Moulton. Diffusion modeling of picosecond laser pulse propagation in turbid media. Master’s thesis, McMaster University, 1990.
- [84] C. S.-L. Ng and L. Li. A multi-layered reflection of natural human skin. In *Computer Graphics International 2001 (CGI’01)*, pages 249–266, 2001.
- [85] F. E. Nicodemus, J. C. Richmond, J. J. Hsia, I. W. Ginsberg, and T. Limperis. *Geometrical Considerations and Nomenclature for Reflectance*. National Bureau of Standards, 1977.
- [86] M. S. Patterson, B. Chance, and B. C. Wilson. Time resolved reflectance and transmittance for the noninvasive measurement of tissue optical properties. *Appl. Opt.*, 28(12):2331–2336, 1989.
- [87] M. S. Patterson, E. Schwartz, and B. C. Wilson. Quantitative reflectance spectrophotometry for the noninvasive measurement of photosensitizer concentration in tissue during photodynamic therapy. In *Proc. SPIE*, volume 1065, pages 115–122, 1989.
- [88] P. Peers, K. vom Berge, W. Matusik, R. Ramamoorthi, J. Lawrence, S. Rusinkiewicz, and P. Dutré. A compact factored representation of heterogeneous subsurface scattering. *ACM Trans. Graphic.*, 25(3):746–753, 2006.
- [89] M. Pharr and P. Hanrahan. Monte carlo evaluation of non-linear scattering equations for subsurface reflection. In *Proceedings of ACM SIGGRAPH 2000*, Computer Graphics Proceedings, pages 75–84, New York, 2000. ACM Press/Addison-Wesley Publishing Co.

- [90] B. T. Phong. Illumination for computer generated pictures. In *Communications of the ACM*, volume 8, pages 311–317, 1975.
- [91] S. Prahl. *Light Transport in Tissue*. PhD thesis, University of Texas at Austin, 1998.
- [92] S. Prahl, M. Keijzer, S. L. Jacques, and A. J. Welch. A monte carlo model of light propagation in tissue. In *Proc. SPIE*, volume IS 5, pages 102–111, 1989.
- [93] J. W. S. L. Rayleigh. On the scattering of light by small particles. *Philosophical Magazine*, 61:447–454, 1871.
- [94] J. Ripoll and M. Nieto-Vesperinas. Index mismatch for diffuse photon density waves at both flat and rough diffuse-diffuse interfaces. *J. Opt. Soc. Am.*, 16(8):1947–1957, 1999.
- [95] J. Ripoll, V. Ntziachristos, J. P. Culver, D. N. Pattanayak, A. G. Yodh, and M. Nieto-Vesperinas. Recovery of optical parameters in multiple-layered diffusive media: theory and experiments. *J. Opt. Soc. Am.*, 18(4):821–830, 2001.
- [96] I. S. Saidi, S. L. Jacques, and F. K. Tittel. Mie and Rayleigh modeling of visible-light scattering in neonatal skin. *Appl. Opt.*, 34(31):7410–7418, 1995.
- [97] J. Sandby-M oller, T. Poulsen, and H. C. Wulf. Influence of epidermal thickness, pigmentation and redness on skin autofluorescence. *Photochem. Photobiol.*, 77(6):616–620, 2003.
- [98] T. Sarna and H. M. Swartz. The physical properties of melanins. In J. J. Nordlund, R. E. Boissy, V. J. Hearing, R. A. King, and J. Paul Ortonne, editors, *The Pigmentary System: Physiology and Pathophysiology*, chapter 25, pages 333–357. Oxford University Press, 1998.
- [99] C. Schlick. An inexpensive brdf model for physically-based rendering. *Computer Graphics Forum*, 13(3):223–246, 1994.
- [100] J. M. Schmitt, G. X. Zhou, and E. C. Walker. Multilayer model of photon diffusion in skin. *J. Opt. Soc. Am. A*, 7(1):2141–2153, 1990.
- [101] A. Schuster. Radiation through a foggy atmosphere. *Astrophys. J.*, 21:1–22, 1905.
- [102] P. Shirley and H. Hu. A practitioners’ assessment of light reflection models. In *Proceedings of Pacific Graphics*, 1997.
- [103] T. Spott, L. O. Svaasand, R. E. Anderson, and P. F. Schmedling. Application of optical diffusion theory to transcutaneous bilirubinometry. In *Proc. SPIE*, volume 3195, pages 234–245, 1997.

- [104] J. Stam. Multiple scattering as a diffusion process. In *Rendering Techniques*, pages 41–50, 1995.
- [105] J. Stam. An illumination model for a skin layer bounded by rough surfaces. In *Rendering Techniques*, pages 39–52, 2001.
- [106] G. N. Stamatias, B. z. Zmudzka, N. Kollias, and J. Z. Beer. Non-invasive measurements of skin pigmentation *in situ*. *Pigment Cell Res.*, 17:618–626, 2004.
- [107] S. Takatania and M. D. Graham. Theoretical analysis of diffuse reflectance from a two-layer tissue model. *IEEE Trans. Biomed. Eng.*, 26(12):656–664, 1979.
- [108] X. Tong, J. Wang, S. Lin, B. Guo, and H. Yeung Shum. Modeling and rendering of quasi-homogeneous materials. *ACM Trans. Graphic.*, 24(3):1054–1061, 2005.
- [109] K. Torrance and E. Sparrow. Theory for off-specular reflection from roughened surfaces. *J. Opt. Soc. Am.*, 57:1104–1114, 1967.
- [110] N. Tsumura and Y. Miyake. Independent component analysis of skin color image. *J. Opt. Soc. Am.*, 16(9):2169–2176, 1999.
- [111] N. Tsumura, N. Ojima, K. Sato, M. Shiraishi, H. Shimizu, H. Nabeshima, S. Akazaki, K. Hori, and Y. Miyake. Image-based skin color and texture analysis-synthesis by extracting hemoglobin and melanin information in the skin. *ACM Trans. Graphic.*, 22(3):770–779, 2003.
- [112] J.-M. Tualle, H. L. Nghiem, D. Ettori, R. Sablong, E. Tinet, and S. Avrillier. Asymptotic behavior and inverse problem in layered scattering media. *J. Opt. Soc. Am. A*, 21(1):24–34, 2004.
- [113] J.-M. Tualle, J. Prat, E. Tinet, and S. Avrillier. Real-space green’s function calculation for the solution of the diffusion equation in stratified turbid media. *J. Opt. Soc. Am. A*, 17(11):2046–2055, 2000.
- [114] V. Tuchin. *Tissue Optics: Light Scattering Methods and Instruments for Medical Diagnosis*. SPIE Press, 2000.
- [115] M. J. C. van Gemert, S. L. Jacques, H. J. C. M. Sterenborg, and W. M. Star. Skin optics. *IEEE Trans. Biomed. Eng.*, 36(12):1146–1154, 1989.
- [116] M. J. C. van Gemert, S. L. Jacques, H. J. C. M. Sterenborg, and W. M. Star. Skin Optics. *IEEE Trans. Biomed. Eng.*, 36:1146–1154, 1989.
- [117] E. Veach. *Robust Monte Carlo Methods for Light Transport Simulation*. PhD thesis, Stanford University, 1997.

- [118] I. A. Vitkin, B. C. Wilson, and R. R. Anderson. Analysis of layered scattering materials by pulsed photothermal radiometry: application to photon propagation in tissue. *Appl. Opt.*, 34(16):2973–2982, 1993.
- [119] H. von Seeliger. Zur photometrie zerstreut reflectirender substanz. In *Mathematisch-Physikalische Klasse: Sitzungsberichte*. Bayerische Akademie der Wissenschaften, 1888.
- [120] M. J. Vrhel, R. Gershon, and L. S. Iwan. Measurement and analysis of object reflectance spectra. *Color Res Appl.*, 19(1):2–9, 1994.
- [121] K. Wakamatsu, R. Kavanagh, A. L. Kadekaro, S. Terzieva, R. A. Sturm, S. Leachman, Z. Abdel-Malek, and S. Ito. Diversity of pigmentation in cultured human melanocytes is due to differences in the type as well as quantity of melanin. *Pigment Cell Res.*, 19:154–162, 2006.
- [122] L. V. Wang. Rapid modeling of diffuse reflectance of light in turbid slabs. *J. Opt. Soc. Am. A*, 15(4):936–944, 1998.
- [123] L. V. Wang and S. L. Jacques. Hybrid model of monte carlo simulation and diffusion theory for light reflectance by turbid media. *J. Opt. Soc. Am. A*, 10(8):1746–1752, 1993.
- [124] L. V. Wang, S. L. Jacques, and L. Zheng. Mcml – monte carlo modeling of light transport in multi-layered tissues. *Computer Methods in Programs and Biomedicine*, 47(8):131–146, 1995.
- [125] L. V. Wang, S. L. Jacques, and L. Zheng. Conv – convolution for responses to a finite diameter photon beam incident on multi-layered tissues. *Computer Methods in Programs and Biomedicine*, 54:141–150, 1997.
- [126] G. J. Ward. Measuring and modeling anisotropic reflection. In *Proceedings of ACM SIGGRAPH*, pages 265–272, 1992.
- [127] A. M. Weinberg and E. P. Wigner. *The physical theory of neutron Chain Reactors*. University of Chicago Press, 1958.
- [128] W. W. Wendlandt and H. G. Hecht. *Reflectance Spectroscopy*. Interscience Publishers, 1966.
- [129] T. Weyrich, W. Matusik, H. Pfister, B. Bickel, C. Donner, C. Tu, J. McAndless, J. Lee, A. Ngan, H. W. Jensen, and M. Gross. Analysis of human faces using a measurement-based skin reflectance model. *ACM Trans. Graphic.*, 25:1013–1024, 2006.

- [130] B. C. Wilson and M. S. Patterson. The physics of photodynamic therapy. *Phys. Med. Bio.*, 31:327–360, 1986.
- [131] D. R. Wyman, M. S. Patterson, and B. C. Wilson. Similarity relations for anisotropic scattering in monte carlo simulations of deeply penetrating neutral particles. *J. Comput. Phys.*, 81:137–150, 1989.
- [132] J. K. F. Zöllner. *Photometrische Untersuchungen mit besonderer Rücksicht auf die physische Beschaffenheit der Himmelskörper*. Engelmann, 1865.
- [133] G. Zonios, J. Bykowski, and N. Kollias. Skin melanin, hemoglobin, and light scattering properties can be quantitatively assessed *In Vivo* using diffuse reflectance spectroscopy. *J. Comput. Phys.*, 81:137–150, 2001.